3-2021

Applied Reachability Analysis for Time-Optimal Spacecraft Attitude Reorientations

Layne C. Barrett

Applied Reachability Analysis for Time-Optimal Spacecraft Attitude Reorientations

THESIS

Layne C. Barrett, Capt, USAF

AFIT-ENY-MS-21-M-287

DEPARTMENT OF THE AIR FORCE
AIR UNIVERSITY

AIR FORCE INSTITUTE OF TECHNOLOGY

Wright-Patterson Air Force Base, Ohio

AFIT-ENY-MS-21-M-287

APPLIED REACHABILITY ANALYSIS FOR TIME-OPTIMAL SPACECRAFT ATTITUDE REORIENTATIONS

THESIS

Presented to the Faculty

Department of Aeronautics & Astronautics

Graduate School of Engineering and Management

Air Force Institute of Technology

Air University

Air Education and Training Command

in Partial Fulfillment of the Requirements for the

Degree of Master of Astronautical Engineering

Layne C. Barrett, BS

Capt, USAF

March 25, 2021

AFIT-ENY-MS-21-M-287

APPLIED REACHABILITY ANALYSIS FOR TIME-OPTIMAL SPACECRAFT ATTITUDE REORIENTATIONS

THESIS

Layne C. Barrett, BS
Capt, USAF

Committee Membership:

Maj Costantinos Zagaris, PhD
Chair

Maj Joshuah A. Hess, PhD
Member

Richard G. Cobb, PhD
Member

Adedeji B. Badiru, PhD
Dean, Graduate School of Engineering and Management

AFIT-ENY-MS-21-M-287

Abstract

Satellite attitude reorientation has been of significant interest in the field of astronautical engineering, and being able to reorient in a time-optimal manner has been of exceeding interest since the 1970s. Satellite reorientations are used for a variety of mission sets, including on-orbit servicing and sensor pointing. Ensuring a mission set can be conducted within a certain amount of time raises the question of whether or not a certain maneuver can be completed with a bounded control. This thesis answers that question by using the concept of reachability to provide reachable sets for different spacecraft scenarios. The reachable sets generated provide a range of initial states that guarantee a satellite will reach a desired end orientation given a certain time constraint. Being able to validate that a certain end state can be reached before a maneuver is attempted can save both time and energy expended by a spacecraft. Prior research providing a formal approach of applying reachability to spacecraft attitude maneuvers has not been found. The analysis of the reachable sets yields the insight that using Modified Rodriguez Parameters (MRPs) to generate reachable sets is more time efficient than other attitude parameterizations. It was also found that the linearized MRP dynamics provide a valid time optimal solution for the nonlinear dynamics of medium angle attitude maneuvers. This linearized version of the dynamics was used to formulate an optimal control policy for spacecraft reorientations with bounded controls.

Acknowledgements

Foremost, I would like to thank Major Zagaris for all of his support and guidance. Thank you for your countless hours of teaching, guiding, and brainstorming of spacecraft dynamics and reachability that made this research possible. I would like to thank the rest of my committee for their instruction which contributed to the foundation of this thesis and for taking the time to provide feedback on the direction and results of my research.

I would also like to thank the rest of my professors for diving deep into the complexities and fascinations of astronautics and the space environment that were unfamiliar to me before arriving at AFIT. I also very much appreciate my fellow students who not only helped me significantly in our studies of learning the material, but providing the encouragement and humor that made my graduate experience enjoyable.

Most importantly, I thank my family and God. God for blessing me with the path to AFIT, and providing opportunity to attend AFIT at the same time as my wife. My parents for humbly providing the example of a strong work ethic and discipline, and encouraging me to pursue my goals. My sweet new daughter for being my alarm clock throughout the night to remind me to start another simulation, for the joy she brings to our family, and her smiles and laughs that make the long days worth it. Finally, my beloved wife for her encouragement and laughter she brought all year, all while going through classes and thesis research of her own. And all of this on top of patiently figuring out parenting with me and developing into an amazingly dedicated and loving mother.

Layne C. Barrett

Table of Contents

Page

Abstract iv

Acknowledgements v

List of Figures viii

List of Tables xiii

I. Introduction 1

1.1 Motivation and Background 1
1.2 Problem Statement 3
1.3 Research Questions 4
1.4 Organization of the Thesis 5

II. Background 6

2.1 Introduction 6
2.2 Fundamentals of Spacecraft Attitude Kinematics and Dynamics 6
2.2.1 Attitude Parameters and Kinematics 6
2.2.2 Rigid Body Dynamics 11
2.3 Optimal Reorientation 12
2.4 Reachability Theory and Application 16
2.4.1 Reachability Theory 16
2.4.2 Reachability Application to Spacecraft Maneuvering 19
2.4.3 Summary 19

III. Methodology 20

3.1 Rotational Dynamics 20
3.1.1 Spacecraft Model 20
3.1.2 Dynamics Formulation 21
3.2 Optimal Control and Reachable Sets 24
3.2.1 Optimal Control Formulation 24
3.2.2 Optimal Control Policy Development 25
3.2.3 Optimal Control Solution 27
3.2.4 Reachable Set Generation 28
3.3 Summary 29

Page

IV. Results and Analysis 30

4.1 Reachable Sets 30
4.1.1 Reachable Set Generation 30
4.1.2 Reachable Set Accuracy 32
4.1.3 MRP vs. Quaternion Reachable Sets 33
4.1.4 Differing Control Constraints 40
4.2 Computation Times 53
4.3 Optimal Control Policy 56
4.3.1 Control Policy Derivation 56
4.4 Control Policy Testing 61
4.4.1 Summary 64

V. Conclusions and Recommendations 65

5.1 Conclusions 65
5.2 Recommendations 67
Bibliography 75

List of Figures

Figure		Page
1	Illustration of Forward and Backward Reachable Sets	3
2	Illustration of Euler's Principal Rotation Theorem	8
3	Models: Symmetric (left), Axially Symmetric (center), Asymmetric (right)	21
4	Example Attitude Reorientation of Spacecraft: Asymmetric Body	25
5	Depiction of Starting Conditions	26
6	Reachable Set Organization Diagram	29
7	Reachable Sets Depicted as Time Optimal Contours from MRP dynamics, Nonlinear (left) and Linear (right) of Spherically Symmetric Body with Spherical Control Constraint	30
8	Starting Attitudes Mapped to Azimuth and Elevation	31
9	Propagated Solutions Compared to GPOPS-II Solutions: Nonlinear MRP Dynamics with a Spherically Symmetric Body and Spherical Control Constraint	32
10	MRP (left) vs Quaternion (right) Sets with Nonlinear Dynamics for a Spherically Symmetric Body and Spherical Control Constraint	34
11	MRP (left) vs Quaternion (right) Sets Depicted as Time Optimal Contours with Nonlinear Dynamics for a Spherically Symmetric Body and Cubic Control Constraint	34
12	MRP (left) vs Quaternion (right) Sets Depicted as Time Optimal Contours with Nonlinear Dynamics for an Axisymmetric Body and Spherical Control Constraint	35
13	MRP (left) vs Quaternion (right) Sets Depicted as Time Optimal Contours with Nonlinear Dynamics for an Axisymmetric Body and Cubic Control Constraint	35

Figure Page

14 MRP (left) vs Quaternion (right) Sets Depicted as Time Optimal Contours with Nonlinear Dynamics for an Asymmetric Body and Spherical Control Constraint 36

15 MRP (left) vs Quaternion (right) Sets Depicted as Time Optimal Contours with Nonlinear Dynamics for an Asymmetric Body and Cubic Control Constraint 36

16 Nonlinear (left) vs Linearized MRP (center) and Linearized Quaternion (right) Dynamics Sets Depicted as Time Optimal Contours for a Spherically Symmetric Body and Spherical Control Constraint 37

17 Nonlinear (left) vs Linearized MRP (center) and Linearized Quaternion (right) Dynamics Sets Depicted as Time Optimal Contours for a Spherically Symmetric Body and Cubic Control Constraint 38

18 Nonlinear (left) vs Linearized MRP (center) and Linearized Quaternion (right) Dynamics Sets Depicted as Time Optimal Contours for an Axisymmetric Body and Spherical Control Constraint 38

19 Nonlinear (left) vs Linearized MRP (center) and Linearized Quaternion (right) Dynamics Sets Depicted as Time Optimal Contours for a Axisymmetric Body and Cubic Control Constraint 39

20 Nonlinear (left) vs Linearized MRP (center) and Linearized Quaternion (right) Dynamics Sets Depicted as Time Optimal Contours for an Asymmetric Body and Spherical Control Constraint 39

21 Nonlinear (left) vs Linearized MRP (center) and Linearized Quaternion (right) Dynamics Sets Depicted as Time Optimal Contours for an Asymmetric Body with Cubic Control Constraint 40

22 Boresight Trajectories and Time Optimal Contours: Nonlinear MRP Dynamics, Asymmetric Body with Spherical Control Constraint 41

Figure Page

23 Boresight Trajectories and Time Optimal Contours Starting at 90 Degrees from Final Attitude of Nonlinear (left) and Linearized (right) Dynamics: Asymmetric Body with Spherical Control Constraint 42

24 Boresight Trajectories and Time Optimal Contours Starting at 90 Degrees from Final Attitude of Nonlinear (left) and Linearized (right) Dynamics: Asymmetric Body with Cubic Control Constraint 42

25 Boresight Trajectories and Time Optimal Contours Starting at 60 Degrees from Final Attitude of Nonlinear (left) and Linearized (right) Dynamics: Asymmetric Body with Cubic Control Constraint 43

26 Boresight Trajectories and Time Optimal Contours Starting at 30 Degrees from Final Attitude of Nonlinear (left) and Linearized (right) Dynamics: Asymmetric Body with Cubic Control Constraint 44

27 Boresight Trajectories and Time Optimal Contours Starting at 9 Degrees from Final Attitude of Nonlinear (left) and Linearized (right) Dynamics: Asymmetric Body with Cubic Control Constraint 44

28 Boresight Trajectories and Time Optimal Contours Starting at 30 Degrees from Final Attitude of Nonlinear (left) and Linearized (right) Dynamics: Asymmetric Body with Spherical Control Constraint 45

29 Trajectory 1 Control History of Nonlinear (left) and Linearized (right) Dynamics: 30 Degrees, Asymmetric Body with Spherical Control Constraint 46

30 Trajectory 2 Control History of Nonlinear (left) and Linearized (right) Dynamics: 30 Degrees, Asymmetric Body with Spherical Control Constraint 47

31 Trajectory 3 Control History of Nonlinear (left) and Linearized (right) Dynamics: 30 Degrees, Asymmetric Body with Spherical Control Constraint 47

32 Trajectory 4 Control History of Nonlinear (left) and Linearized (right) Dynamics: 30 Degrees, Asymmetric Body with Spherical Control Constraint 48

Figure Page

33 Trajectory 5 Control History of Nonlinear (left) and Linearized (right) Dynamics: 30 Degrees, Asymmetric Body with Spherical Control Constraint 48

34 Propagated Boresight Trajectories Compared to GPOPS-II Solutions: 30 degree Reorientation, Asymmetric Body with Spherical Constraint 49

35 Propagated Angular Velocity (rad/s) Compared to GPOPS-II Solutions: Trajectory 4, 30 degree Reorientation, Asymmetric Body with Spherical Constraint 50

36 Boresight Trajectories and Time Optimal Contours Starting at 60 Degrees from Final Attitude of Nonlinear (left) and Linearized (right) Dynamics: Asymmetric Body with Spherical Control Constraint 51

37 Propagated Boresight Trajectories Compared to GPOPS-II Solutions: 60 degree Reorientation, Asymmetric Body with Spherical Constraint 52

38 Propagated Angular Velocity (rad/s) Compared to GPOPS-II Solutions: Trajectory 4, 60 degree Reorientation, Asymmetric Body with Spherical Constraint 52

39 Definition of Control Direction 59

40 Propagated Angular Velocity (rad/s) Compared to GPOPS-II Solutions: Trajectory 4, 30 degree Reorientation, Asymmetric Body with Spherical Constraint 62

41 Propagated Angular Velocity (rad/s) Compared to GPOPS-II Solutions: Trajectory 4, 30 degree Reorientation, Asymmetric Body with Spherical Constraint 62

42 Propagated Angular Velocity (rad/s) Compared to GPOPS-II Solutions: Trajectory 4, 90 degree Reorientation, Asymmetric Body with Spherical Constraint 63

Figure Page

43 Reachable Set: Spherically Symmetric Body, Cubic Control Constraint 69

44 Reachable Set Depicted as Time Optimal Contours: Spherically Symmetric Body, Spherical Control Constraint 69

45 Reachable Set Depicted as Time Optimal Contours: Axisymmetric Body, Cubic Control Constraint 70

46 Reachable Set Depicted as Time Optimal Contours: Axisymmetric Body, Spherical Control Constraint 70

47 Reachable Set Depicted as Time Optimal Contours: Asymmetric Body, Cubic Control Constraint 71

48 Reachable Set Depicted as Time Optimal Contours: Asymmetric Body, Spherical Control Constraint 71

49 Reachable Set Depicted as Time Optimal Contours: Spherically Symmetric Body, Cubic Control Constraint 72

50 Reachable Set Depicted as Time Optimal Contours: Spherically Symmetric Body, Spherical Control Constraint 72

51 Reachable Set Depicted as Time Optimal Contours: Axisymmetric Body, Cubic Control Constraint 73

52 Reachable Set Depicted as Time Optimal Contours: Axisymmetric Body, Spherical Control Constraint 73

53 Reachable Set Depicted as Time Optimal Contours: Asymmetric Body, Cubic Control Constraint 74

54 Reachable Set Depicted as Time Optimal Contours: Asymmetric Body, Spherical Control Constraint 74

List of Tables

Table		Page
1	Computed Optimal 30 Degree Reorientation Times for Nonlinear vs. Linearized Dynamics	50
2	Computed Optimal 60 Degree Reorientation Times for Nonlinear vs. Linearized Dynamics	53
3	Computation Times of Optimization Batches for Generating Reachable Sets Using Nonlinear Dynamics	55
4	Computation Times of Optimization Batches for Generating Reachable Sets Using Linearized Dynamics	55
5	Summary Statistics of Computation Times	56
6	Maximum Pointing Errors	63

APPLIED REACHABILITY ANALYSIS FOR TIME-OPTIMAL SPACECRAFT ATTITUDE REORIENTATIONS

I. Introduction

Satellite attitude reorientation in a time-optimal manner is a problem of significant interest in the field of astronautical engineering. There are several applications for satellite reorientation, including sensor pointing, satellite servicing, and spacecraft or unknown object inspection. Being able to complete reorientations in a timely manner is essential to being able to conduct mission requirements. Being able to complete the mission must first start with the question: Is it even possible to complete a reorientation given certain physical constraints in an allowable time period? The concept of reachability answers this question, providing a range of initial states that guarantee a satellite reach a desired end orientation given a certain control and time constraint. Being able to validate that a certain end state can be reached before a maneuver is attempted can save both time and energy expended by a spacecraft. By not attempting an infeasible maneuver, the spacecraft can save its fuel and dedicate that time towards completing feasible tasks.

1.1 Motivation and Background

Time optimal control of dynamic systems has different applications across many research areas. The specific problem of spacecraft reorientation maneuvers, or attitude pointing, has been extensively studied by many researchers, with the objective of minimizing the maneuver time, amount of control required, or the vibration encountered when applying the control [1, 2, 3, 4, 5]. Many military and civilian space

missions require efficient and accurate attitude reorientation capabilities. Since satellites often have significant demand for collecting data, slewing based on that data, and disseminating data, the timeline to slew can heavily constrain the mission. This is especially true for satellites that are in lower Earth orbits, traveling at faster speeds, that do not have the luxury of being able to monitor the same section of Earth like satellites in geostationary orbits [3]. This highlights the necessity for spacecraft to achieve attitude changes in a time-optimal manner.

Another recent area of interest requiring time sensitive attitude changes is the field of satellite servicing. On February 25, 2020, Northrup Grumman successfully completed the first commercial spacecraft servicing mission with Mission Extension Vehicle 1 [6]. MEV-1 is intended to provide support to a telecommunication's satellite for five years, and then can be used to move on to other customer's satellites. This event ushers in an era where spacecraft servicing will become more prevalent, being able to refuel and repair existing satellites. Robotic servicers can also be used to conduct inspections of other spacecraft or unknown objects. Robotic inspection is a capability that enables a large number of proximity operations, including spacecraft supply and servicing [7]. In order to conduct complete object inspections, time optimal attitude reorientation becomes essential, especially if the inspection period is short due to the relative velocity of the inspecting spacecraft and object of interest.

Completing spacecraft attitude reorientations in a safe manner is paramount due to limited on orbit resources and high launch costs. Efficiency in conducting reorientations is also critical due to the limited amount of energy able to be stored and utilized by a given spacecraft for completing reorientations. The concept of reachability helps make this task of maneuvering safely and efficiently a reality. Reachability, which is related to controllability, has played a central role in the history of modern control theory [8]. The general concept of reachability is fairly simple, answering

the question: Can a certain final desired state be reached from a given initial state? Figure 1 helps to visualize this concept. Part (a) of Figure 1 visualizes the total ad-

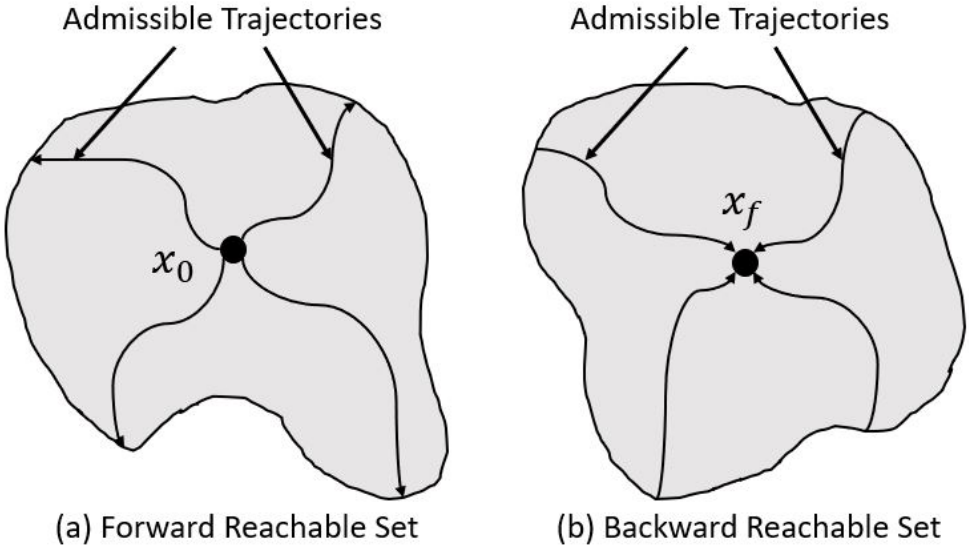

Figure 1. Illustration of Forward and Backward Reachable Sets

missible final states given a single starting initial condition, which is described as the concept of "forward" reachability. Part (b) of Figure 1 visualizes the total admissible initial states given a single desired final state, which is described as the concept of "backward" reachability. The research conducted in this thesis investigates backward reachability for spacecraft reorientation maneuvers. The goal is to find an initial set of conditions that, given certain constraints and an admissible amount of control, will be able to reach a desired end state.

1.2 Problem Statement

The focus of this research is to compute and visualize reachable sets for different spacecraft attitude reorientations. While the concept of reachability is fairly simple, the computation and visualization of reachable sets is fairly complex. Reachable sets have been exactly computed using Hamilton-Jacobi formulations, but are com-

putationally expensive, and problems with approximately 4 or greater dimensions become intractable [9]. However, geometric approximations of reachable sets provide estimates of reachable sets in significantly reduced computational time.

Due to the relationship between reachability and time-optimal control [10], the reachable sets will be generated from the solutions of time-optimal reorientation problems. This research focuses on utilizing GPOPS-II, an optimization problem solver used for a multitude of time-optimal control problems. The solutions to these optimization problems are then used to visually depict the reachable sets in the form of time-correlated contours related to the starting orientation of a spacecraft. Once these reachable sets are generated and depicted in a visually beneficial manner, the problem of formulating an optimal control policy will be investigated.

1.3 Research Questions

In order to provide answers to the problem, the research is divided into three different questions defined below that will be answered in this thesis:

1. Given a desired end state and bounded control input, what are the possible initial conditions (reachable sets) for successfully completing a reorientation maneuver in a given amount of time?

2. How do the linearized equations of rotational motion match the nonlinear dynamics?

3. Assuming the end state is reachable, what is the optimal control required to achieve the desired end state?

The first research question will utilize GPOPS-II to provide reachable sets with both quaternion and MRP nonlinear and linearized dynamics of the spacecraft reorientation as the basis of the solver. The second research question uses analysis of the

reachable sets to determine the validity of the linearized dynamics compared to the nonlinear dynamics. The final research question uses the knowledge of the linearized dynamics to provide the basis of the derivation of an optimal control policy.

1.4 Organization of the Thesis

Chapter II includes relevant previous research in the areas of time-optimal reorientation, reachability analysis, and previous work in applying reachability analysis to spacecraft maneuvering. Methods of generating reachable sets specifically applied to attitude reorientation, as well as the optimal control problem formulation for a time-optimal reorientation are presented in Chapter III. The results and analysis of the reachable sets generated, as well as the development of an optimal control policy, are detailed in Chapter IV. Finally, Chapter V summarizes the findings of the research, and includes recommendations for further work.

II. Background

2.1 Introduction

The work presented in this thesis is the generation of reachable sets for a spacecraft attitude reorientation and use of these reachable sets to generate an optimal control for the reorientation. This chapter surveys the relevant literature in the areas required to conduct this research. The review begins with the fundamentals of attitude parameterization as well as the kinematics and dynamics involved with spacecraft reorientation. An overview of spacecraft optimal reorientation is presented to provide a basis for finding an optimal control for a desired attitude slewing maneuver. Next, the theory of reachability and its application to spacecraft maneuvering is discussed to provide the foundation of the motivation behind this research.

2.2 Fundamentals of Spacecraft Attitude Kinematics and Dynamics

2.2.1 Attitude Parameters and Kinematics

Attitude parameters are a set of values that describe the orientation of a rigid body relative to a certain reference frame. There are an infinite number of ways to represent the attitude of a rigid body, similarly to how there is an infinite number of ways to describe the translational coordinates of a body (ex. Cartesian, polar, etc.). However, the translational difference between two points can approach infinity, whereas the difference between two different attitudes is at most 360° [4]. Choosing how to express a reorientation is essential in avoiding complicated mathematical formulations or singularities in those formulations. To help determine which set of parameters should be chosen, the following list containing rules about rigid body attitude coordinates is provided from [4].

1. A minimum of three coordinates is required to describe the relative angular displacement between two reference frames F_1 and F_2.

2. Any minimal set of three attitude coordinates will contain at least one geometrical orientation where the coordinates are singular, namely at least two coordinates are undefined or not unique.

3. At or near such a geometric singularity, the corresponding kinematic differential equations are also singular.

4. The geometric singularities and associated numerical difficulties can be avoided altogether through a regularization. Redundant sets of four or more coordinates exist which are universally determined and contain no geometric singularities.

One of the most fundamental formulations of attitude parameters is the Principal Rotation Vector, commonly referred to as Euler's principal rotation. This stems from Euler's Eigenaxis Rotation Theorem, which states the general rotational displacement of a rigid body with a fixed point is a rotation about an axis ($\hat{e}$) through that point and particular angle (ϕ), which makes it one of the simplest ways to describe a rotation. This theorem is depicted in Figure 2.

Euler's eigenaxis and angle is a non-minimum representation of a reorientation due to having four parameters (e_1, e_2, e_3, ϕ). The disadvantages of using Euler's Principal Rotation are that the parameters are not independent since the vector components of $\hat{e}$ must abide by the unit norm constraint, and each representation is a non-unique representation. One representation $(\hat{e}, \phi)$ can be represented either with $(-\hat{e}, -\phi)$ or with the original $\hat{e}$ and $\phi \pm 2k\pi$ for all $k = 0, 1, 2, ...$ [4].

One of the most common ways to represent a reorientation stems from the Euler axis and angle, and are referred to as Euler parameters, or commonly called quaternions. Quaternions provide a redundant, non-singular attitude parameterization, and

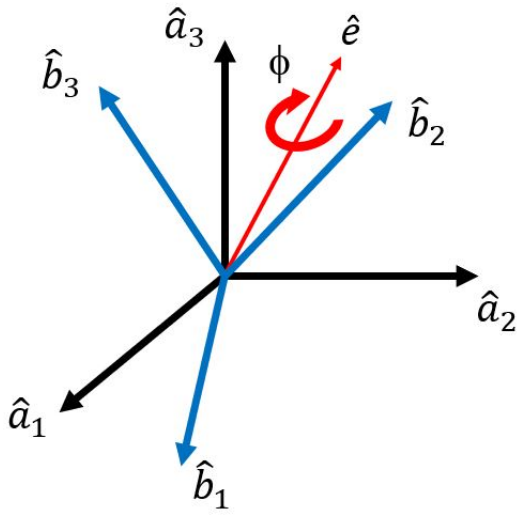

Figure 2. Illustration of Euler's Principal Rotation Theorem

are well suited for large rotations. Another representation rising in popular use are the Modified Rodriguez Parameters, which are a minimum representation set, and are well suited for attitude reorientations less than 360° [4]. Quaternions and Modified Rodriguez Parameters are the representations used in this thesis, the formulations of which are discussed in more detail below.

Quaternions are used for their computational efficiency and freedom from singularities. MRPs are used because of their ability to linearize well up to approximately 60 degrees of rotation, because they are a minimum representation of attitude, and because they have a singularity at 2π radians as opposed to other representations such as Euler angles or the classical Rodrigues parameters which have singularities at smaller angles of rotation. The spacecraft will only be subjected to attitude reorientations at or below π radians for all of the simulations which avoids this singularity.

Quaternions are composed of a vector and scalar part. This thesis will represent quaternions as $\boldsymbol{q} = [q_1\ q_2\ q_3\ q_4]^T = [\bar{q}\ q_4]^T$ where $\bar{q}$ is the vector part and q_4 is the scalar part. Each element is defined in terms of the Euler axis and angle:

$$q_1 = e_1 \sin\frac{\phi}{2} \tag{1}$$

$$q_2 = e_2 \sin\frac{\phi}{2} \tag{2}$$

$$q_3 = e_3 \sin\frac{\phi}{2} \tag{3}$$

$$q_4 = \cos\frac{\phi}{2} \tag{4}$$

where $\hat{e}$ is the Euler axis of rotation, and ϕ is the rotation angle. Given a certain attitude, there are actually two sets of quaternions that describe the same attitude, $\boldsymbol{q}$ and $-\boldsymbol{q}$. This is due to the non-uniqueness of the principal rotation elements, where switching between $(\hat{e}, \phi)$ and $(-\hat{e}, -\phi)$ will yield the same quaternion [4]. This dual representation can be avoided by ensuring the q_4 parameter is non-negative, and therefore the shortest reorientation is described by the chosen quaternion.

Quaternions avoid the presence of singularities by using a fourth parameter. The addition of a parameter, however, makes the quaternion representation a non-minimum representation. This requires the unit norm constraint depicted in Equation 5:

$$\sqrt{q_1^2 + q_2^2 + q_3^2 + q_4^2} = 1 \tag{5}$$

The equation describing the quaternion kinematics of a rotating body reference frame, B, with respect to an inertial reference frame, N, is given by [4]:

$$\dot{\boldsymbol{q}} = \frac{1}{2} Q \boldsymbol{\omega}_{BN} \tag{6}$$

where

$$Q = \begin{bmatrix} q_4 & -q_3 & q_2 & q_1 \\ q_3 & q_4 & -q_1 & q_2 \\ -q_2 & q_1 & q_4 & q_3 \\ -q_1 & -q_2 & -q_3 & q_4 \end{bmatrix} \tag{7}$$

and $\boldsymbol{\omega}_{BN}$ is the angular velocity vector of the B reference frame with respect to the N reference frame.

In order to have a minimum representation of the attitude, MRPs are used as an alternative to quaternions. MRPs are a stereographic projection of the set of unit quaternions (a four-dimensional unit sphere) onto a three-dimensional hyperplane [5]. The MRP vector in this thesis is represented as $\boldsymbol{\sigma} = [\sigma_1 \ \sigma_2 \ \sigma_3]^T$, where the three parameters are defined by $\sigma_i = \frac{q_i}{1+q_4}$ for $i = 1, 2, 3$. MRPs can also be defined in terms of the Euler axis and angle:

$$\boldsymbol{\sigma} = \hat{e} \ \tan \frac{\phi}{4} \tag{8}$$

It is apparent in Equation 8 that a singularity occurs at $\phi = \pm 2\pi$.

Similar to quaternions, two different MRPs can correspond to the same reorientation. The second MRP is referred to as the "shadow" MRP, $\boldsymbol{\sigma}^S$, and corresponds to the orientation given by $-\boldsymbol{q}$. This "shadow" MRP is a distinct set of MRPs, separate from the traditional MRP set ($\boldsymbol{\sigma} \neq \boldsymbol{\sigma}^S$). The existence of the shadow MRP allows for a switch to occur between $\boldsymbol{\sigma}$ and $\boldsymbol{\sigma}^S$ at $\phi = \pi$ (i.e. orientations where $\phi \leq \pi$ are represented by $\boldsymbol{\sigma}$, and orientations where $\phi \geq \pi$ are represented by $\boldsymbol{\sigma}^S$). One can arbitrarily switch between the original and shadow set of MRPs on the switching surface $\boldsymbol{\sigma}^T \boldsymbol{\sigma} = 1$, which provides a non-singular (at 180°), bounded, minimum attitude description [4]. The equation describing the MRP kinematics of a rotating body

reference frame, B, with respect to an inertial frame, N, is given [4]:

$$\dot{\boldsymbol{\sigma}} = \frac{1}{4} B \boldsymbol{\omega}_{BN} \tag{9}$$

where

$$B = \begin{bmatrix} 1 - \sigma^2 + 2\sigma_1^2 & 2(\sigma_1\sigma_2 - \sigma_3) & 2(\sigma_1\sigma_3 + \sigma_2) \\ 2(\sigma_2\sigma_1 + \sigma_3) & 1 - \sigma^2 + 2\sigma_2^2 & 2(\sigma_2\sigma_3 - \sigma_1) \\ 2(\sigma_3\sigma_1 - \sigma_3) & 2(\sigma_3\sigma_2 + \sigma_1) & 1 - \sigma^2 + 2\sigma_3^2 \end{bmatrix} \tag{10}$$

and σ^2 is $\boldsymbol{\sigma}^T\boldsymbol{\sigma}$.

2.2.2 Rigid Body Dynamics

The previous section described the rotational kinematic equations for a rigid spacecraft, defining how the attitude will evolve without considering the cause of the motion. Of course, most spacecraft need some sort of outside force in the form of an active control to be able to change the attitude of a spacecraft in order to complete its mission. There are several different methods of actively maneuvering a spacecraft, including: thrusters, momentum-exchange devices (i.e. momentum wheels, reaction wheels, control moment gyros, etc.), or magnetorquers. This research remains actuator-agnostic and assumes that torques are available along the primary axes of the spacecraft.

The fundamental equation of dynamics is the total torque ($\boldsymbol{\tau}$ acting on a body about the center of mass) is related to the time derivative of the total angular momentum $\dot{\boldsymbol{H}}$ about the center of mass, i.e. $\dot{\boldsymbol{H}} = \boldsymbol{\tau}$. If there are no torques applied to the body, then angular momentum is conserved. Taking the time derivative of the total angular momentum with respect to an inertial reference frame, N, and applying the transport theorem to resolve the equations in the body reference frame, B, results

in:

$$\dot{\boldsymbol{H}} = \frac{^N d}{dt}\boldsymbol{H} = \frac{^B d}{dt}\boldsymbol{H} + \boldsymbol{\omega}_{BN} \times \boldsymbol{H} \tag{11}$$

Wie [11] derives the expression for the total angular momentum using the inertia matrix of a rigid body, J, resolved in the body reference frame, to be $\boldsymbol{H} = J\boldsymbol{\omega}_{BN}$. Plugging this expression into Equation 11, assuming rigid body motion, and recognizing that $\frac{^B d}{dt}J = 0$ and $\frac{^B d}{dt}\boldsymbol{\omega}_{BN} = \frac{^N d}{dt}\boldsymbol{\omega}_{BN} = \dot{\boldsymbol{\omega}}_{BN}$, we get the equation for the rotational dynamics for a rigid body resolved in the B reference frame:

$$J\dot{\boldsymbol{\omega}}_{BN} + \left[\boldsymbol{\omega}_{BN}^{\times}\right](J\boldsymbol{\omega}_{BN}) = \boldsymbol{\tau} \tag{12}$$

where,

$$\left[\boldsymbol{\omega}_{BN}^{\times}\right] = \begin{bmatrix} 0 & -\omega_3 & \omega_2 \\ \omega_3 & 0 & -\omega_1 \\ -\omega_2 & \omega_1 & 0 \end{bmatrix} \tag{13}$$

This fundamental equation of rotational dynamics paired with the kinematic expressions for the quaternion and MRP equations of motion provide the basis for the dynamics used in this thesis.

2.3 Optimal Reorientation

Large-angle attitude maneuvers of spacecraft have been of great interest since the 1960's, with the testing of attitude determination and control [12]. Research in large-angle attitude maneuvers then gained significant traction in the area of executing such maneuvers optimally [13, 14, 15]. Rapid retargeting may be a part of a given spacecraft's mission set, or it may be needed to correct or calibrate the guidance and navigation sensors of the spacecraft.

As discussed previously, one of the simplest ways to reorient a spacecraft is via a

single rotation about the required Euler axis as laid out in [16] according to Euler's Eigenaxis Rotation Theorem. In fact, the Apollo Command and Service Modules were both reoriented with single rotations about an Euler axis [17]. However, such maneuvers, especially for non-spherically symmetric spacecraft, are not necessarily control or time optimal. Dixon *et al.* [18] showed that single axis maneuvers for an axisymmetric spacecraft are not fuel optimal. Bilimoria and Wie show that for non-spherically symmetric spacecraft, and for spherically symmetric spacecraft with independent control constraints, the eigenaxis maneuver is not time-optimal [1].

Junkins *et al.* [14] were the first to formally present a non-singular formulation of the necessary conditions for optimal large-angle rotational maneuvers for an asymmetric, generally tumbling spacecraft. Junkins and Turner went on to write a book on *Optimal Spacecraft Rotational Maneuvers*, wherein they present the elements of optimal control theory and their relation to spacecraft reorientation maneuvers, as well as the formulation of an optimal control policy for large angle maneuvers of a single rigid body while minimizing the total control effort [19]. Several authors have further delved into the research of providing optimal control policies for spacecraft, either optimizing the control effort or time to complete a reorientation. However, to the author's knowledge, no time-optimal control policy has been presented which is applicable to all symmetries of a rigid body spacecraft. This thesis seeks to fill this gap using the knowledge of the reachable sets, maneuvering trajectories, and relationship between the nonlinear and linearized rotational dynamics explored in the author's research.

In order to solve for the optimal control of a reorientation, the optimal control problem must first be formulated. The general optimal control problem formulation

without path constraints is given as:

$$\mathrm{J} = \phi\left(\boldsymbol{x}(t_f), t_f\right) + \int_{t_0}^{t_f} \mathcal{L}\left(\boldsymbol{x}(t), \boldsymbol{u}(t), t\right) dt \tag{14}$$

where J is the cost functional in the Bolza form, and is constrained by the dynamics:

$$\dot{\boldsymbol{x}}(t) = \boldsymbol{f}\left(\boldsymbol{x}(t), \boldsymbol{u}(t), t\right) \tag{15}$$

with path constraints:

$$\boldsymbol{k}\left(\boldsymbol{x}(t), \boldsymbol{u}(t), t\right) \leq 0 \tag{16}$$

where $[t_0, t_f]$ is the time interval of interest, $\boldsymbol{x} : [t_o, t_f] \Rightarrow \mathbb{R}^{n_x}$ is the state vector, $\boldsymbol{u} : [t_o, t_f] \Rightarrow \mathbb{R}^{n_u}$ is the control vector, J is the cost functional, ϕ is the terminal cost, $\mathcal{L}$ is the Lagrange function (or running cost), and $\boldsymbol{k}$ is the general expression for an algebraically constrained parameter.

The two major areas of optimal control for reorientations are in regards to minimizing the control effort spent on completing the maneuver, or minimizing the time taken to complete the maneuver. The latter of the two is the focus for this research, thereby making time the performance measure the optimal control problem seeks to minimize. This makes the formulation for the simple cost functional:

$$\mathrm{J} = \int_{t_0}^{t_f} 1 dt \tag{17}$$

where there is no terminal cost included in the optimization, and the Lagrange function, $\mathcal{L}$, is equal to 1. However, the dynamics of the reorientation of a rigid body are nonlinear, making the problem difficult to solve, and formulation of an optimal control policy even more difficult. There are various ways to solve nonlinear optimization problems. In particular, "Direct Methods" approximate the optimal control problem

through some form of discretization, and transcribe it to a nonlinear programming (NLP) problem [20]. One such method is called direct collocation, which is a method that parameterizes both the states and the control, allowing for flexibility with constraints on the control path. Direct collocation can yield a sparse nonlinear program, which is ideal, because several solvers already exist for sparse NLPs.

One prevalent optimization tool available is GPOPS-II: a commercially available, variable-order Gaussian quadrature collocation software [21]. Collocation points are placed as the roots to orthogonal Legendre polynomials, and Lagrange interpolating polynomials are used to approximate the state and control trajectories where Gaussian quadrature is used for numerical integration [21]. SNOPT [22], which stands for sparse nonlinear optimizer and is used for large scale nonlinear optimization problems, was used for all scenarios. This tool is ideal for solving the reorientation problems needed in this research quickly, because the dynamics are nonlinear, and there are not constraints besides the dynamics on the path of the reorientation, which slow down the computation of the optimal solution.

However, as will be shown in Chapter IV, there is an opportunity to use the linearized rotational dynamics for derivation of an optimal control policy. Since the dynamics are linear, it is not necessary to use direct methods to help derive this policy. Instead, the traditional, indirect methods for solving an optimal control problem can be used. Indirect methods develop first-order necessary conditions for an optimal solution through the calculus of variations laid out by Kirk in [20]. In his book, Kirk defines the necessary conditions of optimality as shown in Equations 18-20:

$$\dot{\boldsymbol{x}}(t) = \frac{\partial \mathcal{H}}{\partial \boldsymbol{\lambda}} \tag{18}$$

$$\dot{\boldsymbol{\lambda}}(t) = -\frac{\partial \mathcal{H}}{\partial \boldsymbol{x}} \tag{19}$$

$$0 = \frac{\partial \mathcal{H}}{\partial \boldsymbol{u}} \tag{20}$$

where the Hamiltonian ($\mathcal{H}$) is defined by $\mathcal{H} = \mathcal{L} + \lambda^T f$, the states are denoted by $\boldsymbol{x}$, the costates are denoted with $\boldsymbol{\lambda}$ (which deviates from Kirk's notation of using $\mathbf{p}$ for the costates), and the control is denoted with $\boldsymbol{u}$. The problem also has the boundary conditions:

$$\begin{aligned} &\left[\frac{\partial \phi}{\partial \boldsymbol{x}}(\boldsymbol{x}^*(t_f), t_f) - \boldsymbol{\lambda}^*(t_f)\right]^T \delta \boldsymbol{x_f} + \\ &\quad \left[\mathcal{H}(\boldsymbol{x}^*(t_f), \boldsymbol{u}^*(t_f), \boldsymbol{\lambda}^*(t_f), t_f) + \frac{\partial \phi}{\partial t}(\boldsymbol{x}^*(t_f), t_f)\right] \delta t_f = 0 \end{aligned} \tag{21}$$

These necessary conditions along with the boundary conditions of the optimal control problem provide the basis of the formulation of the optimal control problem in Chapter IV.

2.4 Reachability Theory and Application

2.4.1 Reachability Theory

While there is extensive research in controlling spacecraft attitude via various different methods, almost no work has been done on characterizing the initial conditions from which attitude maneuvers can be accomplished safely. Spacecraft are typically very complex systems, which increases the need to determine whether they will perform according to expectation and specification. As a result, verification becomes essential in developing spacecraft and determining the spacecraft's maneuverability. Since all possible system behaviors must be accounted for, most simulation methods

are insufficient due to the typical drawback of requiring significant computational resources of simulating the entire space of interest [23]. This leads to the requirement of a more formal verification method [24, 25]. Reachability provides a formal verification method for guaranteeing performance and safety for a given maneuver.

Reachability has its roots in optimal control theory, and has been studied extensively for discrete time systems, motivated by the importance for control in the presence of constraints [26, 27]. In reachability analyses, a reach-avoid set is calculated. This reach-avoid set contains the admissible states from which a system can reach a final end state, while adhering to constraints on the system. Outside of these constraints is the "inadmissible" or "unsafe" state space region. Traditionally, reachability analysis involves solving a Hamilton-Jacobi partial differential equation. Hamilton-Jacobi reachability is applicable to general non-linear systems, it easily handles control and disturbance variables, and is able to represent sets of arbitrary shapes [24]. However, solving Hamilton-Jacobi partial differential equations is very complex computationally, and limited to low-dimensional systems [9]. To avoid this computational complexity, a second major category of methods has been implemented in research to generate reachable sets: geometric approximations.

Geometric approximation involves approximating a convex set with a geometric shape, typically depicted in the form of ellipsoids, polytopes or zonotopes, and then propagating this set according to the systems dynamics [28]. The use of ellipsoids has been extensively used in the approximation of reachable sets, and is a desirable option since it is requires less computational complexity compared to generating sets comprised of polytopes or zonotopes (centrally symmetric polytopes) [29]. While geometric approximations may not be able to visually produce the full reachable set, specifically for systems with more than 2 dimensions, taking slices of these sets are still helpful in visualizing the reachable set of a system.

The author takes a slightly different approach to generating reachable sets than the previously discussed methods. Instead of computing the complete reachable set via solving the Hamilton-Jacobi equations, or by approximating the sets geometrically, a hybrid approach is introduced. This approach uses a method utilizing the relationship between optimal control and reachability.

Reachability analysis shows if a given desired state, x_f, is reachable from an initial state, x_0, then at least one admissible trajectory exists [10]. It is very likely for reorientations that more than one admissible trajectory exists. If multiple admissible trajectories do exist, it follows that one of these trajectories minimizes a certain performance index. The performance index of interest in this research is time. This leads to the requirement of the existence of a time-optimal trajectory, highlighting the relationship between optimal control and reachability. The control solution that results in this time-optimal trajectory is defined as the time-optimal control solution. GPOPS-II is used to solve these time-optimal trajectories and control solutions.

The reachability analysis conducted herein utilizes these time-optimal control solutions applied to a variety of initial conditions. Each initial condition is then correlated to the time generated from its optimal reorientation solution. This creates a grid of solutions from which all initial conditions can be interpolated to generate time-optimal contours. These time-optimal contours depict the reachable sets of attitude reorientations. The goal behind generating these time optimal reachable sets is to produce a visual product that operators can use. For a given spacecraft symmetry, desired angle of rotation, and limited control, an operator could tell how long it would take to complete a reorientation, which would inform the decision of whether or not to even attempt it. In future autonomous applications, the spacecraft itself could either store the time to complete a reorientation on-board, or quickly compute the feasibility of a reorientation, and decide whether or not to complete the maneuver.

2.4.2 Reachability Application to Spacecraft Maneuvering

There have been several applications of reachability to spacecraft mission sets. Holzinger and Scheeres [30] use reachability to validate the safety of general spacecraft proximity operations in Low Earth Orbit (LEO) and Geostationary Orbit (GEO). Lesser *et al.* [31] examine the calculation of stochastic reachable sets, and apply that to the specific problem of rendezvous and docking. Lee and Hwang [32] compute ellipsoidal reachable set approximations for spacecraft formations to validate the safety of formation flying. Chen *et al.* [33] apply the concept of forward-reachability to solving for the reachable domain of a spacecraft with a single impulse. Hess and Zagaris [34] used ellipsoidal approximations of reachable sets applied to spacecraft single impulse maneuvers. Chernick *et al.* [35] use reachable set theory to minimize the delta-v cost of impulsive control maneuvers for use in spacecraft relative orbit reconfiguration. Zagaris and Romano [28, 36] generated polytopic sets for a spacecraft docking with a rotating body in close proximity, and then extended this to computing the reachable sets for a rendezvous with a tumbling object. Bayadi *et al.* [37] explore calculating reachable sets of a spacecraft with two rotors by looking at the possible angular velocities that can be achieved. However, as mentioned in Section **2.3.1**, no work to the author's knowledge has been done on formally characterizing the time-optimal reachable sets for attitude reorientations of a satellite.

2.4.3 Summary

This chapter discussed the relevant literature on the topics of spacecraft reorientation, optimization, and reachability. The foundational mathematics were provided that will be used to generate the reachable sets for spacecraft attitude reorientations, as well as the framework for the development of an optimal control policy for reorientation maneuvers.

III. Methodology

This chapter outlines the methodology used to formulate reachable sets for a spacecraft reorientation. The rotational motion of the spacecraft is described both in terms of quaternions and modified Rodrigues parameters (MRPs). To set up the time-optimal reorientation problem that is the basis for constructing the reachable sets, the cost functional and constraints are derived from the dynamics the spacecraft is subject to. Finally, the starting conditions for the formulation of an optimal control policy from the linearized MRP dynamics is developed.

3.1 Rotational Dynamics

3.1.1 Spacecraft Model

Three different symmetries of rigid body spacecraft are examined to study the differences in reachable sets: spherically symmetric, axially symmetric, and asymmetric/triaxial. A spherically symmetric body has the same symmetry about all principal axes, i.e. $J_{xx} = J_{yy} = J_{zz}$. An axially symmetric body has the same symmetry about one of the axes, i.e. $J_{xx} = J_{yy}$, $J_{xx} = J_{zz}$, or $J_{yy} = J_{zz}$. Asymmetric, or triaxial, bodies exhibit no symmetry, i.e. $J_{xx} \neq J_{yy} \neq J_{zz}$. The inertia matrix J, and its inverse J^{-1}, in a principal body frame are defined as:

$$J = \begin{bmatrix} J_{xx} & 0 & 0 \\ 0 & J_{yy} & 0 \\ 0 & 0 & J_{zz} \end{bmatrix}, \quad J^{-1} = \begin{bmatrix} \frac{1}{J_{xx}} & 0 & 0 \\ 0 & \frac{1}{J_{yy}} & 0 \\ 0 & 0 & \frac{1}{J_{zz}} \end{bmatrix} \tag{22}$$

Each model has the same mass, 200kg, and volume, 9m^3, to keep the densities the same. The mass is assumed to be equally distributed throughout the body. The symmetric body is a cube with a length, width, and height of 3 meters. The axially

symmetric body is a parallelepiped with a length of 6.75 meters, and width and height of 2 meters. The asymmetric body has a length of 4.5 meters, width of 3 meters, and height of 2 meters. The boresight of the spacecraft is arbitrarily defined to be along the x-axis of the body, or down the middle of the longest side of the spacecraft. The models of each of the spacecraft are depicted in Figure 3.

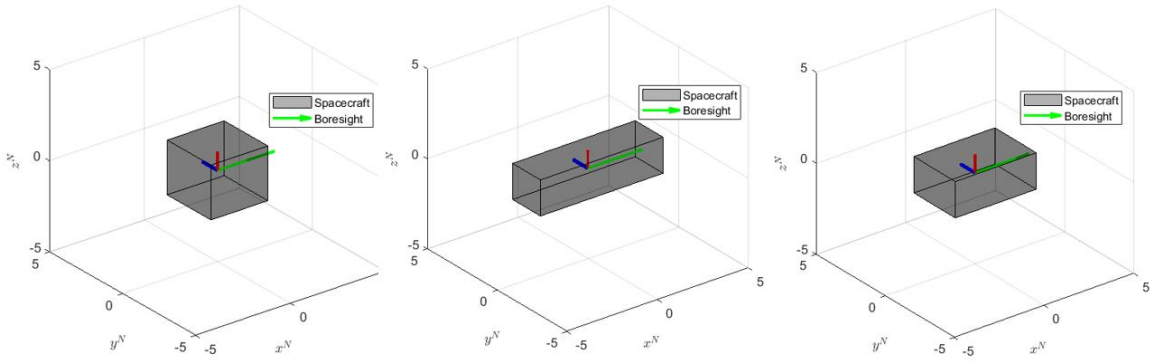

Figure 3. Models: Symmetric (left), Axially Symmetric (center), Asymmetric (right)

3.1.2 Dynamics Formulation

The two parameterizations used to compute the reachable sets are taken from the quaternion and MRP kinematics (Eq. 6, 9) in conjunction with the standard rotational dynamics used for a rigid body (Eq. 12). MRPs linearize fairly well below 90 degrees of rotation as discussed in [38]. In order to linearize the MRP dynamics listed in Equations 9 and 10, the region near an equilibrium point is investigated. The quaternion dynamics are also linearized for comparison according to the same process. The dynamics given in Equations 6, 7, 9 and 10 are in the form:

$$\dot{\boldsymbol{x}} = \boldsymbol{f}(\boldsymbol{x}) \tag{23}$$

where $\boldsymbol{x} = [\boldsymbol{\omega}\ \boldsymbol{\sigma}]$.

Suppose that $\boldsymbol{x}^*$ is an equilibrium point such that $f(\boldsymbol{x}^*) = 0$. Expanding the right

side of Equation 23 via a Taylor series expansion about $\boldsymbol{x}^*$ yields:

$$\dot{\boldsymbol{x}} = \boldsymbol{f}(\boldsymbol{x}^*) + \left.\frac{\partial \boldsymbol{f}}{\partial \boldsymbol{x}}\right|_{\boldsymbol{x}^*} (\boldsymbol{x} - \boldsymbol{x}^*) + ... \tag{24}$$

$$= \left.\frac{\partial \boldsymbol{f}}{\partial \boldsymbol{x}}\right|_{\boldsymbol{x}^*} (\boldsymbol{x} - \boldsymbol{x}^*) + ... \tag{25}$$

The partial derivative in Equation 25 is in this case the Jacobian matrix. To linearize the dynamics, the Jacobian of the dynamics is determined, and evaluated at an equilibrium point. If the state vector $\boldsymbol{x}$ is defined as $x_1, x_2, ..., x_n$, and the vector $\boldsymbol{f}$ is defined as the derivatives $f_1, f_2, ..., f_n$, the Jacobian matrix of a system of equations is defined as:

$$Jac = \begin{bmatrix} \frac{\partial f_1}{\partial x_1} & \frac{\partial f_1}{\partial x_2} & \dots & \frac{\partial f_1}{\partial x_n} \\ \frac{\partial f_2}{\partial x_1} & \frac{\partial f_2}{\partial x_2} & \dots & \frac{\partial f_2}{\partial x_n} \\ \vdots & \vdots & \ddots & \vdots \\ \frac{\partial f_n}{\partial x_1} & \frac{\partial f_n}{\partial x_2} & \dots & \frac{\partial f_n}{\partial x_n} \end{bmatrix} \tag{26}$$

When applied to the MRP kinematics and dynamics, the Jacobian becomes:

$$Jac_{MRP} = \begin{bmatrix} \frac{\partial \dot{\omega}_1}{\partial \omega_1} & \frac{\partial \dot{\omega}_1}{\partial \omega_2} & \frac{\partial \dot{\omega}_1}{\partial \omega_3} & \frac{\partial \dot{\omega}_1}{\partial \sigma_1} & \frac{\partial \dot{\omega}_1}{\partial \sigma_2} & \frac{\partial \dot{\omega}_1}{\partial \sigma_3} \\ \frac{\partial \dot{\omega}_2}{\partial \omega_1} & \frac{\partial \dot{\omega}_2}{\partial \omega_2} & \frac{\partial \dot{\omega}_2}{\partial \omega_3} & \frac{\partial \dot{\omega}_2}{\partial \sigma_1} & \frac{\partial \dot{\omega}_2}{\partial \sigma_2} & \frac{\partial \dot{\omega}_2}{\partial \sigma_3} \\ \frac{\partial \dot{\omega}_3}{\partial \omega_1} & \frac{\partial \dot{\omega}_3}{\partial \omega_2} & \frac{\partial \dot{\omega}_3}{\partial \omega_3} & \frac{\partial \dot{\omega}_3}{\partial \sigma_1} & \frac{\partial \dot{\omega}_3}{\partial \sigma_2} & \frac{\partial \dot{\omega}_3}{\partial \sigma_3} \\ \frac{\partial \dot{\sigma}_1}{\partial \omega_1} & \frac{\partial \dot{\sigma}_1}{\partial \omega_2} & \frac{\partial \dot{\sigma}_1}{\partial \omega_3} & \frac{\partial \dot{\sigma}_1}{\partial \sigma_1} & \frac{\partial \dot{\sigma}_1}{\partial \sigma_2} & \frac{\partial \dot{\sigma}_1}{\partial \sigma_3} \\ \frac{\partial \dot{\sigma}_2}{\partial \omega_1} & \frac{\partial \dot{\sigma}_2}{\partial \omega_2} & \frac{\partial \dot{\sigma}_2}{\partial \omega_3} & \frac{\partial \dot{\sigma}_2}{\partial \sigma_1} & \frac{\partial \dot{\sigma}_2}{\partial \sigma_2} & \frac{\partial \dot{\sigma}_2}{\partial \sigma_3} \\ \frac{\partial \dot{\sigma}_3}{\partial \omega_1} & \frac{\partial \dot{\sigma}_3}{\partial \omega_2} & \frac{\partial \dot{\sigma}_3}{\partial \omega_3} & \frac{\partial \dot{\sigma}_3}{\partial \sigma_1} & \frac{\partial \dot{\sigma}_3}{\partial \sigma_2} & \frac{\partial \dot{\sigma}_3}{\partial \sigma_3} \end{bmatrix} \tag{27}$$

The quaternion version, which follows the same method but adds an additional state, is not be displayed for brevity. When evaluated at an equilibrium point, $\boldsymbol{x^*}$, chosen

to be,

$$\boldsymbol{x^*} = \begin{bmatrix} \omega_1^* \\ \omega_2^* \\ \omega_3^* \\ q_1^* \\ q_2^* \\ q_3^* \end{bmatrix} \text{ or } \begin{bmatrix} \omega_1^* \\ \omega_2^* \\ \omega_3^* \\ \sigma_1^* \\ \sigma_2^* \\ \sigma_3^* \end{bmatrix} = \begin{bmatrix} 0 \\ 0 \\ 0 \\ 0 \\ 0 \\ 0 \end{bmatrix} \tag{28}$$

where q_4 can be computed from q_1, q_2, and q_3 using the fact that $q_4 = \sqrt{1 - q_1^2 - q_2^2 - q_3^2}$ [39]. This results in:

$$Jac^*_{quat} = \begin{bmatrix} 0 & 0 & 0 & 0 & 0 & 0 \\ 0 & 0 & 0 & 0 & 0 & 0 \\ 0 & 0 & 0 & 0 & 0 & 0 \\ \frac{1}{2} & 0 & 0 & 0 & 0 & 0 \\ 0 & \frac{1}{2} & 0 & 0 & 0 & 0 \\ 0 & 0 & \frac{1}{2} & 0 & 0 & 0 \end{bmatrix} \text{ or, } Jac^*_{MRP} = \begin{bmatrix} 0 & 0 & 0 & 0 & 0 & 0 \\ 0 & 0 & 0 & 0 & 0 & 0 \\ 0 & 0 & 0 & 0 & 0 & 0 \\ \frac{1}{4} & 0 & 0 & 0 & 0 & 0 \\ 0 & \frac{1}{4} & 0 & 0 & 0 & 0 \\ 0 & 0 & \frac{1}{4} & 0 & 0 & 0 \end{bmatrix} \tag{29}$$

Where Jac^* signifies the Jacobian evaluated at an equilibrium point, $\boldsymbol{x}^*$. When there is no input to the system, this yields:

$$\dot{\boldsymbol{\omega}} = zeros(1,3) \tag{30}$$

$$\dot{\boldsymbol{q}} = \frac{1}{2} I_3 \boldsymbol{\omega} \tag{31}$$

$$\dot{\boldsymbol{\sigma}} = \frac{1}{4} I_3 \boldsymbol{\omega} \tag{32}$$

Where I_3 is defined as a 3x3 identity matrix. The result of the linearized quaternion dynamics are validated in [39]. When there is input to the system, as will be the case

for the maneuvers conducted, the angular velocity dynamics become:

$$\dot{\boldsymbol{\omega}} = J^{-1}\boldsymbol{u} \tag{33}$$

These equations are used to generate reachable sets for comparisons to the reachable sets generated with the nonlinear dynamics. The insights provided by this comparison are discussed in Chapter IV.

3.2 Optimal Control and Reachable Sets

3.2.1 Optimal Control Formulation

An optimal control problem is formulated for completing the minimum time reorientation. The formulation for this optimal control problem is given for the nonlinear and linear dynamics:

$$\min_{\boldsymbol{t_f}} \quad \mathrm{J} = \int_{t_0}^{t_f} dt \tag{34}$$

$$\text{s.t.} \quad \dot{\boldsymbol{\omega}}_{BN} = J^{-1}\left[-[\boldsymbol{\omega}_{BN}^{\times}](J\boldsymbol{\omega}_{BN}) + \boldsymbol{\tau}\right] \tag{35}$$

$$\dot{\boldsymbol{q}} = \frac{1}{2}Q\boldsymbol{\omega}_{BN}, \; or \quad \dot{\boldsymbol{\sigma}} = \frac{1}{4}B\boldsymbol{\omega}_{BN} \tag{36}$$

$$\text{or} \quad \dot{\boldsymbol{\omega}}_{BN} = J^{-1}\boldsymbol{u} \tag{37}$$

$$\dot{\boldsymbol{q}} = \frac{1}{2}I_3\boldsymbol{\omega}_{BN}, \; or \quad \dot{\boldsymbol{\sigma}} = \frac{1}{4}I_3\boldsymbol{\omega}_{BN} \tag{38}$$

$$\text{and} \quad \boldsymbol{q}^T\boldsymbol{q} = 1 \tag{39}$$

$$u_i \leq 1, \quad i = 1, 2, 3 \tag{40}$$

$$\text{or} \quad ||\boldsymbol{u}|| \leq 1 \tag{41}$$

where t_f is the final time, and the control has either a cubic ($u_i \leq 1, \;\; i = 1, 2, 3$) or spherical ($||\boldsymbol{u}|| \leq 1$) constraint.

3.2.2 Optimal Control Policy Development

Because the linearized dynamics are much simpler than the nonlinear dynamics, it is much easier to make a control law that is applicable universally for spherically symmetric, axisymmetric, and asymmetric rigid body spacecraft. Consider a series of rest-to-rest reorientations, where the initial and final angular velocities are both equal to zero in the inertial frame, and the final orientation of the spacecraft's boresight is aligned with the inertial $\hat{I}_x$ axis as depicted in Figure 4.

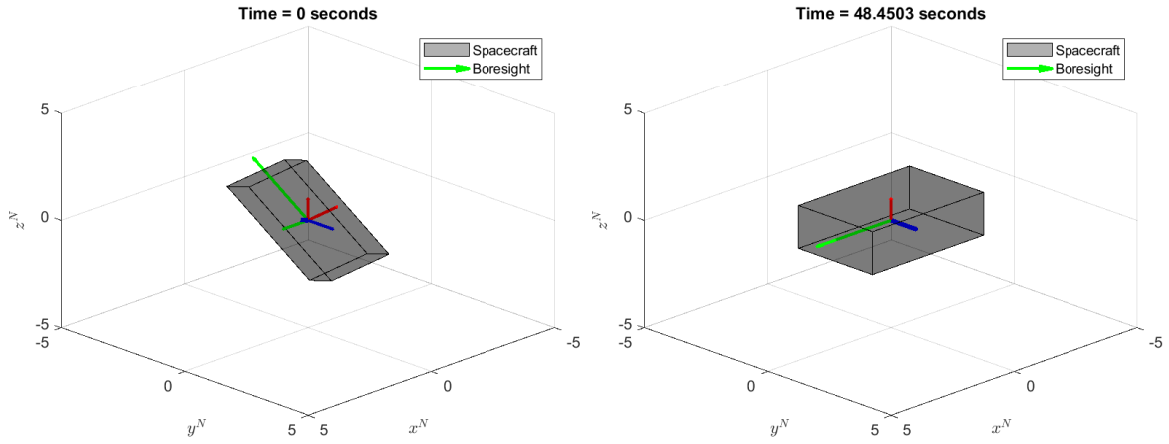

(a) Starting Attitude **(b) Final Attitude**

Figure 4. Example Attitude Reorientation of Spacecraft: Asymmetric Body

The boundary conditions for this two-point boundary value problem are given:

$$\omega_1(t_0) = \omega_2(t_0) = \omega_3(t_0) = 0 \tag{42}$$

$$\boldsymbol{\sigma}(t_0) = \boldsymbol{\sigma}_0 \tag{43}$$

$$\omega_1(t_f) = \omega_2(t_f) = \omega_3(t_f) = 0 \tag{44}$$

$$\sigma_1(t_f) = \sigma_2(t_f) = \sigma_3(t_f) = 0 \tag{45}$$

where it assumed the initial time is 0 and the final time is t_f, and the MRP at

t_0 ($\boldsymbol{\sigma}_0$) defines the initial orientation. Using MRPs instead of quaternions to solve the two-point boundary problem has the advantage of reducing the total number of states from 7 to 6, and therefore reducing the dimension of the problem including the costates from 14 to 12.

The initial MRPs are chosen from a set of points such that the angle between the initial attitude and final attitude is less than or equal to 90 degrees. The starting orientations are depicted as a section of the unit sphere in Figure 5, where x, y, and z are aligned with the inertial frame $\hat{I}_x$, $\hat{I}_y$, and $\hat{I}_z$. The goal of each reorientation

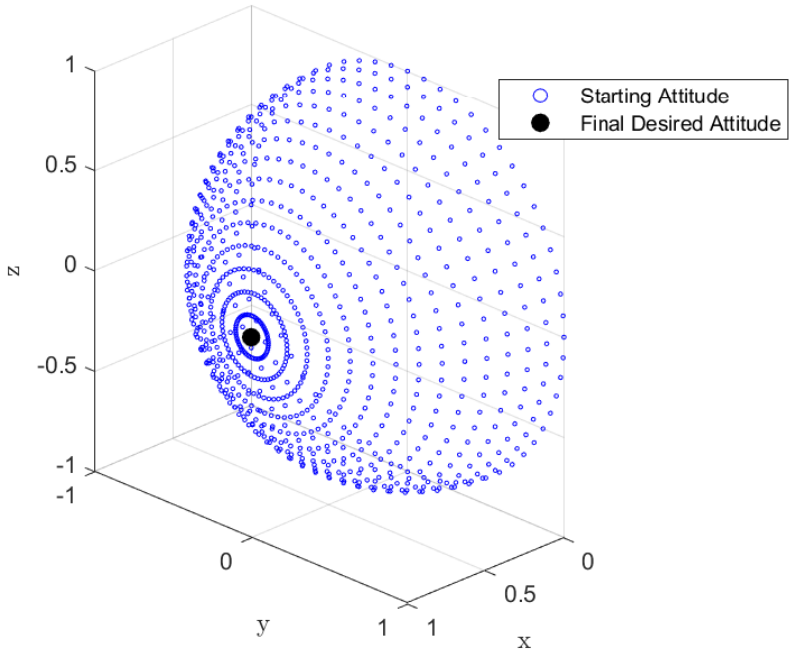

Figure 5. Depiction of Starting Conditions

maneuver, and the goal of the optimal control policy, is to start with the boresight pointed to a blue dot and perform a maneuver to point the boresight to the black dot depicted in Figure 5.

3.2.3 Optimal Control Solution

As seen in the cost functional J formulated in Equation 34, this optimal control problem seeks to complete the objective in the minimum amount of time from a given initial condition. The constraints that this problem is subject to are the dynamics of the system described in Section 2.2. The reorientation optimization problems are then solved using a GPOPS-II.

GPOPS-II requires an initial guess for the starting and final states, control, and time to complete the reorientation. Two different methods are used to provide an initial guess to GPOPS-II. The first method involved an iterative approach which is used to complete batches of optimization problems. Each batch has a certain set of dynamics (ex. nonlinear MRP, etc.). The first iteration uses an "educated guess" of the states and control at the initial and final times supplied to GPOPS-II, but every subsequent iteration uses the previous problem's solution as the initial guess. Since the previous solution is based off a very similar starting orientation to the current optimization problem, the guess provided to GPOPS-II is fairly accurate to the real solution. The second method is to generate an eigenaxis reorientation from each initial condition. This solution is determined using an eigenaxis quaternion feedback control law, derived in [40], as shown in Equation 46.

$$\boldsymbol{\tau} = -K\bar{\boldsymbol{q}}_e - C\boldsymbol{\omega} + \left[\boldsymbol{\omega}^{\times}\right] J\boldsymbol{\omega}, \tag{46}$$

where τ is the required torque to perform the maneuver, which is then limited between $-u_{max}$ and u_{max}. K and C are weighting matrices for tuning of the control. The parameter $\bar{\boldsymbol{q}}_e$ is the quaternion error between the actual quaternion and the desired

quaternion, and $\boldsymbol{\omega} = \boldsymbol{\omega}_{BN}$ since $\boldsymbol{\omega}_{des} = [0\ 0\ 0]^T$. The quaternion error is given by:

$$q_e = \begin{bmatrix} q_{4c} & q_{3c} & -q_{2c} & -q_{1c} \\ -q_{3c} & q_{4c} & q_{1c} & -q_{2c} \\ q_{2c} & -q_{1c} & q_{4c} & -q_{3c} \\ q_{1c} & q_{2c} & q_{3c} & q_{4c} \end{bmatrix} \begin{bmatrix} q_1 \\ q_2 \\ q_3 \\ q_4 \end{bmatrix} \tag{47}$$

where q_c is the commanded (desired) quaternion [4].

Both of these methods speed up the time it takes to complete the optimization problems, which is essential for reducing the computation time when thousands of optimization problems are to be solved in generation of the reachable sets. It was determined that the approach of using the previous solution as the guess for the subsequent iteration is slightly faster computationally, and yielded approximately the same results for the optimal solution as the eigenaxis reorientation solution method. This method is therefore used for all of the guesses of the optimal control solutions.

3.2.4 Reachable Set Generation

Following an iterative comparison process, different combinations of optimization problems are organized in batches according to dynamic equations used, symmetry of spacecraft, and control constraint. As discussed earlier in this chapter, there are four different types of dynamics, two types of control constraints, and three types of spacecraft symmetries, resulting in 24 different combinations to be compared. This translates to 43,920 optimization problems to be solved as depicted in Figure 6. All 24 reachable sets are displayed in Appendix A for reference, and certain ones will be depicted throughout the following chapters to highlight key findings and comparisons. In order to provide the most intuitive depiction of the reachable sets, the 3-dimensional state of MRPs is mapped onto a 2-dimensional plane of azimuth and el-

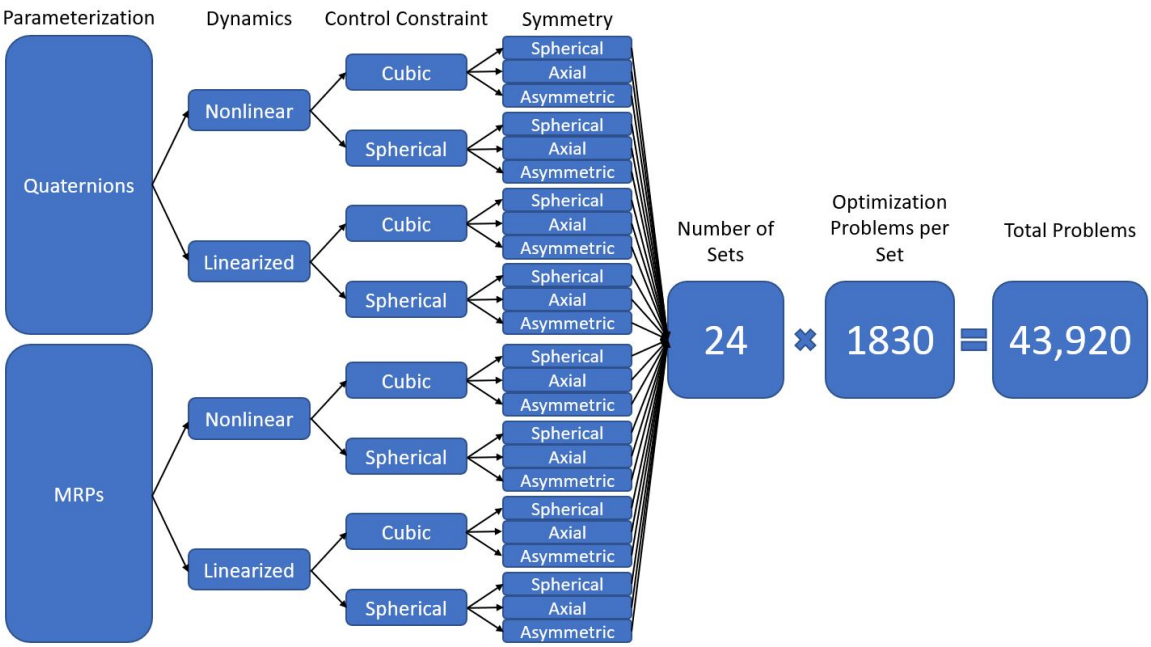

Figure 6. Reachable Set Organization Diagram

evation. Reorientations up to 90 degrees are depicted because, as will be shown later, the linearized dynamics become increasingly invalid at angles beyond approximately 60 degrees.

3.3 Summary

The objective of the outlined scenarios is to generate reachable sets for reorientation maneuvers. These sets will be produced for different spacecraft symmetries, and will be based off of the minimum time solutions to complete a reorientation given a set of initial conditions. The goal is to visually depict these reachable sets in a manner that is useful to operators in determining how long it will take to perform a reorientation from a given starting condition. It is also a goal to investigate a potential control law derived from linearized MRP dynamics and principles of optimality.

IV. Results and Analysis

This chapter presents the results and analysis of the reachable sets for different spacecraft models. It is divided into three major subsections. First, a comparison between various reachable sets is discussed. Second, the computational efficiency of generating the reachable sets is assessed. Last, an optimal control law derived from the linearized MRP dynamics is presented for spacecraft attitude reorientations.

4.1 Reachable Sets

4.1.1 Reachable Set Generation

For an introduction to the products of reachable sets being generated, an example of two different sets are shown in Figure 7. Depicted in Figure 7 are time optimal

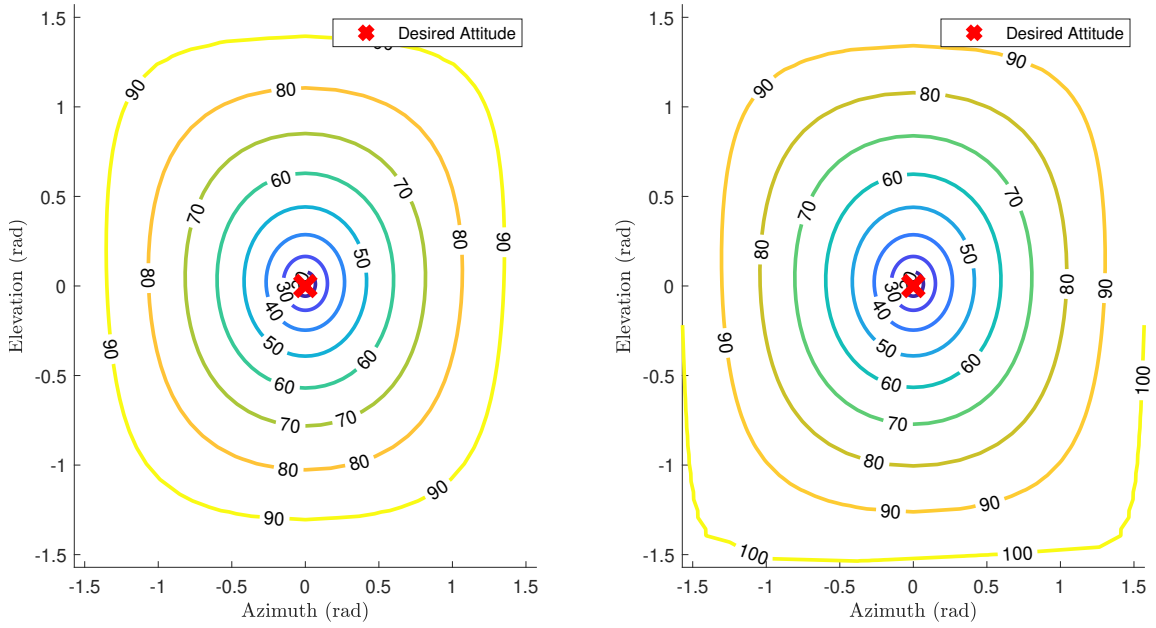

Figure 7. Reachable Sets Depicted as Time Optimal Contours from MRP dynamics, Nonlinear (left) and Linear (right) of Spherically Symmetric Body with Spherical Control Constraint

contours of reorientation times to maneuver using the nonlinear dynamics of motion compared to the linearized dynamics. The red "x" in the center depicts the targeted final attitude state, in this case, aligned with the x-axis of the inertial frame which is specifically defined by the boundary conditions given in Chapter III. To determine how long it would take to complete a maneuver, one would go to a certain azimuth and elevation, and then determine the contour on which the point lies. For example, if a spacecraft is starting with an azimuth of 0 radians and an elevation of 1 radian from the final attitude, it would take the spacecraft approximately 78 seconds to maneuver to the desired attitude. The contours depicted in Figure 7 demonstrate the transition of contours from being completely circular to becoming more square-like in shape. This is due to the 3-dimensional space being mapped to a 2-dimensional space of azimuth and elevation, which takes up the entire square plot. This mapping is depicted in Figure 8. The azimuth and elevation could be converted to another attitude parameterization if desired.

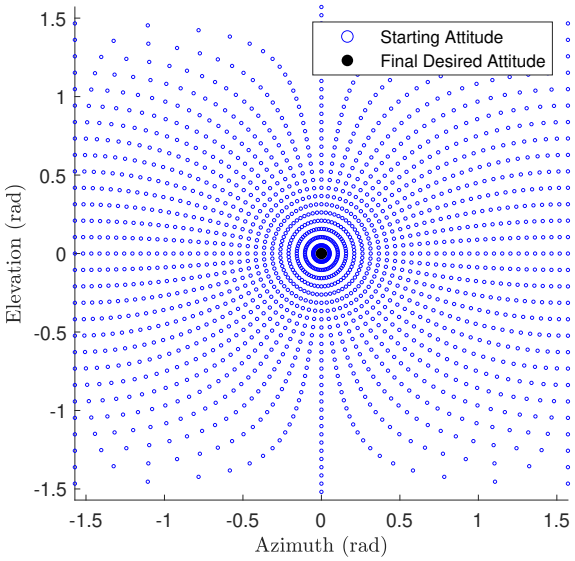

Figure 8. Starting Attitudes Mapped to Azimuth and Elevation

4.1.2 Reachable Set Accuracy

In order to determine if the optimal control problem solutions being output by GPOPS-II are accurate, the solutions are propagated through a numerical integration solver, ode45, in MATLAB. The control history generated from the supposed optimal solution is applied via simulation to the starting attitude conditions of the spacecraft, and the nonlinear dynamics are used to propagate the result from applying the control history. In order to see the maximum error, the starting conditions farthest from the desired end state (90 degrees of rotation) are examined in Figure 9.

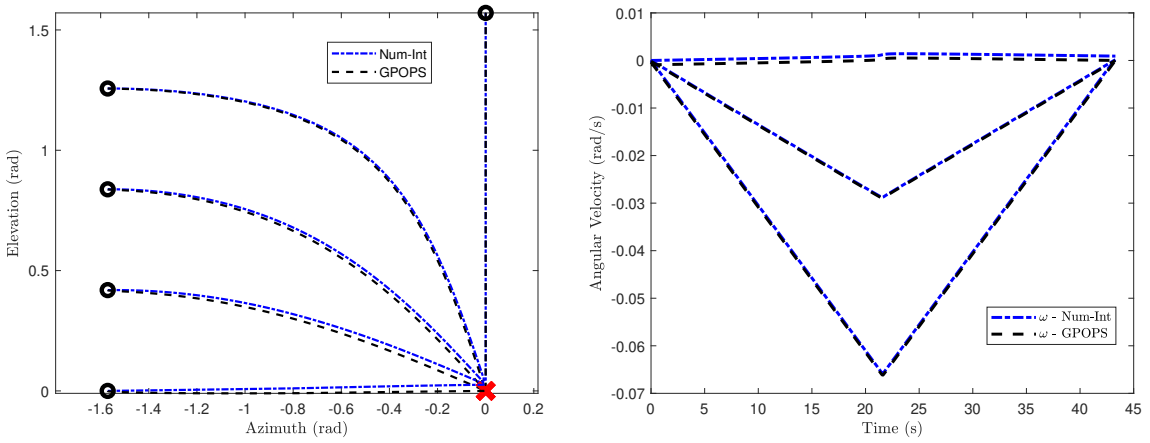

(a) Boresight Trajectory **(b) Angular Velocity from Trajectory 4**

Figure 9. Propagated Solutions Compared to GPOPS-II Solutions: Nonlinear MRP Dynamics with a Spherically Symmetric Body and Spherical Control Constraint

It is seen in Figure 9 that the nonlinear propagations of the selected trajectories slightly differ from the solutions output by GPOPS-II. In other words, the commanded control output from GPOPS-II does not exactly produce the desired end state. However, this error is less than 2 degrees in pointing error, and less than 0.115 deg/sec in angular velocity error from the desired end state for all trajectories. This error decreases as the magnitude of the rotation is decreased. In order to test getting closer to the optimal solution, different tolerances are used in the setup of GPOPS-II, different solver types are used, all of which significantly slowed down the computation times of

the reachable sets without producing noticeable differences in getting to the desired end state. The only parameter that helped get closer to the end state is increasing the control authority of the spacecraft, but to get very close to the desired end state, an unrealistic amount of control authority (>10 Nm) is required. Even though the exact optimal solution is not generated for the trajectories, it is deemed close enough to accurately approximate the time optimal solutions of the reorientations. An alternate NLP solver, IPOPT [41], was used to attempt to get a more accurate solution from GPOPS-II, but this method produced results that were indistinguishable from the results produced when using SNOPT.

4.1.3 MRP vs. Quaternion Reachable Sets

One of the first areas of interest is how the reachable sets generated from the MRP dynamics compared to the quaternion dynamics compared. The following six figures are shown for the comparison of how the nonlinear dynamics compare with one another for all three spacecraft symmetries.

As seen in Figures 10-15, the sets appear to be identical. This is expected because both types of nonlinear dynamics are valid for all reorientations, and neither have singularities in the region of interest. Any discrepancies between the sets are most likely due to the interpolation between the actual optimal times calculated.

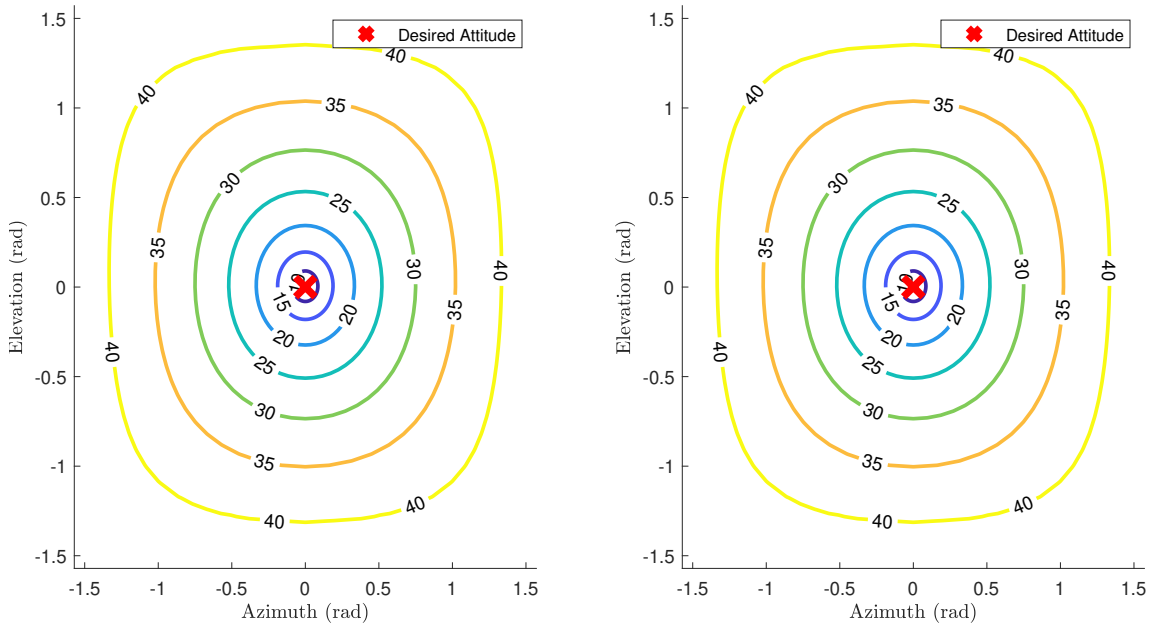

Figure 10. MRP (left) vs Quaternion (right) Sets with Nonlinear Dynamics for a Spherically Symmetric Body and Spherical Control Constraint

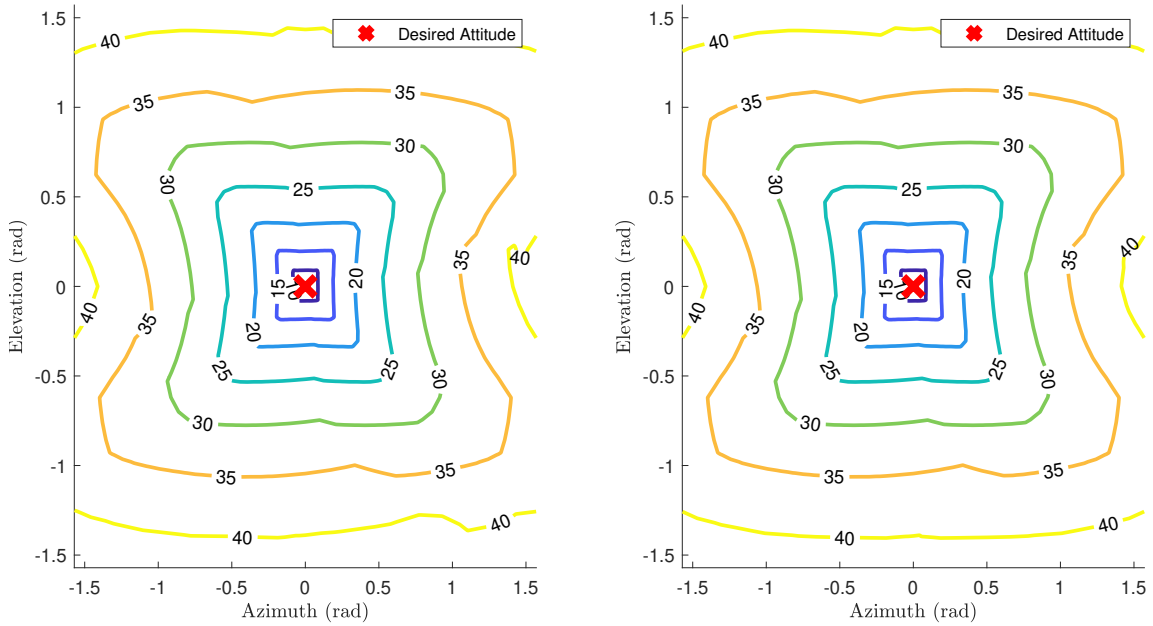

Figure 11. MRP (left) vs Quaternion (right) Sets Depicted as Time Optimal Contours with Nonlinear Dynamics for a Spherically Symmetric Body and Cubic Control Constraint

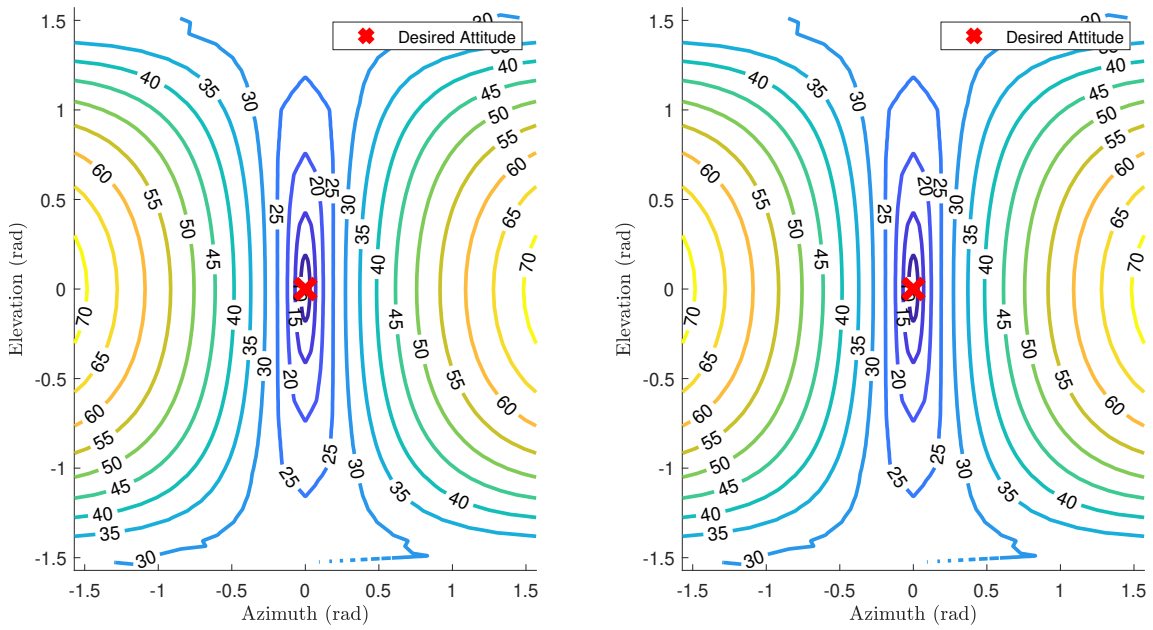

Figure 12. MRP (left) vs Quaternion (right) Sets Depicted as Time Optimal Contours with Nonlinear Dynamics for an Axisymmetric Body and Spherical Control Constraint

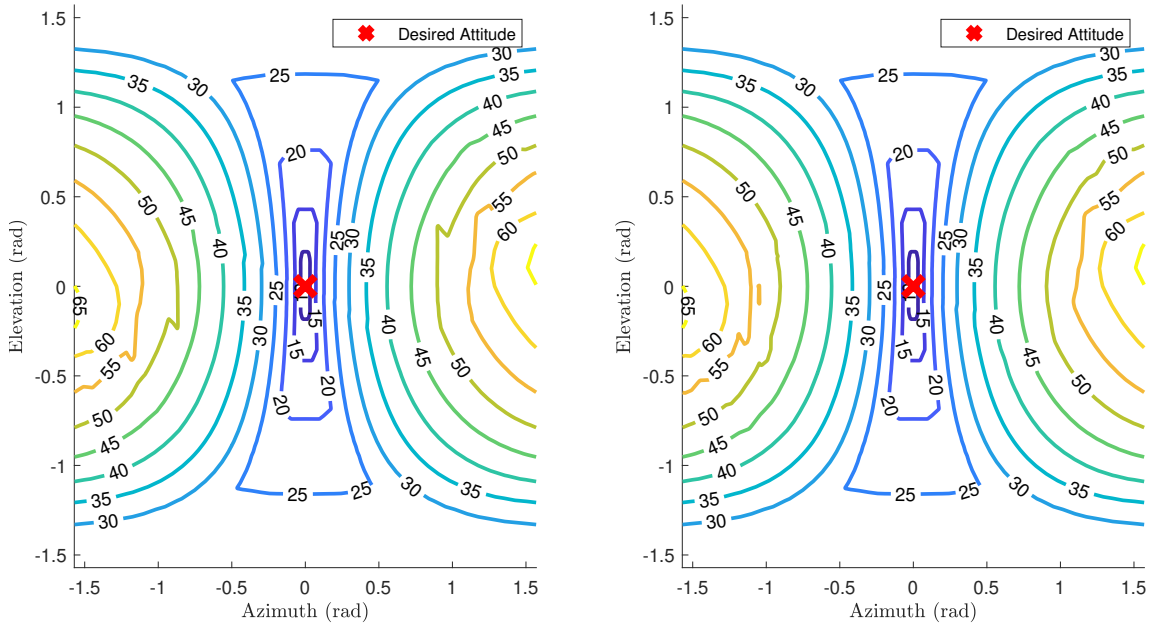

Figure 13. MRP (left) vs Quaternion (right) Sets Depicted as Time Optimal Contours with Nonlinear Dynamics for an Axisymmetric Body and Cubic Control Constraint

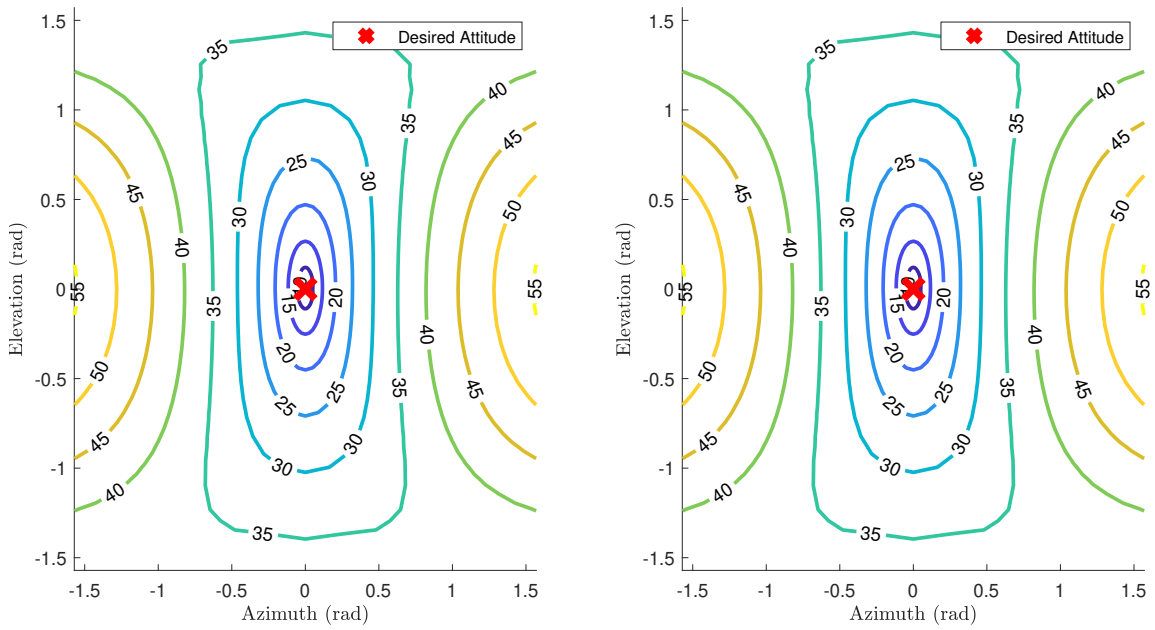

Figure 14. MRP (left) vs Quaternion (right) Sets Depicted as Time Optimal Contours with Nonlinear Dynamics for an Asymmetric Body and Spherical Control Constraint

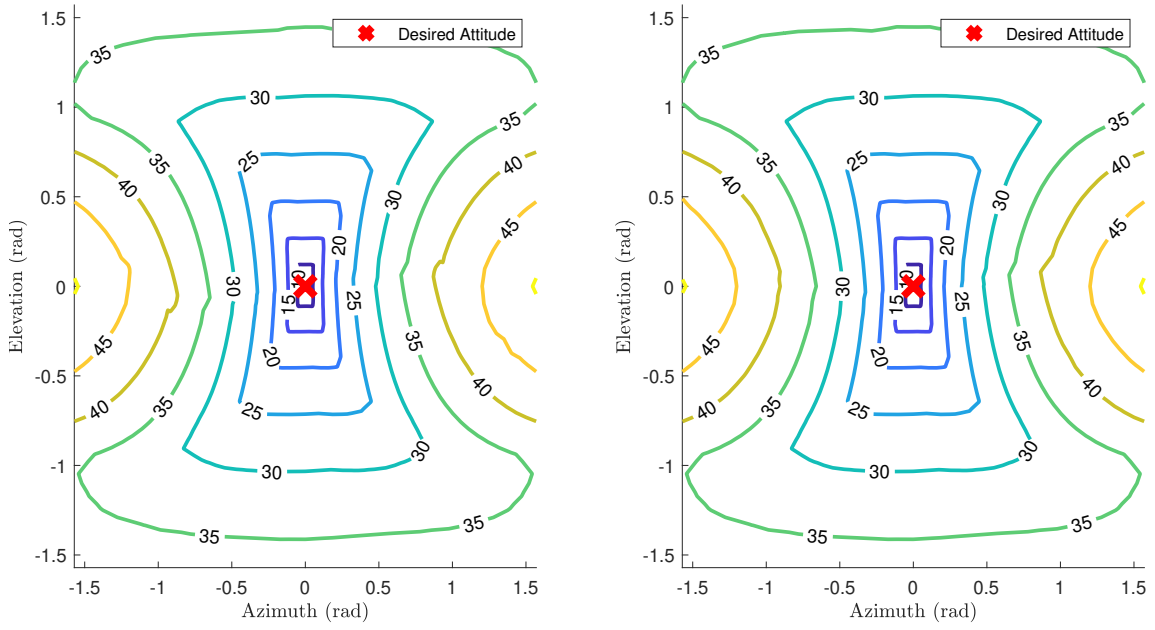

Figure 15. MRP (left) vs Quaternion (right) Sets Depicted as Time Optimal Contours with Nonlinear Dynamics for an Asymmetric Body and Cubic Control Constraint

The next area of interest is a comparison of the sets generated with the linearized dynamics with the sets generated with nonlinear dynamics. Figures 16-21 show the comparisons of both linearized dynamic outputs compared to the nonlinear outputs.

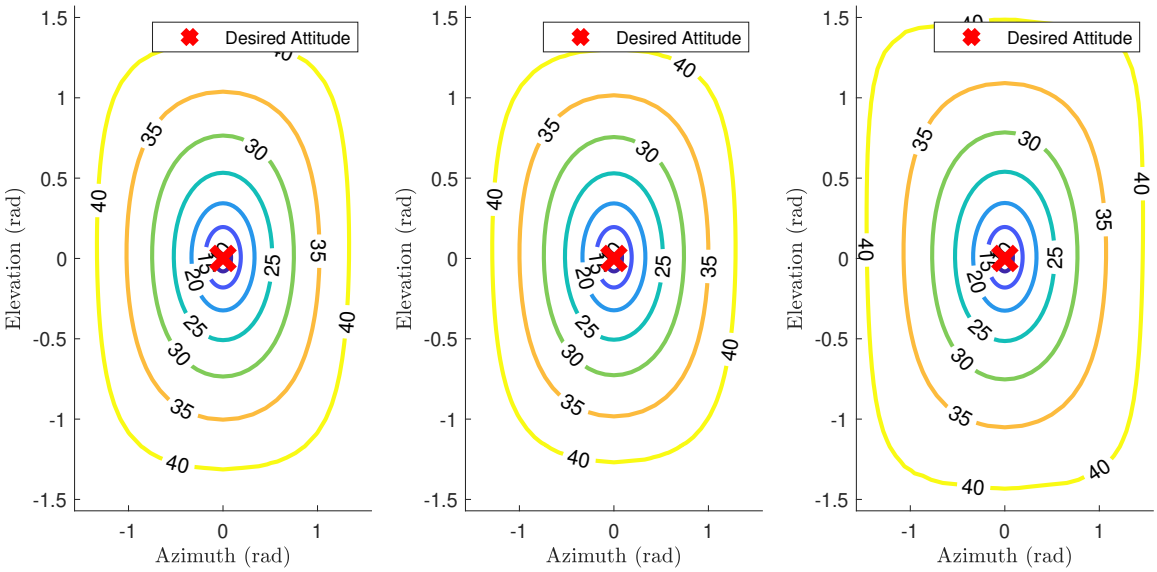

Figure 16. Nonlinear (left) vs Linearized MRP (center) and Linearized Quaternion (right) Dynamics Sets Depicted as Time Optimal Contours for a Spherically Symmetric Body and Spherical Control Constraint

As seen in Figures 16-21, the reachable sets produced using the linearized versions of both the MRP and quaternion dynamics closely match the sets produced with the nonlinear dynamics. The linearized MRP reachable are more conservative than the nonlinear dynamics (i.e. the length of time at a certain starting attitude is predicted to take longer with the linearized MRP sets than the nonlinear sets), and the linearized quaternions are less conservative. The linearized MRP dynamics are more conservative, have less states than the quaternion dynamics, and are better than the linearized quaternion dynamics at predicting the nonlinear dynamics according to [38]. Therefore, the linearized MRP dynamics will be the only dynamics used henceforth.

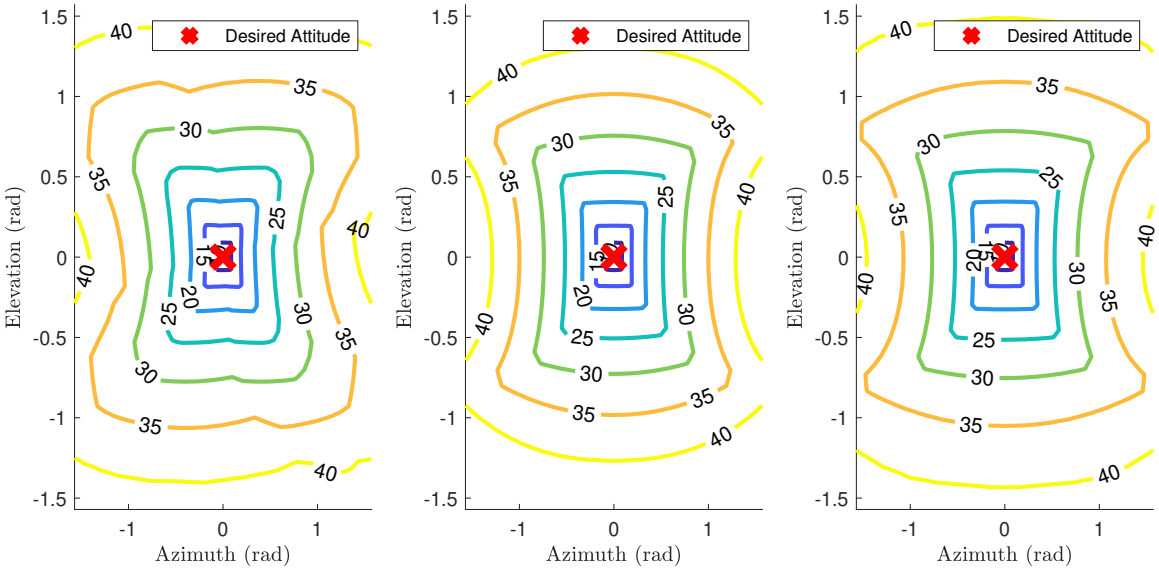

Figure 17. Nonlinear (left) vs Linearized MRP (center) and Linearized Quaternion (right) Dynamics Sets Depicted as Time Optimal Contours for a Spherically Symmetric Body and Cubic Control Constraint

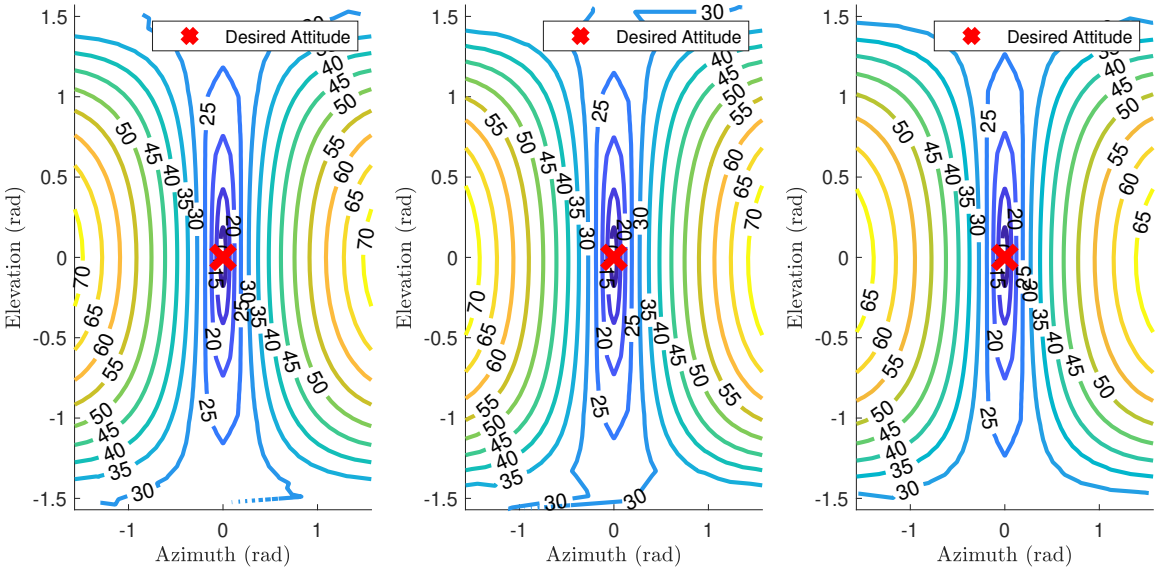

Figure 18. Nonlinear (left) vs Linearized MRP (center) and Linearized Quaternion (right) Dynamics Sets Depicted as Time Optimal Contours for an Axisymmetric Body and Spherical Control Constraint

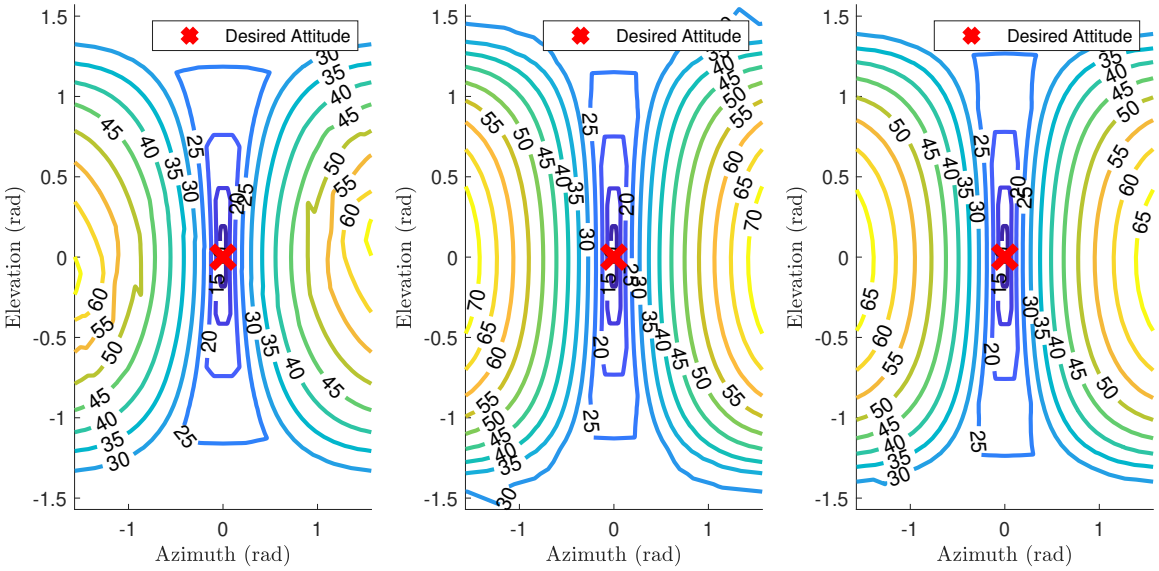

Figure 19. Nonlinear (left) vs Linearized MRP (center) and Linearized Quaternion (right) Dynamics Sets Depicted as Time Optimal Contours for a Axisymmetric Body and Cubic Control Constraint

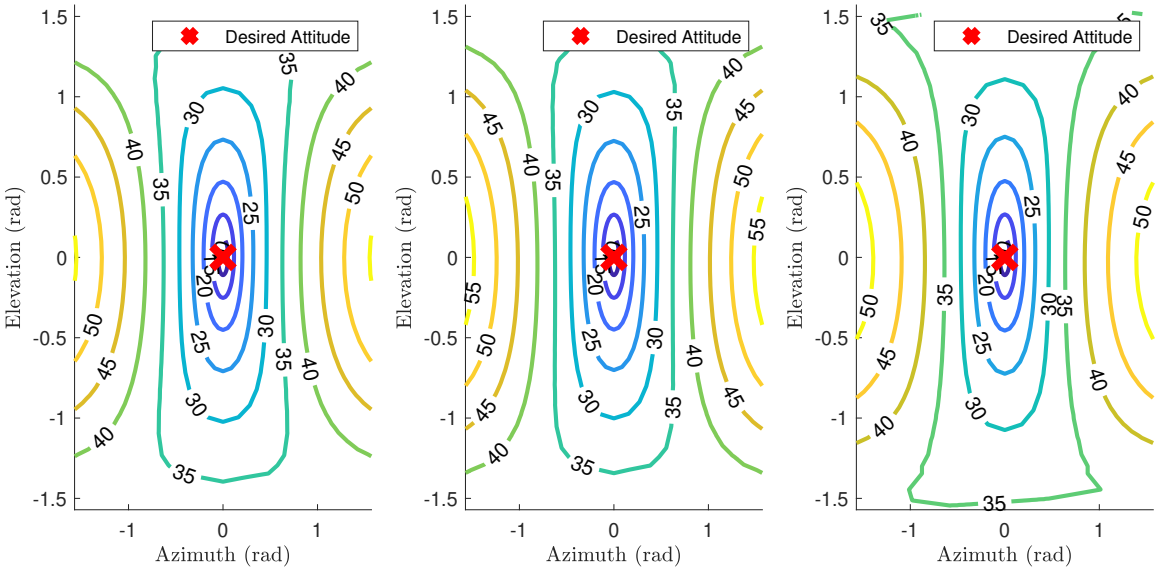

Figure 20. Nonlinear (left) vs Linearized MRP (center) and Linearized Quaternion (right) Dynamics Sets Depicted as Time Optimal Contours for an Asymmetric Body and Spherical Control Constraint

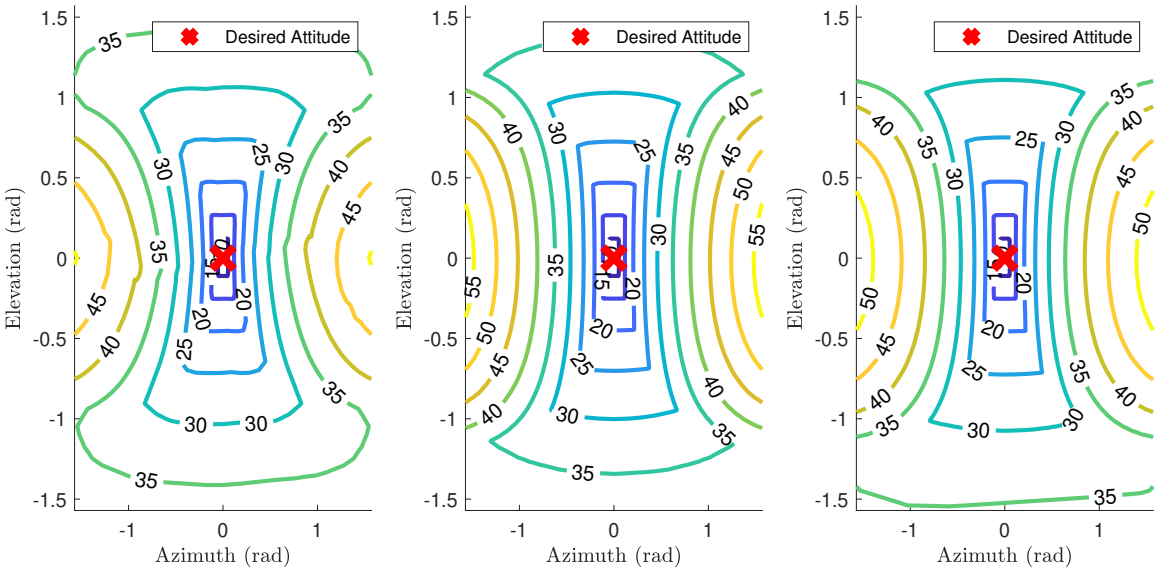

Figure 21. Nonlinear (left) vs Linearized MRP (center) and Linearized Quaternion (right) Dynamics Sets Depicted as Time Optimal Contours for an Asymmetric Body with Cubic Control Constraint

4.1.4 Differing Control Constraints

In Section 4.1.3, both the spherical and cubic control constraints are depicted. It is useful to do a deeper dive into the comparison of these different control constraints for development of an optimal control policy, and to determine if both constraints provide accurate solutions with the linearized dynamics compared to the nonlinear dynamics. By simply looking at the reachable sets in Figures 16-21, it appears that both the spherical and cubic constraints provide decently accurate representations of optimal times to maneuver given a variety of initial conditions.

However, it is important to observe the actual maneuvers of the spacecraft during the time-optimal reorientation to determine if the linearized dynamics provide a valid solution for the maneuvers. In order to visualize the maneuvers provided from the optimal solution output, the 2-dimensional path of the boresight vector is plotted on top of the reachable sets. The boresight trajectory numbers henceforth will be referred to as trajectory 1-5, starting with the top to bottom trajectory labeled as

trajectory 1, and then consecutively counterclockwise with the trajectory starting at an elevation of 0 radians labeled trajectory 5. An example of these trajectories for a spherically symmetric body is depicted in Figure 22. The trajectories depicted in

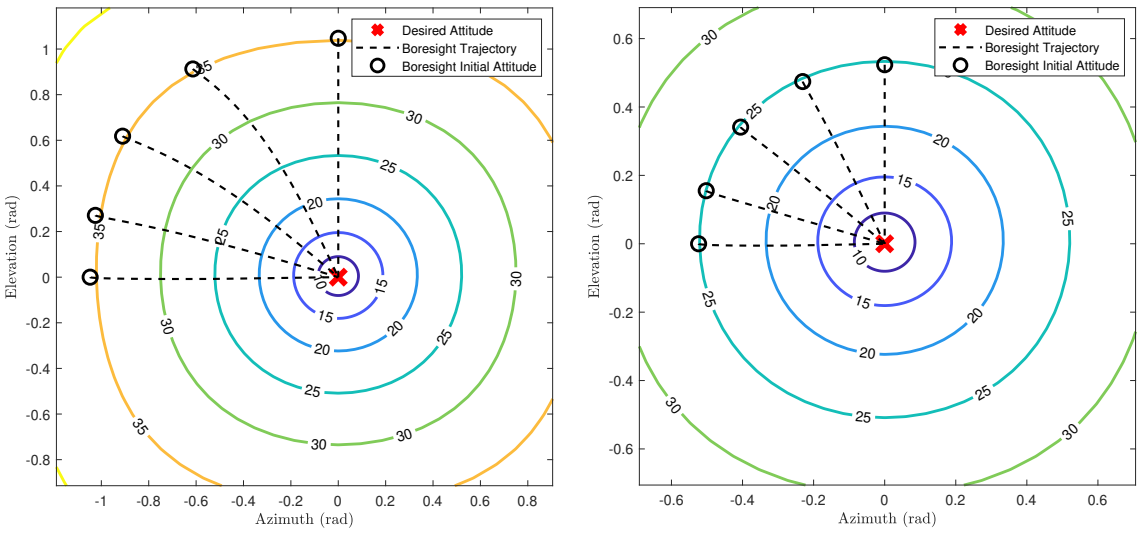

(a) 60 Degree Reorientations **(b) 30 Degree Reorientations**

Figure 22. Boresight Trajectories and Time Optimal Contours: Nonlinear MRP Dynamics, Asymmetric Body with Spherical Control Constraint

Figure 22 depict eigenaxis maneuvers, which matches the proven optimal solution for a spherically symmetric body [42]. The trajectories are not shown as straight lines due to the 2-dimensional mapping phenomenon depicted in Figure 8.

Asymmetric bodies are specifically studied because if an optimal control policy can be applied to this most complex case, then it can also be applied to spherically symmetric and axially symmetric bodies. As depicted in Figure 23, if the control has the spherical constraint, all of the linearized trajectories closely match the nonlinear trajectories, even up to 90 degrees. There are some discrepancies though, as the trajectories computed using the nonlinear dynamics have more concavity than the linearized result. The region for which the linearized dynamics provide a more accurate solution will be further investigated later.

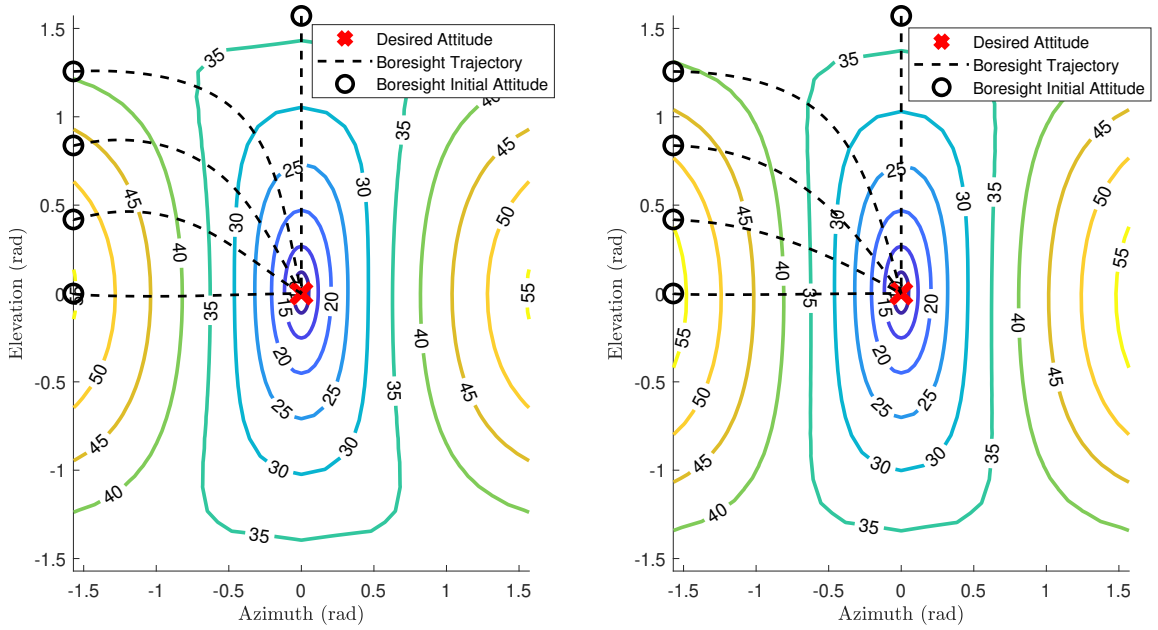

Figure 23. Boresight Trajectories and Time Optimal Contours Starting at 90 Degrees from Final Attitude of Nonlinear (left) and Linearized (right) Dynamics: Asymmetric Body with Spherical Control Constraint

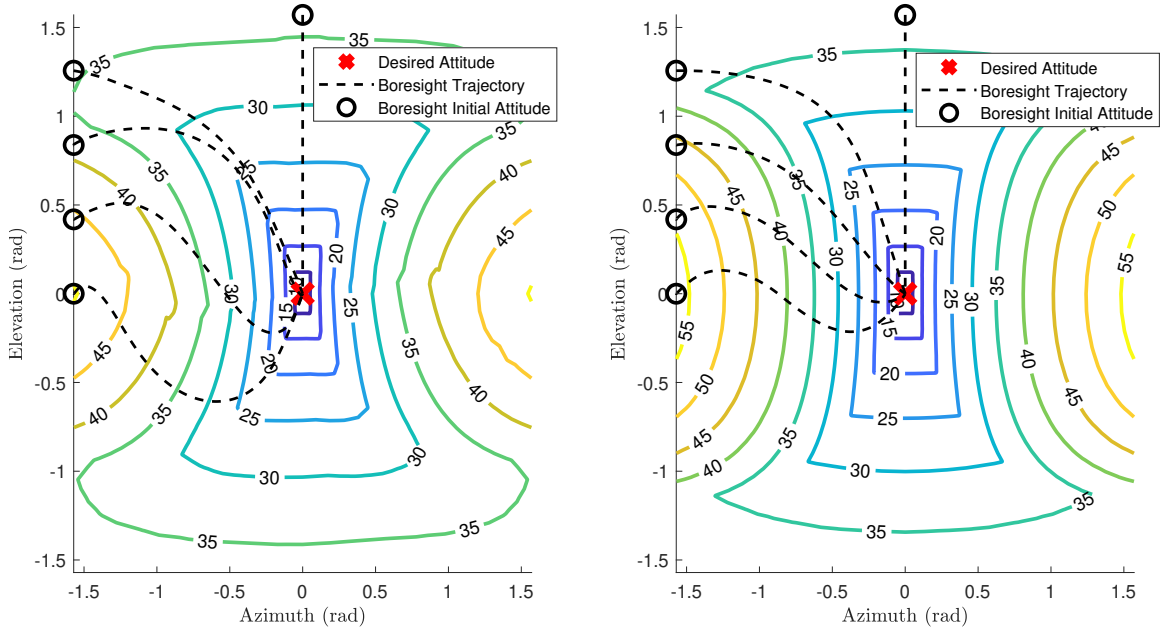

Figure 24. Boresight Trajectories and Time Optimal Contours Starting at 90 Degrees from Final Attitude of Nonlinear (left) and Linearized (right) Dynamics: Asymmetric Body with Cubic Control Constraint

However, as depicted in Figure 24, when the control is bounded by the cubic constraint, some of the trajectories are vastly different from the linearized version compared to the nonlinear version. This may just be due to the magnitude of the angle between the starting and ending attitudes, so starting conditions closer to the desired final attitude are examined in Figures 25-27.

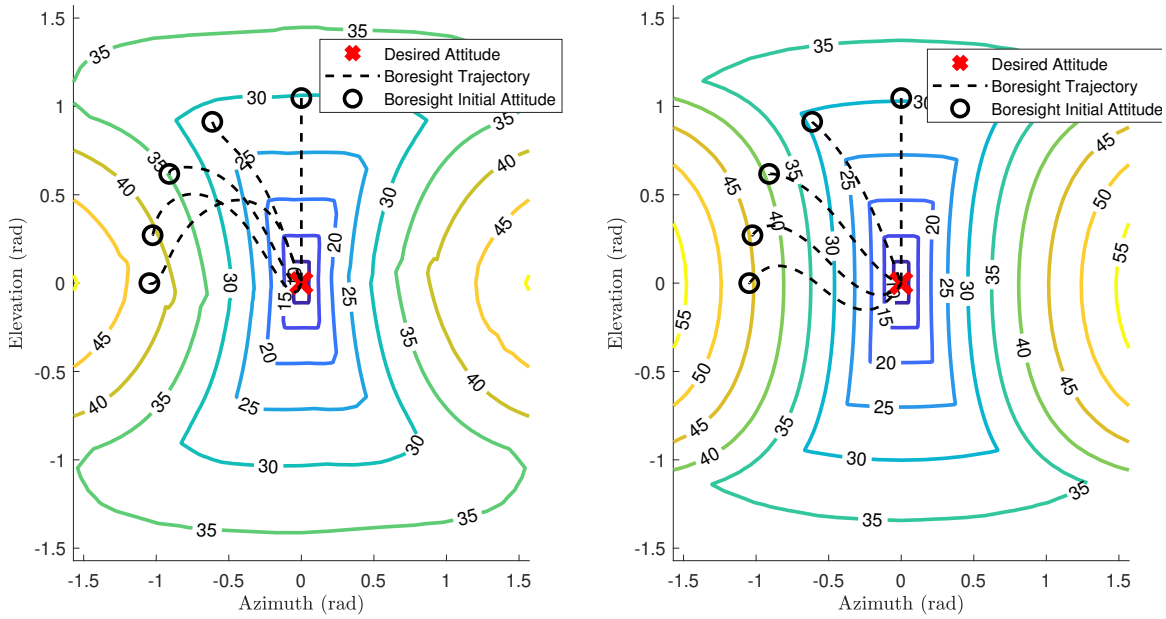

Figure 25. Boresight Trajectories and Time Optimal Contours Starting at 60 Degrees from Final Attitude of Nonlinear (left) and Linearized (right) Dynamics: Asymmetric Body with Cubic Control Constraint

While some trajectories are close to the nonlinear trajectories, not all are close, and in some instances maneuver in the completely opposite direction. As shown in Figure 27, even with a small maneuver of 9 degrees, the linearized version with a cubic control constraint is not valid. Since the goal is to derive an optimal control policy that is valid for all initial conditions within a certain space, using the cubic constraint on the control is ruled out as option.

Figure 23 demonstrates that with a spherical constraint on the control, the linearized solution is similar to the nonlinear solution, even at maneuvers as large as 90

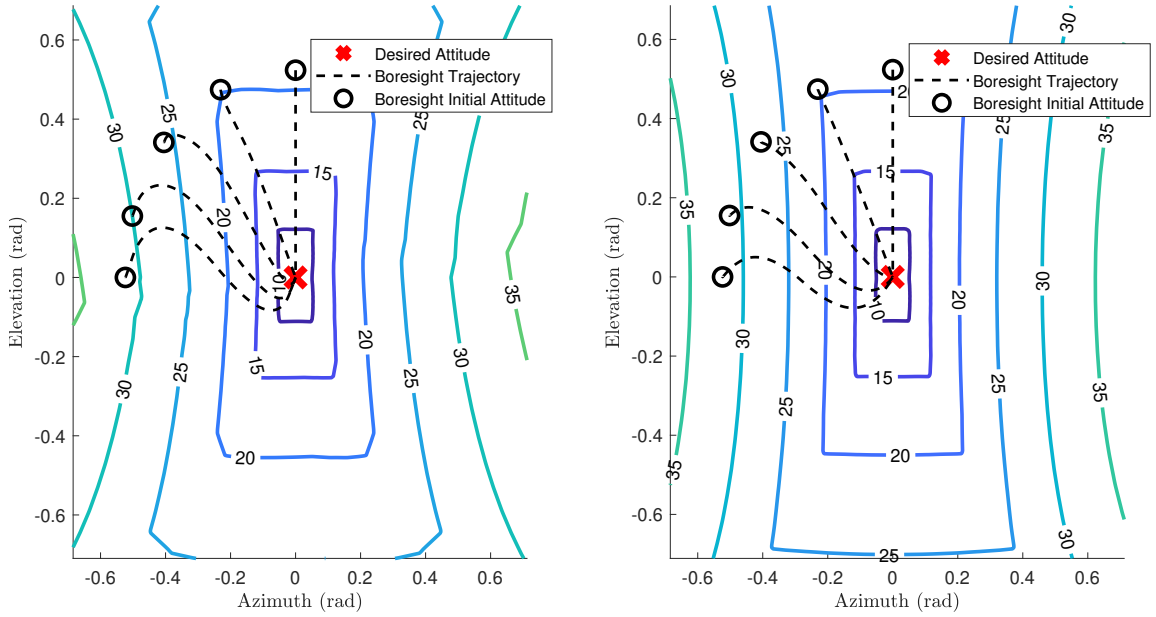

Figure 26. Boresight Trajectories and Time Optimal Contours Starting at 30 Degrees from Final Attitude of Nonlinear (left) and Linearized (right) Dynamics: Asymmetric Body with Cubic Control Constraint

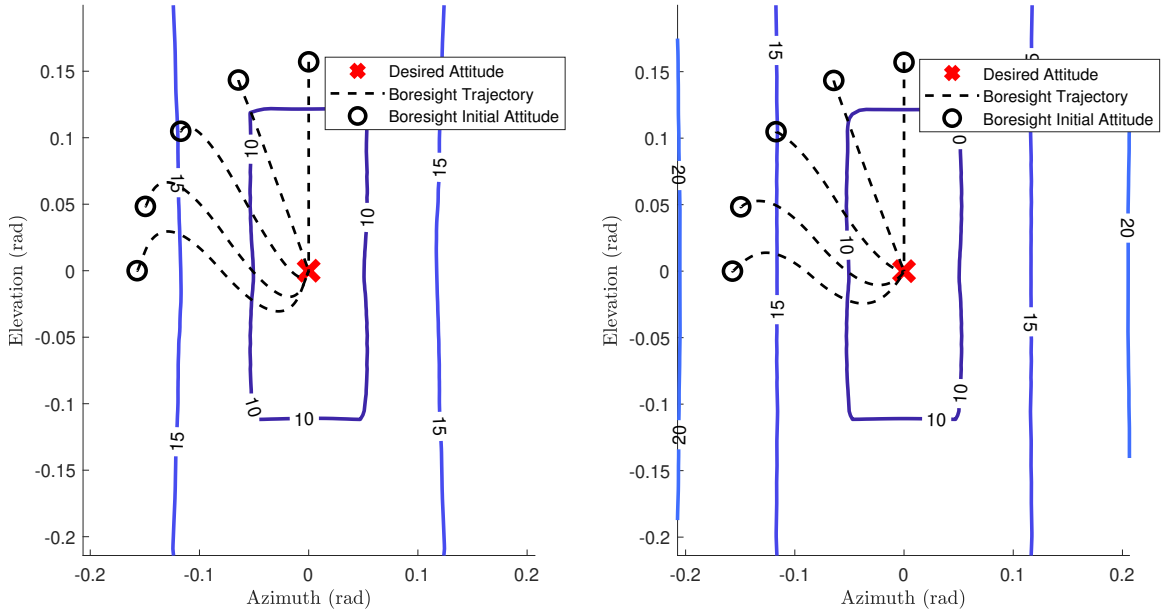

Figure 27. Boresight Trajectories and Time Optimal Contours Starting at 9 Degrees from Final Attitude of Nonlinear (left) and Linearized (right) Dynamics: Asymmetric Body with Cubic Control Constraint

degrees. However, there are some discrepancies at 90 degrees, so the space in which the linearized solution matches the nonlinear solution needs to be investigated. An iterative approach of comparing the trajectories and control history of the nonlinear versus linear solutions for a variety of initial conditions is examined. First, an angle of 30 degrees is compared to ensure that the linearized dynamics provide a valid solution at least out to 30 degrees of rotation.

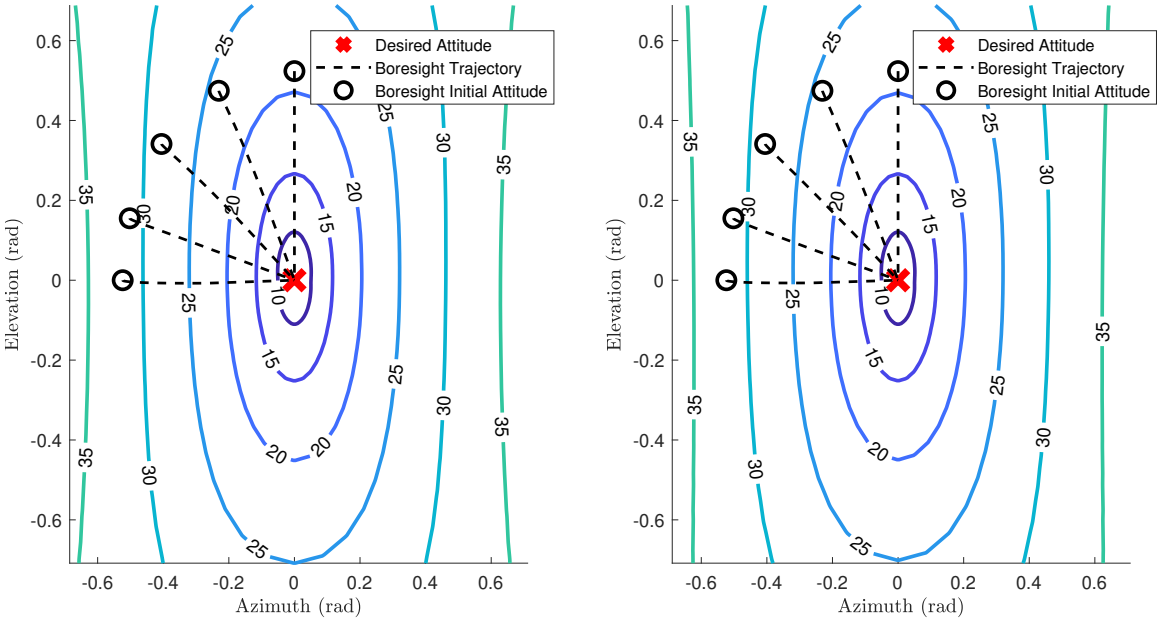

Figure 28. Boresight Trajectories and Time Optimal Contours Starting at 30 Degrees from Final Attitude of Nonlinear (left) and Linearized (right) Dynamics: Asymmetric Body with Spherical Control Constraint

As seen in Figure 28, the boresight trajectory using the linearized dynamics very closely matches the trajectory generated using the nonlinear dynamics. In order to further investigate the validity of the solution, the control history from both sets of trajectories are compared in Figures 29-33.

As seen in Figures 29 and 33, the optimal control history from the linearized solution matches very closely to the control history from the nonlinear solution. However, when not starting at an elevation or azimuth of 0 radians, the control(s) that are not

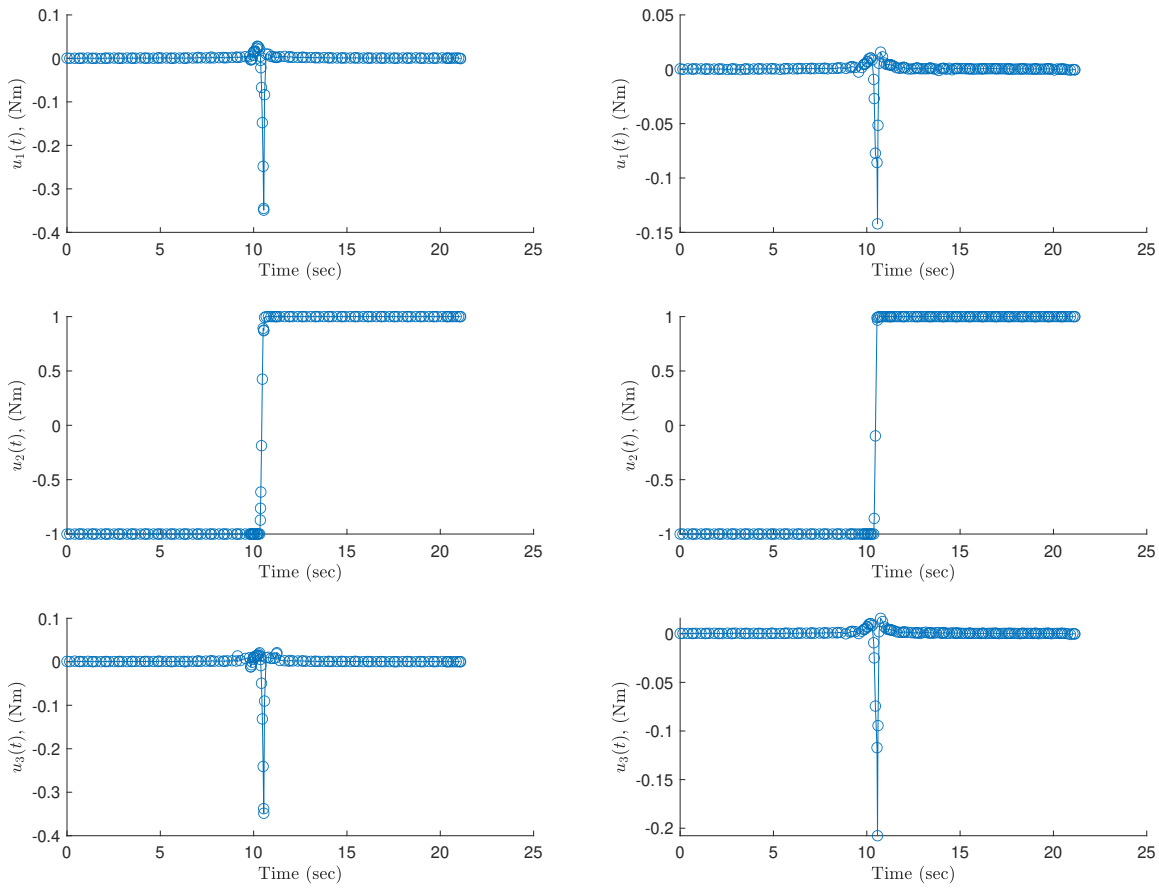

Figure 29. Trajectory 1 Control History of Nonlinear (left) and Linearized (right) Dynamics: 30 Degrees, Asymmetric Body with Spherical Control Constraint

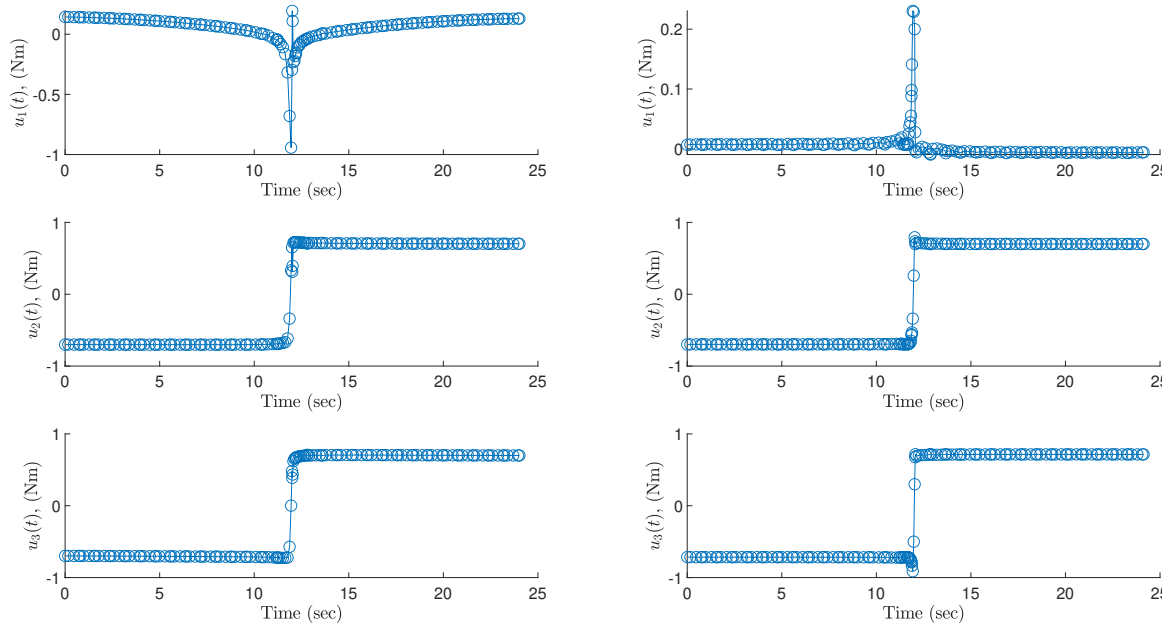

Figure 30. Trajectory 2 Control History of Nonlinear (left) and Linearized (right) Dynamics: 30 Degrees, Asymmetric Body with Spherical Control Constraint

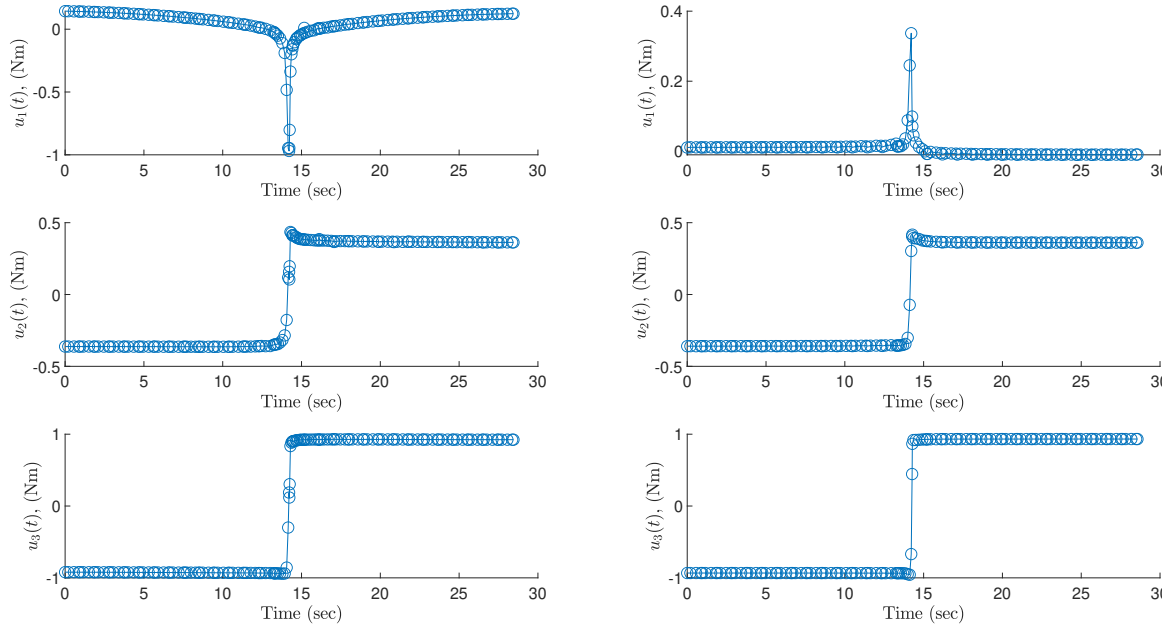

Figure 31. Trajectory 3 Control History of Nonlinear (left) and Linearized (right) Dynamics: 30 Degrees, Asymmetric Body with Spherical Control Constraint

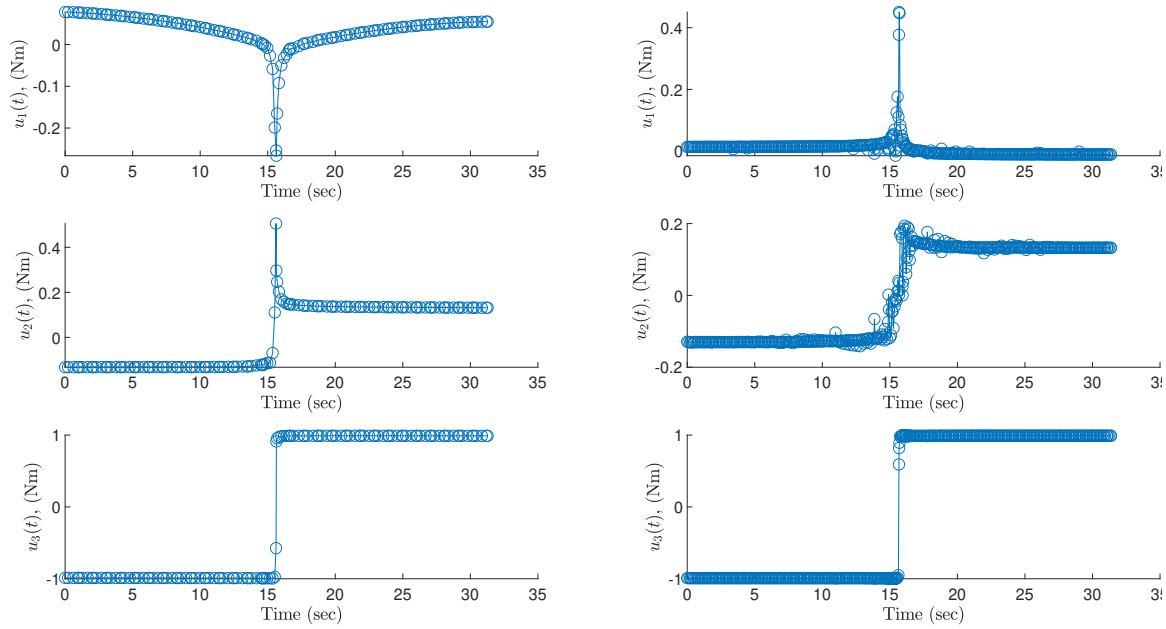

Figure 32. Trajectory 4 Control History of Nonlinear (left) and Linearized (right) Dynamics: 30 Degrees, Asymmetric Body with Spherical Control Constraint

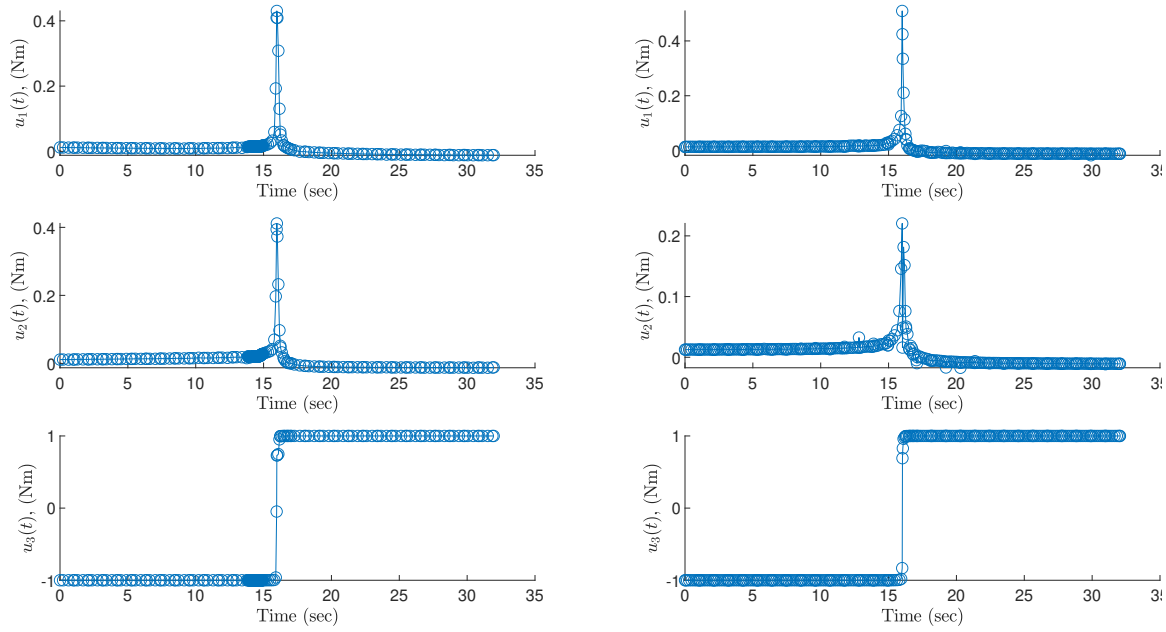

Figure 33. Trajectory 5 Control History of Nonlinear (left) and Linearized (right) Dynamics: 30 Degrees, Asymmetric Body with Spherical Control Constraint

the primary controls utilized in the reorientation, i.e. have a magnitude around 0 Nm for the majority of the reorientation, often have the opposite sign of the jump in control at the switching time. This is demonstrated in Figures 30-32. It is unknown why this occurs, but it will be shown in the development of the optimal control policy that the control history from the optimal control has the same phenomenon. To determine if the control histories are valid, each set of control histories are propagated with the nonlinear dynamics to see how close to the desired end state each control ends up. This comparison is depicted in Figures 34 and 35.

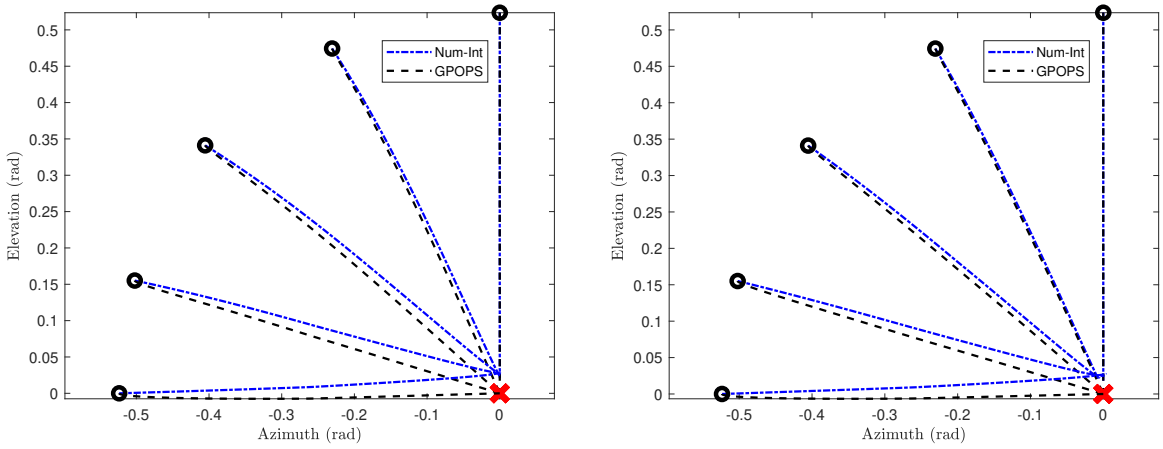

(a) Nonlinear Dynamics **(b) Linearized Dynamics**

Figure 34. Propagated Boresight Trajectories Compared to GPOPS-II Solutions: 30 degree Reorientation, Asymmetric Body with Spherical Constraint

As seen in Figure 35, with the difference in the sign of the control jump at the switching time for the non-primary controls, there is a small deviation in angular velocity, especially in the latter half of the trajectory. However, as seen in Figure 34, this does not translate to a significant difference in the boresight trajectory. It is also useful to look at the difference in predicted optimal times for each of the trajectories. This comparison is given in Table 1.

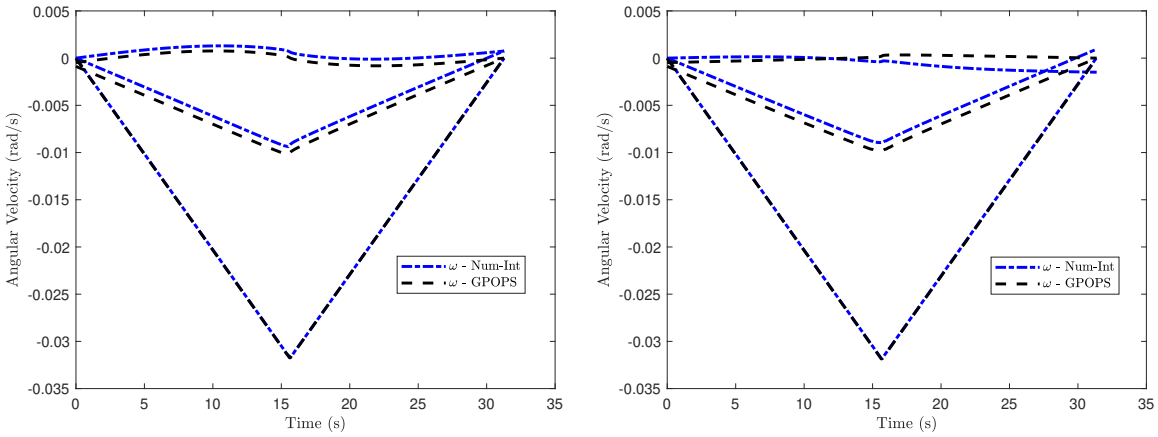

(a) Nonlinear Dynamics **(b) Linearized Dynamics**

Figure 35. Propagated Angular Velocity (rad/s) Compared to GPOPS-II Solutions: Trajectory 4, 30 degree Reorientation, Asymmetric Body with Spherical Constraint

Table 1. Computed Optimal 30 Degree Reorientation Times for Nonlinear vs. Linearized Dynamics

Trajectory	Nonlinear Time (sec)	Linear Time (sec)	% Difference
1	21.09	21.15	0.29
2	24.02	24.13	0.46
3	28.45	28.57	0.42
4	31.28	31.37	0.30
5	31.96	32.05	0.29

The difference in computed optimal reorientation times are very small, so the linearized dynamics appear to be a valid set of dynamics to generate reachable sets to at least 30 degrees of rotation. Since the times computed from the linearized dynamics are always larger than the nonlinear times, these reachable sets computed provide a conservative safe set for reorientations, ensuring the feasibility of an attempted reorientation maneuver to be completed withing the predicted amount of time.

Larger angles of reorientation are now examined to determine the linearized dynamics validity, specifically 60 degrees. Again, the boresight trajectories are examined, and are shown to be relatively similar in Figure 36. The control histories are not shown for brevity, because they are similar to the control histories for the 30 degree reorientations. The same phenomenon of sign reversal occurs at the switching times, but overall, the control from the linearized dynamics closely matches the control from the nonlinear dynamics.

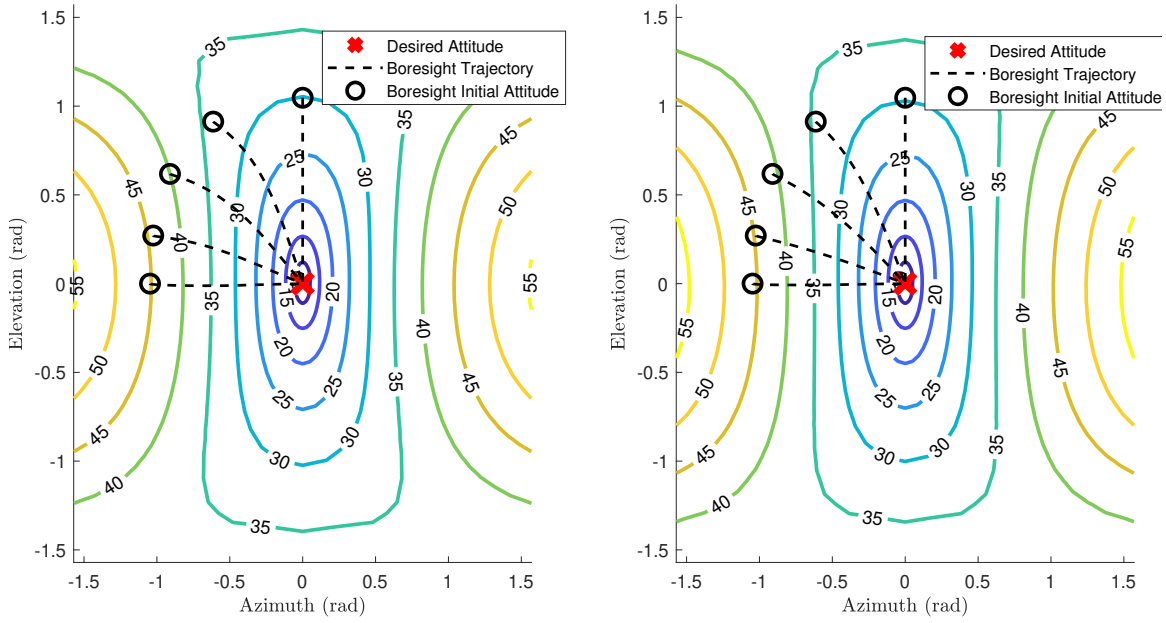

Figure 36. Boresight Trajectories and Time Optimal Contours Starting at 60 Degrees from Final Attitude of Nonlinear (left) and Linearized (right) Dynamics: Asymmetric Body with Spherical Control Constraint

The validity of the solutions is again examined by propagating the nonlinear dynamics with each of the control solutions output by GPOPS-II. Figures 37 and 38 depict these comparisons.

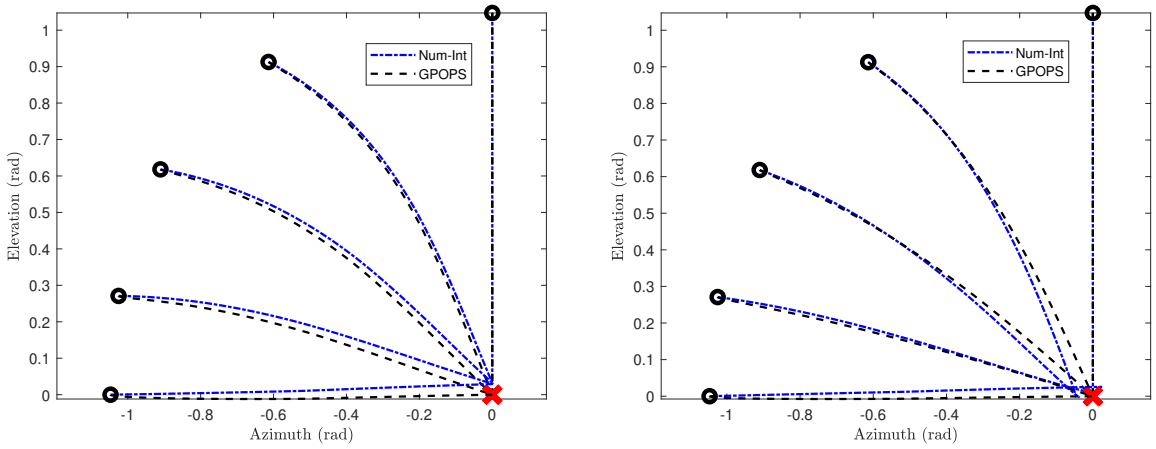

(a) Nonlinear Dynamics **(b) Linearized Dynamics**

Figure 37. Propagated Boresight Trajectories Compared to GPOPS-II Solutions: 60 degree Reorientation, Asymmetric Body with Spherical Constraint

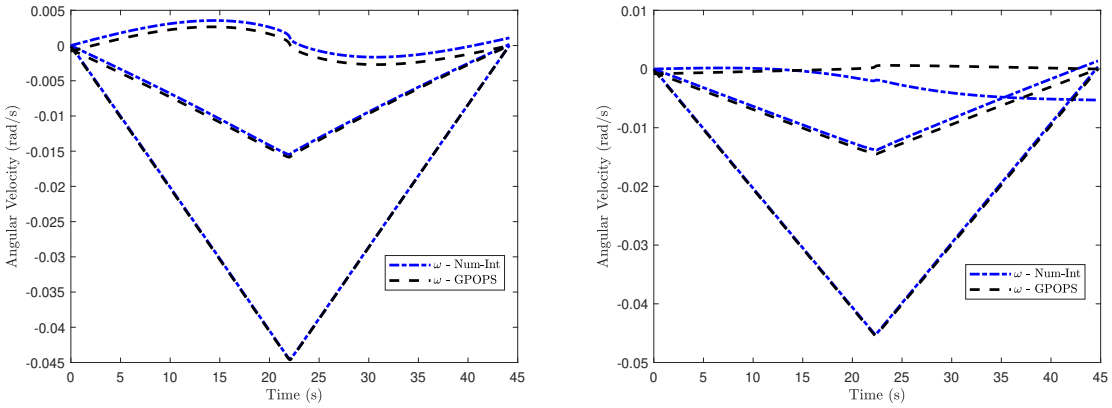

(a) Nonlinear Dynamics **(b) Linearized Dynamics**

Figure 38. Propagated Angular Velocity (rad/s) Compared to GPOPS-II Solutions: Trajectory 4, 60 degree Reorientation, Asymmetric Body with Spherical Constraint

Figures 37 and 38 show markedly greater deviation between the nonlinear and linear solutions than reorientations of only 30 degrees. While the differences are not large in magnitude with less than two degrees for the worst case from the desired

end attitude, and the angular velocity being less than 0.3 deg/sec for the worst case desired rotation rate, it is still important to note that the controls do not get to the desired end state. However, it is again useful to look at the difference in predicted minimum times for each of the trajectories. This comparison is given in Table 2.

Table 2. Computed Optimal 60 Degree Reorientation Times for Nonlinear vs. Linearized Dynamics

Trajectory	Nonlinear Time (sec)	Linear Time (sec)	% Difference
1	29.91	30.26	1.18
2	33.81	34.46	1.90
3	40.01	40.73	1.82
4	44.17	44.73	1.28
5	45.19	45.72	1.17

Table 2 demonstrates that even though the trajectories from GPOPS-II using the linearized dynamics may not exactly achieve the desired end state, the calculated times to achieve a reorientation are close to the nonlinear GPOPS-II solutions, with less than a two percent difference for all trajectories. When the nonlinear GPOPS-II control solution is propagated with the nonlinear dynamics, it is very close to the desired end state. So with the understanding that there is some error in the times being reported for the reachable sets generated from the linearized dynamics, these sets are still useful for observation as they are conservative estimates.

4.2 Computation Times

In order to determine the more efficient attitude parameterization, the computation times of each batch of optimization problems is documented. The results are displayed in Tables 3 and 4. Each batch of runs consists of 1830 starting conditions, all with the same ending condition, resulting in 1830 optimization problems for each batch used to generate the reachable sets. In every case, the MRP batches took less time than the quaternion batches. For a clearer comparison, the results of Table 3 are

used to generate summary statistics in Table 5. It is more computationally efficient to use the MRPs than the quaternion dynamics in generating the sets. This is especially true when using the nonlinear dynamics, because they produce virtually the same results. It is also shown in Table 5 that, overall, the computation times with the linear dynamics takes longer than with the nonlinear dynamics. However, when broken down between the cubic control and spherical control averages, the average computation time per run is 1.19 seconds using the linearized dynamics, compared to 2.25 seconds using the nonlinear dynamics. So if the control is spherical-constrained in the optimization problem, the linearized computation proves faster. But overall, since the nonlinear solutions provide more accurate solutions, it is best to use the nonlinear equations.

Table 3. Computation Times of Optimization Batches for Generating Reachable Sets Using Nonlinear Dynamics

		Time (min)	Time per Run (sec)
Quaternions	**Symmetric**		
	Cubic Control	96.01	3.15
	Spherical Control	71.16	2.33
	Axially Symmetric		
	Cubic Control	158.78	5.21
	Spherical Control	122.17	4.01
	Asymmetric		
	Cubic Control	88.08	2.89
	Spherical Control	85.87	2.82
MRPs	**Symmetric**		
	Cubic Control	39.38	1.29
	Spherical Control	36.62	1.20
	Axially Symmetric		
	Cubic Control	50.37	1.65
	Spherical Control	53.51	1.75
	Asymmetric		
	Cubic Control	40.60	1.33
	Spherical Control	43.28	1.42

Table 4. Computation Times of Optimization Batches for Generating Reachable Sets Using Linearized Dynamics

		Time (min)	Time per Run (sec)
Quaternions	**Symmetric**		
	Cubic Control	107.53	3.53
	Spherical Control	31.02	1.02
	Axially Symmetric		
	Cubic Control	283.90	9.31
	Spherical Control	50.86	1.67
	Asymmetric		
	Cubic Control	142.55	4.67
	Spherical Control	32.08	1.05
MRPs	**Symmetric**		
	Cubic Control	101.43	3.33
	Spherical Control	29.92	0.98
	Axially Symmetric		
	Cubic Control	209.27	6.86
	Spherical Control	43.75	1.43
	Asymmetric		
	Cubic Control	103.67	3.40
	Spherical Control	29.71	0.97

Table 5. Summary Statistics of Computation Times

	MRPs	Quaternions	Nonlinear Dynamics	Linearized Dynamics	Cubic Control	Spherical Control
Average Time Per Run (sec)	2.14	3.47	2.42	3.18	3.88	1.72

4.3 Optimal Control Policy

Section 4.1.4 demonstrated that with a spherical constraint on the control, the reachable sets generated from linearized dynamics closely match the sets generated from the nonlinear dynamics. This finding presents an opportunity for an optimal control policy to be derived from the linearized dynamics for all symmetries of spacecraft. To the author's knowledge, an optimal control policy derived from the linearized dynamics that is applicable to all symmetries of spacecraft does not exist [42].

4.3.1 Control Policy Derivation

In order to determine an optimal control policy for each set of dynamics, the necessary conditions of optimality listed in Equations 18-20 must be satisfied. Unlike previous attempts to develop an optimal control policy for the nonlinear MRP dynamics, the linearized optimal control policy can be applied to a spacecraft with any type of symmetry. The Hamiltonian with the MRP dynamics is given in Equation 48,

$$\begin{aligned}\mathcal{H} &= 1 + \lambda_{\omega_1}(\dot{\omega}_1) + \lambda_{\omega_2}(\dot{\omega}_2) + \lambda_{\omega_3}(\dot{\omega}_3) + \lambda_{\sigma_1}\dot{\sigma}_1 + \lambda_{\sigma_2}\dot{\sigma}_2 + \lambda_{\sigma_3}\dot{\sigma}_3 \\ &= 1 + {\lambda_\omega}^{\mathrm{T}}\,\dot{\omega} + {\lambda_\sigma}^{\mathrm{T}}\,\dot{\sigma}\end{aligned} \tag{48}$$

For the linearized dynamics, the Hamiltonian becomes,

$$\begin{aligned}\mathcal{H} = 1 + \lambda_{\omega_1}\left(\frac{1}{J_{xx}}\right)u_1 + \lambda_{\omega_2}\left(\frac{1}{J_{yy}}\right)u_2 + \lambda_{\omega_3}\left(\frac{1}{J_{zz}}\right)u_3 \\ + \lambda_{\sigma_1}\left(\frac{1}{4}\right)\omega_1 + \lambda_{\sigma_2}\left(\frac{1}{4}\right)\omega_2 + \lambda_{\sigma_3}\left(\frac{1}{4}\right)\omega_3\end{aligned} \tag{49}$$

It is apparent that while applying the necessary condition given in Equation 20, also known as the stationarity condition, to the Hamiltonian listed in Equation 49, the controls u_1, u_2, and u_3 vanish. It will be shown that specifying the control in a manner such that u_1, u_2, and u_3 do not vanish when applying the stationarity condition is helpful for developing an optimal control law. Applying the necessary condition in Equation 19 provides the following differential equations for the costates,

$$\dot{\lambda}_{\omega_1}(t) = -\frac{\partial \mathcal{H}}{\partial \omega_1} = -\frac{1}{4}\lambda_{\sigma_1} \tag{50}$$

$$\dot{\lambda}_{\omega_2}(t) = -\frac{\partial \mathcal{H}}{\partial \omega_2} = -\frac{1}{4}\lambda_{\sigma_2} \tag{51}$$

$$\dot{\lambda}_{\omega_3}(t) = -\frac{\partial \mathcal{H}}{\partial \omega_3} = -\frac{1}{4}\lambda_{\sigma_3} \tag{52}$$

$$\dot{\lambda}_{\sigma_1}(t) = -\frac{\partial \mathcal{H}}{\partial \sigma_1} = 0 \tag{53}$$

$$\dot{\lambda}_{\sigma_2}(t) = -\frac{\partial \mathcal{H}}{\partial \sigma_2} = 0 \tag{54}$$

$$\dot{\lambda}_{\sigma_3}(t) = -\frac{\partial \mathcal{H}}{\partial \sigma_3} = 0 \tag{55}$$

which leads to $\lambda_{\sigma_1}, \lambda_{\sigma_2}$, and λ_{σ_3} being constant, denoted in this derivation as c_1, c_2, and c_3 respectively. Since Equations 50, 51, and 52 are dependent on $\lambda_{\sigma_1}, \lambda_{\sigma_2}$, and λ_{σ_3} which are constant, the derivatives of $\lambda_{\omega_1}, \lambda_{\omega_2}$, and λ_{ω_3} are constant. In summary,

$$\lambda_{\sigma_1} = c_1,\ \lambda_{\sigma_2} = c_2,\ \lambda_{\sigma_3} = c_3 \tag{56}$$

$$\dot{\lambda}_{\omega_1} = -\frac{1}{4}c_1,\ \dot{\lambda}_{\omega_2} = -\frac{1}{4}c_2,\ \dot{\lambda}_{\omega_3} = -\frac{1}{4}c_3 \tag{57}$$

Since the control is bounded, Pontryagin's Minimum (or Maximum) Principle (PMP) must be invoked to satisfy the necessary conditions of optimal control. PMP states that the optimal control must minimize the Hamiltonian [20]. Minimizing the Hamiltonian in Equation 49, the optimal control has the form

$$u_i = -sign(\lambda_{\omega_i}) \tag{58}$$

or in the expanded form,

$$u_i > 0, \quad \text{if } \lambda_{\omega_i} < 0 \tag{59}$$

$$u_i < 0, \quad \text{if } \lambda_{\omega_i} > 0 \tag{60}$$

$$u_i = u_{switch}, \quad \text{if } \lambda_{\omega_i} = 0 \tag{61}$$

With a cubic constraint on the control, where all of the controls are individually bounded between u_{min} and u_{max}, the optimal control becomes:

$$u_i = u_{max}, \quad \text{if } \lambda_{\omega_i} < 0 \tag{62}$$

$$u_i = u_{min}, \quad \text{if } \lambda_{\omega_i} > 0 \tag{63}$$

$$u_i = u_{switch}, \quad \text{if } \lambda_{\omega_i} = 0 \tag{64}$$

As was shown in Section 4.1.4, having a cubic constraint on the control for the linearized dynamics is not valid for predicting the nonlinear dynamics. However, when a spherical constraint is imposed on the control, the linearized MRP dynamics do a much better job of accurately predicting the nonlinear MRP dynamics.

When a spherical constraint on the control, the magnitude of the control is constrained, but the control direction is not. A body-fixed coordinate system can therefore be defined such that the body x axis becomes aligned with the inertial $\hat{I}_x$ axis at

the final time of the maneuver, t_f. As shown in Figure 39, two angles, α and β are used to define the control direction relative to the specified reference frame, and L is used to define the control magnitude.

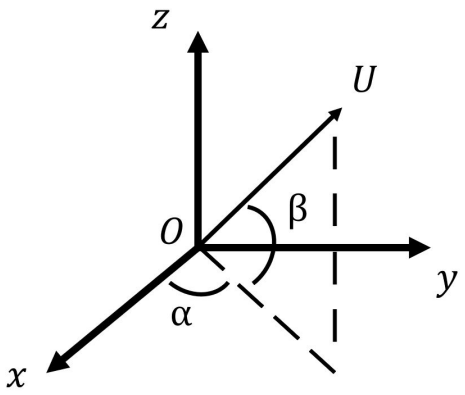

Figure 39. Definition of Control Direction

With this new definition of the control direction, the three control components in the new frame are:

$$\boldsymbol{U}(t) = \begin{bmatrix} L(t)\sin\alpha(t) \\ L(t)\cos\alpha(t)\cos\beta(t) \\ L(t)\cos\alpha(t)\sin\beta(t) \end{bmatrix} \tag{65}$$

where $0 \leq L(t) \leq u_{max}$, $-(\pi/2) \leq \alpha(t) \leq (\pi/2)$, and $0 \leq \beta(t) \leq 2\pi$ as defined in [42]. This results in the new Hamiltonian becoming:

$$\begin{aligned} \mathcal{H} = 1 &+ \lambda_{\omega_1}\left(\frac{1}{J_{xx}}\right) L\sin\alpha + \lambda_{\omega_2}\left(\frac{1}{J_{yy}}\right) L\cos\alpha\cos\beta + \lambda_{\omega_3}\left(\frac{1}{J_{zz}}\right) L\cos\alpha\sin\beta \\ &+ \lambda_{\sigma_1}\left(\frac{1}{4}\right)\omega_1 + \lambda_{\sigma_2}\left(\frac{1}{4}\right)\omega_2 + \lambda_{\sigma_3}\left(\frac{1}{4}\right)\omega_3 \end{aligned} \tag{66}$$

In order to solve for the optimal control angles α and β, the necessary optimal conditions are applied to Equation 66. Applying the stationarity condition yields the

following three equations:

$$\frac{\partial \mathcal{H}}{\partial L} = \lambda_{\omega_1}\left(\frac{1}{J_{xx}}\right)\sin\alpha + \lambda_{\omega_2}\left(\frac{1}{J_{yy}}\right)\cos\alpha\cos\beta + \lambda_{\omega_3}\left(\frac{1}{J_{zz}}\right)\cos\alpha\sin\beta = 0 \quad (67)$$

$$\frac{\partial \mathcal{H}}{\partial \alpha} = \lambda_{\omega_1}\left(\frac{1}{J_{xx}}\right)L\cos\alpha - \lambda_{\omega_2}\left(\frac{1}{J_{yy}}\right)L\sin\alpha\cos\beta - \lambda_{\omega_3}\left(\frac{1}{J_{zz}}\right)L\sin\alpha\sin\beta = 0 \quad (68)$$

$$\frac{\partial \mathcal{H}}{\partial \beta} = -\lambda_{\omega_2}\left(\frac{1}{J_{yy}}\right)L\cos\alpha\sin\beta + \lambda_{\omega_3}\left(\frac{1}{J_{zz}}\right)L\cos\alpha\cos\beta = 0 \quad (69)$$

Equation 69 can be solved by dividing out L and the $\cos\alpha$ terms, and solving for β in terms of the costates, to give the optimal control angle for β, yielding:

$$\beta^* = \tan^{-1}\left(\frac{-J_{yy}\lambda_{\omega_3}}{-J_{zz}\lambda_{\omega_2}}\right) \quad (70)$$

This expression for β is then substituted into Equation 68 to solve for α, as seen below.

$$\begin{aligned}\frac{\partial \mathcal{H}}{\partial \alpha} =& \lambda_{\omega_1}\left(\frac{1}{J_{xx}}\right)L\cos\alpha - \lambda_{\omega_2}\left(\frac{1}{J_{yy}}\right)L\sin\alpha\cos\beta^* \\ &- \lambda_{\omega_3}\left(\frac{1}{J_{zz}}\right)L\sin\alpha\sin\beta^* = 0\end{aligned} \quad (71)$$

Given that,

$$\cos(\beta^*) = \frac{-J_{zz}\lambda_{\omega_2}}{\sqrt{J_{zz}^2\lambda_{\omega_2}^2 + J_{yy}^2\lambda_{\omega_3}^2}} \quad (72)$$

$$\sin(\beta^*) = \frac{-J_{yy}\lambda_{\omega_3}}{\sqrt{J_{zz}^2\lambda_{\omega_2}^2 + J_{yy}^2\lambda_{\omega_3}^2}} \quad (73)$$

this yields,

$$\tan\alpha = \frac{-\lambda_{\omega_1}J_{yy}J_{zz}}{J_{xx}\sqrt{J_{zz}^2\lambda_{\omega_2}^2 + J_{yy}^2\lambda_{\omega_3}^2}} \quad (74)$$

which gives the optimal control angle for α:

$$\alpha^* = \tan^{-1}\left(\frac{-\lambda_{\omega_1} J_{yy} J_{zz}}{J_{xx}\sqrt{J_{zz}^2\lambda_{\omega_2}^2 + J_{yy}^2\lambda_{\omega_3}^2}}\right) \tag{75}$$

When the control is written in terms of the three optimal torques u_1^*, u_2^*, and u_3^*, this yields:

$$\boldsymbol{U}^*(t) = \begin{bmatrix} u_1^* \\ u_2^* \\ u_3^* \end{bmatrix} = \begin{bmatrix} L(t)\sin\alpha^* \\ L(t)\cos\alpha^*\cos\beta^* \\ L(t)\cos\alpha^*\sin\beta^* \end{bmatrix} \tag{76}$$

Where, in order to satisfy Pontryagin's Minimum Principle of minimizing the Hamiltonian,

$$L(t) = 0, \quad \text{if } \lambda_{\omega_1}\left(\frac{1}{J_{xx}}\right)\sin\alpha + \lambda_{\omega_2}\left(\frac{1}{J_{yy}}\right)\cos\alpha\cos\beta + \lambda_{\omega_3}\left(\frac{1}{J_{zz}}\right)\cos\alpha\sin\beta > 0 \tag{77}$$

$$L(t) = u_{max}, \quad \text{if } \lambda_{\omega_1}\left(\frac{1}{J_{xx}}\right)\sin\alpha + \lambda_{\omega_2}\left(\frac{1}{J_{yy}}\right)\cos\alpha\cos\beta + \lambda_{\omega_3}\left(\frac{1}{J_{zz}}\right)\cos\alpha\sin\beta \leq 0 \tag{78}$$

4.4 Control Policy Testing

To determine if the optimal control policy derived from the linearized dynamics provides a valid solution to the nonlinear dynamics, this control policy is used to propagate the spacecraft trajectories. Since the costates are an essential part of the control law, the initial costates are needed. An analytical method to determine the initial costates is not attained in this research, so these values are taken from the GPOPS-II solutions' accurate approximations of the costates, which it solves using the costate mapping theorem [21]. It is important to note that these initial costates are taken from the solutions that use the linearized MRP dynamics. The costate solutions are then propagated according to Equations 50-55. This is used in

conjunction with the expressions β^* and α^* given in Equations 70 and 75 to solve for the optimal controls given in Equation 76. These optimal controls are then applied to the initial attitudes of the trajectories, and then propagated with the nonlinear dynamics to determine how close the solution came to the desired end state. Figures 40-42 demonstrate the accuracy of the optimal control policy at 30, 60 and 90 degrees.

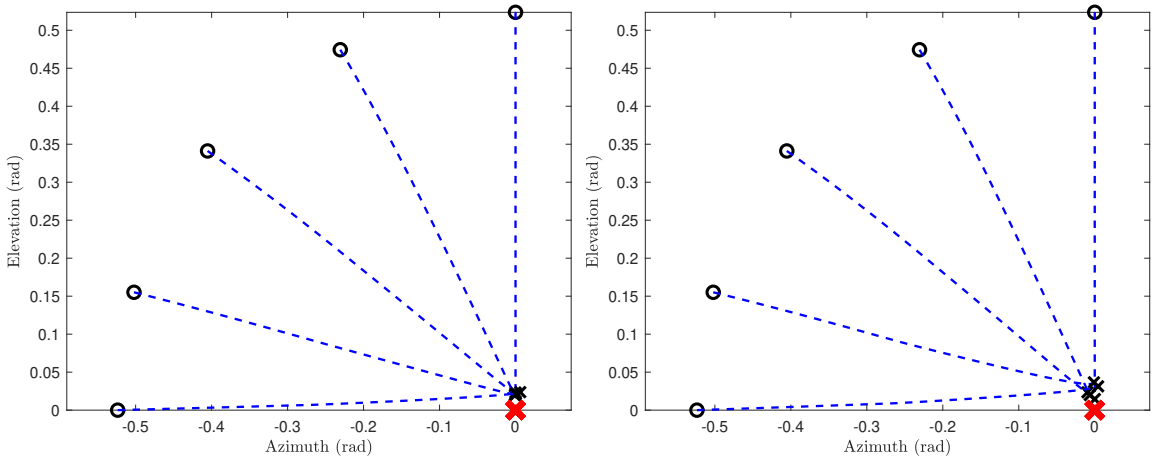

(a) Spherical Body **(b) Asymmetric Body**

Figure 40. Propagated Angular Velocity (rad/s) Compared to GPOPS-II Solutions: Trajectory 4, 30 degree Reorientation, Asymmetric Body with Spherical Constraint

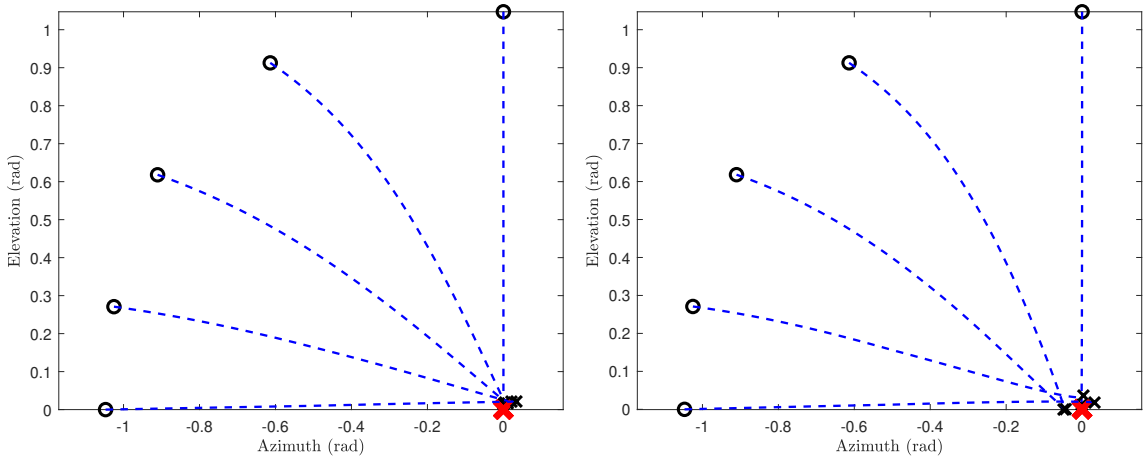

(a) Spherical Body **(b) Asymmetric Body**

Figure 41. Propagated Angular Velocity (rad/s) Compared to GPOPS-II Solutions: Trajectory 4, 30 degree Reorientation, Asymmetric Body with Spherical Constraint

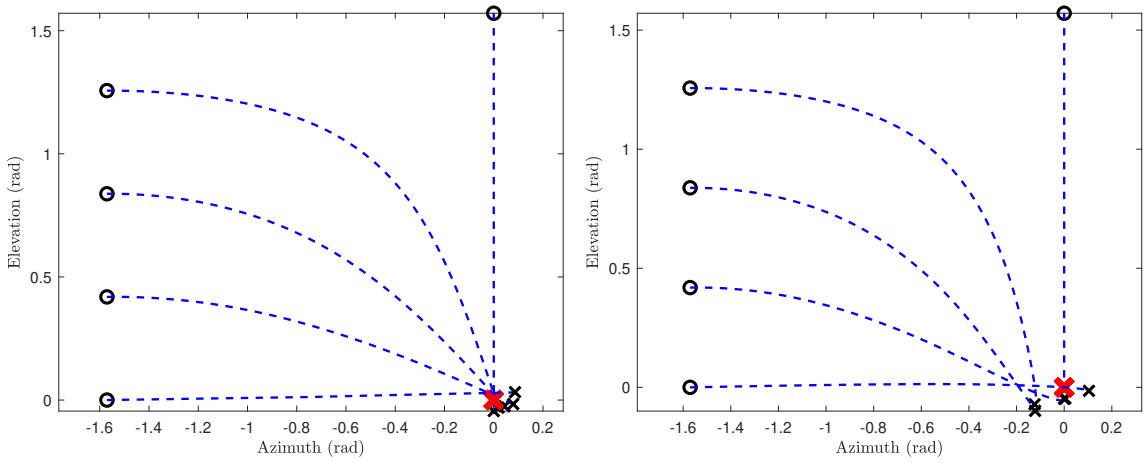

(a) Spherical Body **(b) Asymmetric Body**

Figure 42. Propagated Angular Velocity (rad/s) Compared to GPOPS-II Solutions: Trajectory 4, 90 degree Reorientation, Asymmetric Body with Spherical Constraint

These demonstrate that even when starting from 90 degrees of rotation from the desired end state, the optimal control policy gets close to the desired end attitude, with a maximum error of 5.28 degrees for a spherically symmetric body, and a maximum error of 9 degrees for an asymmetric body. A summary of these errors is given in Table 6.

Table 6. Maximum Pointing Errors

	90 deg	**60 deg**	**30 deg**
Spherically Symmetric	5.28	2.31	1.40
Asymmetric	9.00	2.80	2.10

The smaller the rotation, the more this error decreases, pointing to the usefulness of this optimal control policy for medium angle attitude maneuvers. It is important to note that all of these maneuvers are completed without any sort of feedback, which is essential for realistic spacecraft reorientations. By providing feedback of the true attitude, this control policy can still be a valid candidate for spacecraft attitude maneuvers.

4.4.1 Summary

This chapter presented the reachable sets generated from the solutions of time-optimal control problems correlated with the starting attitudes of the spacecraft. An analysis of these sets provided insights into the usefulness of the linearized dynamics in providing a conservative but accurate estimate of the spacecraft's reachable space. The computational efficiency of generating these sets was then presented, demonstrating that the most efficient way to generate the sets of a given spacecraft symmetry with the method detailed herein, was with the linearized MRP dynamics and a spherical control constraint. Lastly, the development and accuracy of an optimal control policy based off of the linearized MRP dynamics was presented and tested via simulation.

V. Conclusions and Recommendations

This chapter closes the thesis by summarizing the research that was accomplished and contributions to the field of astronautics. Ideas for future research are discussed as a potential extension to the work presented in this thesis.

5.1 Conclusions

A formal production and analysis of the reachable sets for attitude reorientations of a rigid body spacecraft was presented. Although reachability has been applied to the realm of astrodynamics previously, a research gap was identified in the application to spacecraft attitude reorientations. Advancements in optimization software made it possible to solve thousands of optimization problems for the nonlinear rotational dynamics as well as the linearized versions of those dynamics.

The first research question addressed was, given a desired end state and bounded control input, what are the possible initial conditions (reachable sets) for successfully completing a reorientation maneuver in a given amount of time? A background of the dynamics used was presented, as well as different parameterizations of the attitude. Both quaternions and Modified Rodrigues Parameters (MRPs) were used to describe the attitude of the spacecraft, and the kinematics for each were presented. In order to compute these reachable sets, a grid of 1830 initial conditions was formed as the basis for reorientations of less than 90 degrees. Each initial condition was used as the initial boundary of solving a time-optimal reorientation problem. These optimal solutions were then computed using GPOPS-II to provide an optimal time to complete the reorientation. In order to provide the best visual representation of attitude, the 3-dimensional MRP and quaternion spaces were converted to a 2-dimensional azimuth and elevation space. The optimal times were then matched with their correspond-

ing initial condition, and used to create time-optimal contours which represented the reachable sets. These sets were created for each type of dynamics, spacecraft symmetry, and control constraint. By creating a visualization of the reachable sets, it was easy to compare the optimal times to maneuver given a certain combination of initial conditions. A single reachable set could be used by an operator for a spacecraft with matching conditions to determine the amount of time it would take to complete a given maneuver, and inform their decision of whether or not to complete the maneuver. This information could also be stored on-board a spacecraft, to inform the spacecraft of the feasibility of a certain maneuver within a certain amount of time.

Computing the time-optimal reorientations with GPOPS-II was also, on average, faster than computing the solution with the quaternion dynamics. So for attitude changes of less than 360 degrees, MRPs are better in terms of computational time. Using the linear MRP dynamics resulted in even faster computation time, and provided a slightly more conservative estimate than the nonlinear dynamics, while still providing an accurate representation of the reachable sets. This results in a higher tolerance for the verification of safety of a maneuver along with faster computation of a reachable set. For potential future implementation of on-board processing, the MRP representation and corresponding dynamics would be a good option as long as the spacecraft was computing reorientations of less than 360 degrees.

The second research question addressed, was, how do the linearized equations of rotational motion match the nonlinear dynamics? Each reachable set depicted the optimal time to complete a maneuver given a bounded control input. By looking at the comparison of reachable sets computed with the linearized vs nonlinear MRP dynamics, it was shown that the time-optimal solutions were very similar up to approximately 60 degrees. The boresight trajectories were then examined and it was shown that, with a spherically-bounded control, the linearized solution was very sim-

ilar to the nonlinear solution. This started an investigation into a potential optimal control solution derived from the linearized MRP dynamics.

The final research question tackled, was, assuming the end state is reachable, what is the optimal control required to achieve the desired end state? An optimal control solution based off of the linearized MRP dynamics was presented that was applicable for all spacecraft symmetries. For the attitude reorientation space considered (out to 90 degrees of rotation), the optimal control policy achieved attitudes close to the desired attitude without any feedback. With the implementation of feedback, this control policy would be accurate and easy to compute, which is conducive for on-board operations.

5.2 Recommendations

There are several future expansions of the work presented herein. As discussed previously, there are an infinite amount of ways to express the attitude of a spacecraft. MRPs and quaternions are two of the most widely used, but there may be other, more efficient ways of computing reachable sets with a different parameterization. The magnitude of the angle of reorientations was limited to 90 degrees, due to the fact that the linearized dynamics were used throughout, so a generation of the reachable sets of angles greater than 90 degrees would be helpful. It may also be useful to explore reachable sets of axisymmetric bodies that incorporate symmetries about different primary axes (i.e. $J_{xx} = J_{yy}$ or $J_{yy} = J_{zz}$ instead of $J_{xx} = J_{zz}$ which was used in this research).

The computation time of these reachable sets was not trivial. Since the computation of the reachable sets requires several minutes, with a software that consumes a lot of space and computing power, it does not currently make sense to do the reachable set computations on board with this method. Finding ways to reduce this compu-

tation time would be beneficial for on-board applications. This could be potentially done with approximating the reachable sets geometrically as has been done in other research for other applications. The biggest issue is representing a 3-dimensional space used for attitude in a way that is useful visually, so mapping these geometric approximations to a 2-dimensional plane proved helpful.

Also, the development of the linearized optimal control policy requires the knowledge of the initial costates. Since these values were taken from the output of GPOPS-II, it would be useful to find a method of calculating the initial costates analytically. The knowledge of the reachable sets presented herein may be useful in developing this analytic solution.

Finally, being able to expand this research for spacecraft which are not a simple rigid body would be beneficial. This research is applicable for very simple spacecraft, however, many spacecraft include flexible components, containers with fuel-slosh, or moving components which call for a deviation from the standard rigid-body dynamics. These dynamics are more complex, and therefore would require a greater amount of time to compute the reachable sets, but would be more applicable for more complicated spacecraft designs. It is also often necessary to incorporate constraints into reorientations, for example, avoiding sensitive sensor damage by pointing at the sun or other bright objects [43]. Incorporating constraints into these reorientations would slow down the computation times of reachable sets, but could be used to paint a more accurate picture for spacecraft needing to avoid certain attitudes.

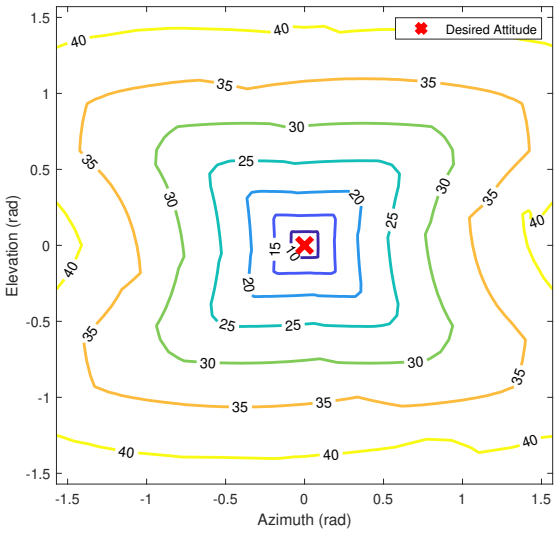

(a) Nonlinear MRP Dynamics

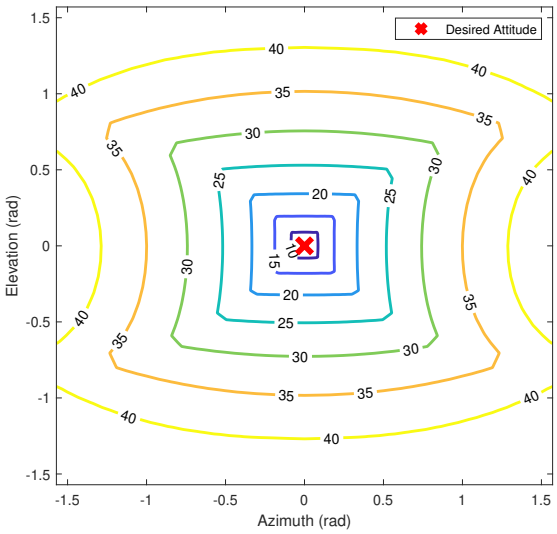

(b) Linearized MRP Dynamics

Figure 43. Reachable Set: Spherically Symmetric Body, Cubic Control Constraint

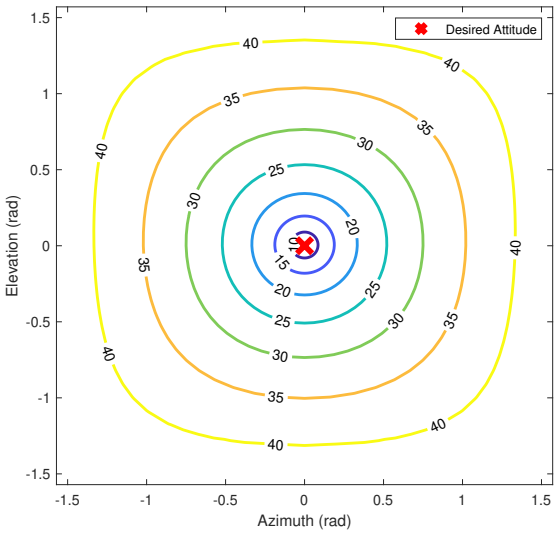

(a) Nonlinear MRP Dynamics

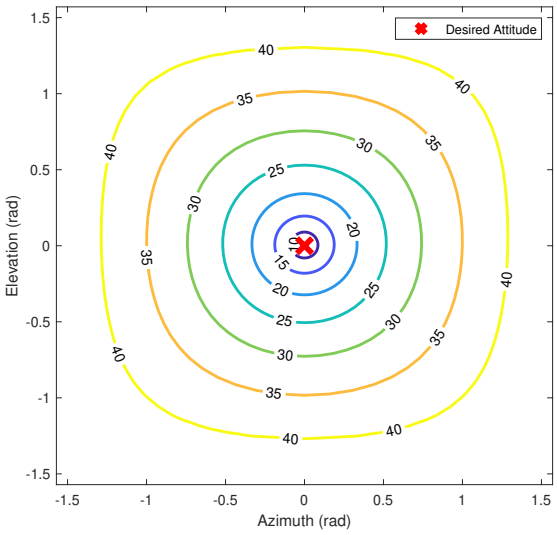

(b) Linearized MRP Dynamics

Figure 44. Reachable Set Depicted as Time Optimal Contours: Spherically Symmetric Body, Spherical Control Constraint

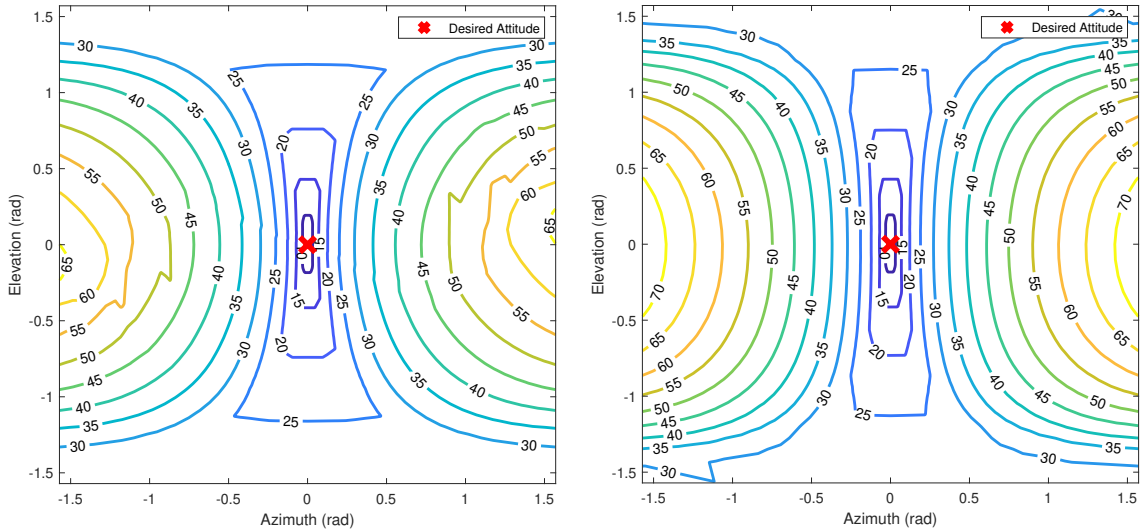

(a) Nonlinear MRP Dynamics

(b) Linearized MRP Dynamics

Figure 45. Reachable Set Depicted as Time Optimal Contours: Axisymmetric Body, Cubic Control Constraint

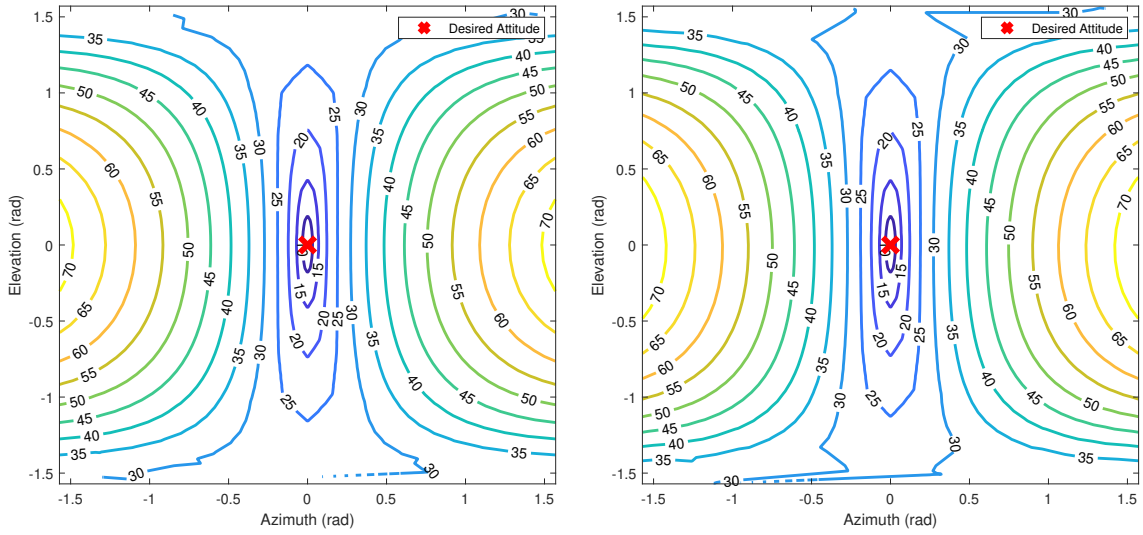

(a) Nonlinear MRP MRP Dynamics

(b) Linearized MRP Dynamics

Figure 46. Reachable Set Depicted as Time Optimal Contours: Axisymmetric Body, Spherical Control Constraint

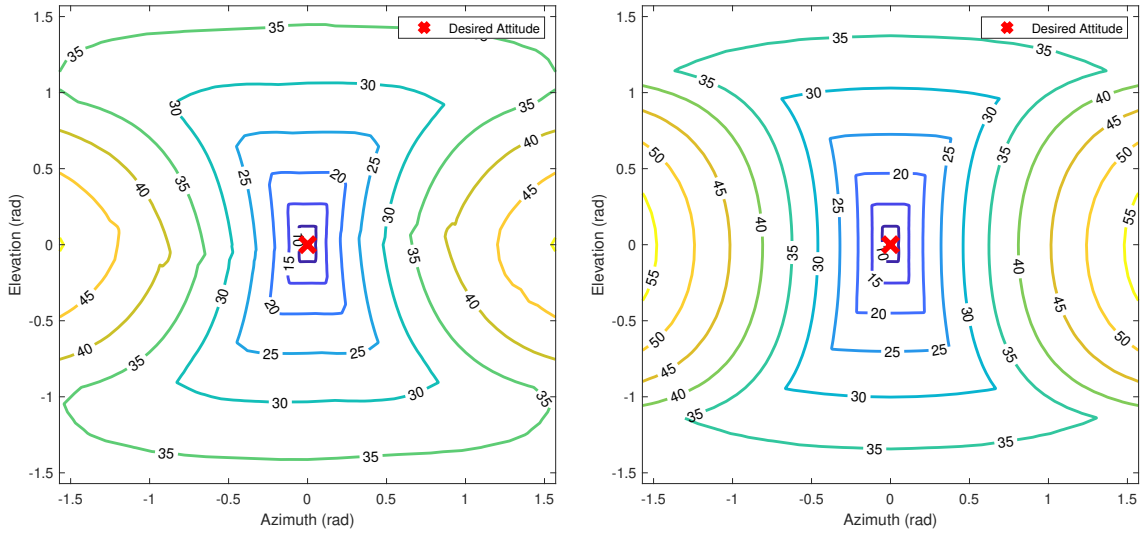

(a) Nonlinear MRP Dynamics (b) Linearized MRP Dynamics

Figure 47. Reachable Set Depicted as Time Optimal Contours: Asymmetric Body, Cubic Control Constraint

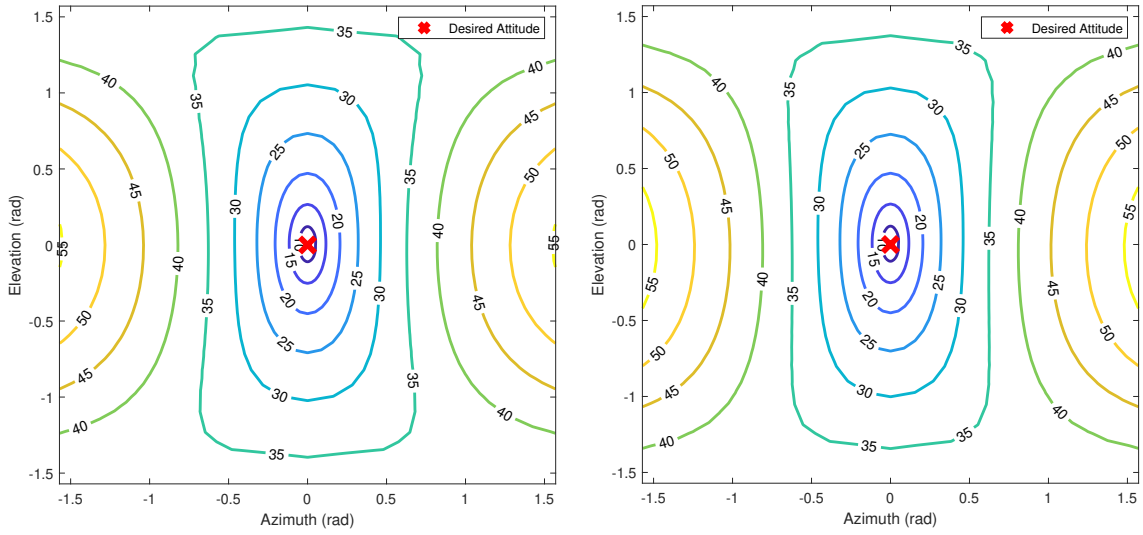

(a) Nonlinear MRP Dynamics (b) Linearized MRP Dynamics

Figure 48. Reachable Set Depicted as Time Optimal Contours: Asymmetric Body, Spherical Control Constraint

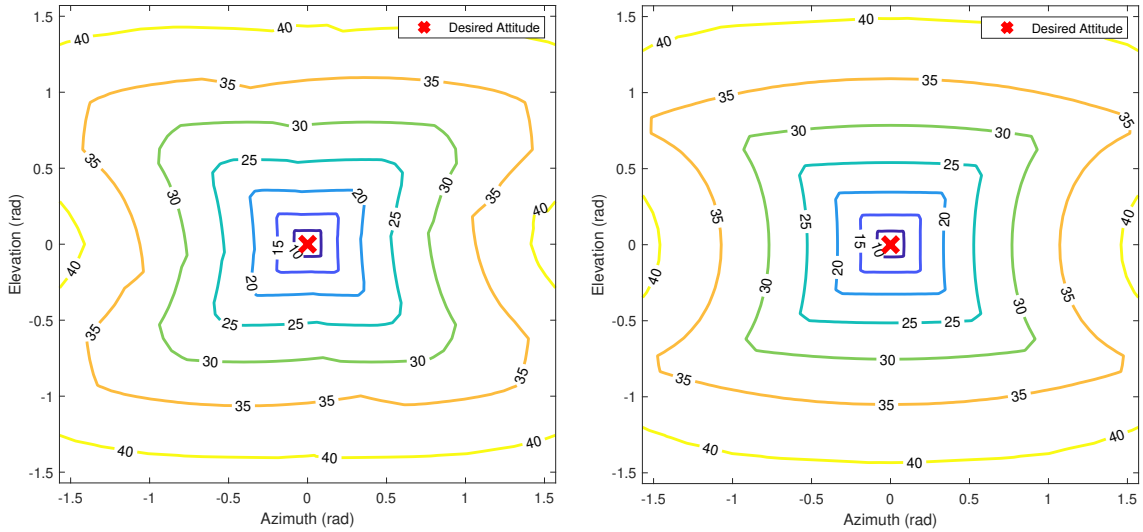

(a) Nonlinear Quaternion Dynamics **(b) Linearized Quaternion Dynamics**

Figure 49. Reachable Set Depicted as Time Optimal Contours: Spherically Symmetric Body, Cubic Control Constraint

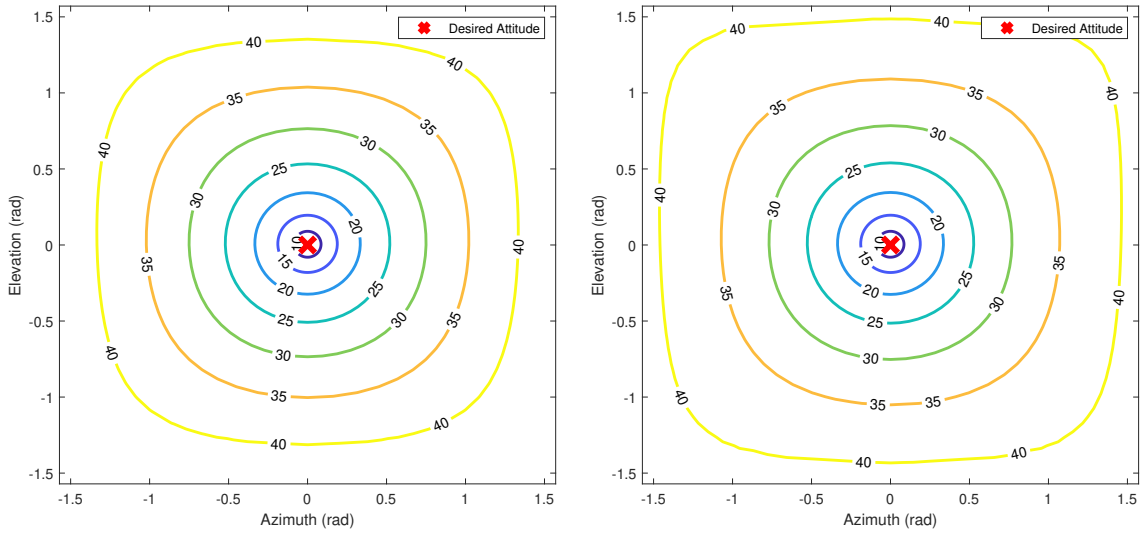

(a) Nonlinear Quaternion Dynamics **(b) Linearized Quaternion Dynamics**

Figure 50. Reachable Set Depicted as Time Optimal Contours: Spherically Symmetric Body, Spherical Control Constraint

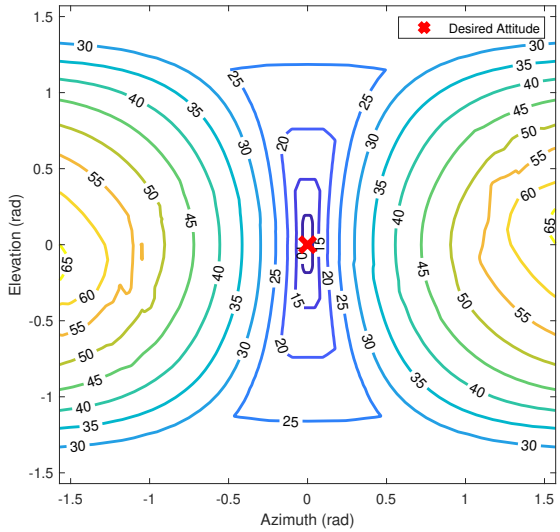

(a) Nonlinear Quaternion Dynamics

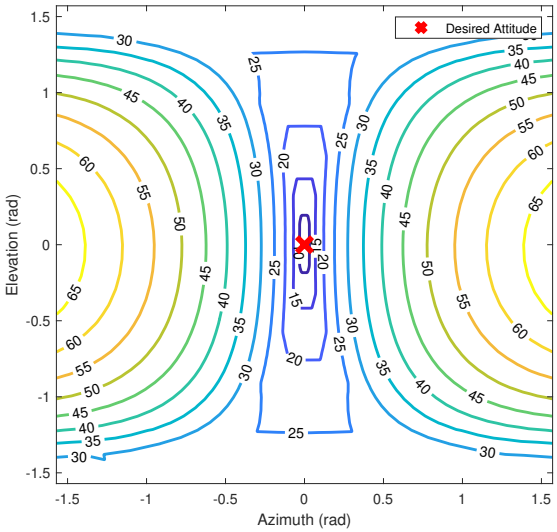

(b) Linearized Quaternion Dynamics

Figure 51. Reachable Set Depicted as Time Optimal Contours: Axisymmetric Body, Cubic Control Constraint

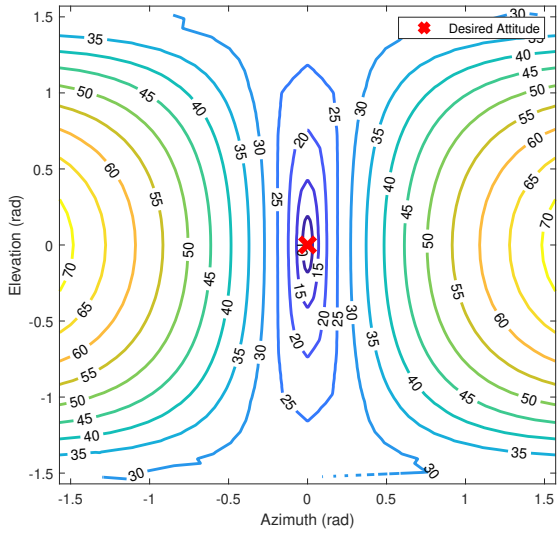

(a) Nonlinear Quaternion Dynamics

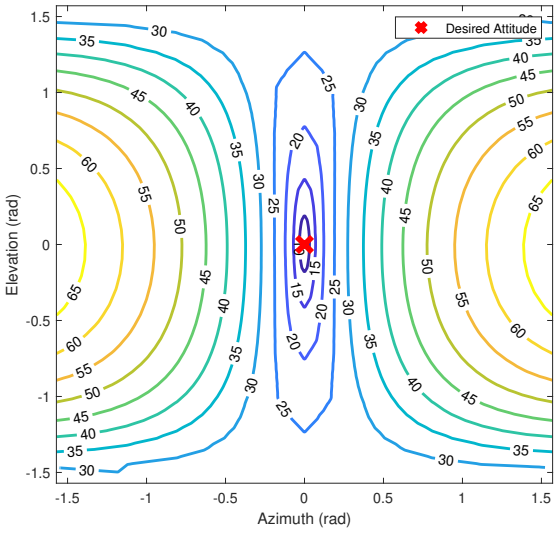

(b) Linearized Quaternion Dynamics

Figure 52. Reachable Set Depicted as Time Optimal Contours: Axisymmetric Body, Spherical Control Constraint

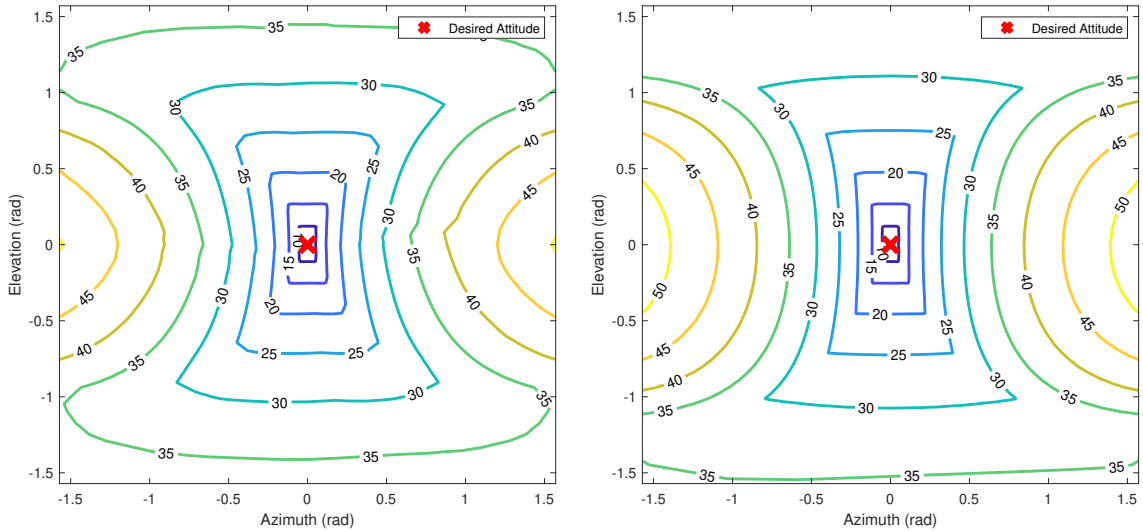

(a) Nonlinear Quaternion Dynamics **(b) Linearized Quaternion Dynamics**

Figure 53. Reachable Set Depicted as Time Optimal Contours: Asymmetric Body, Cubic Control Constraint

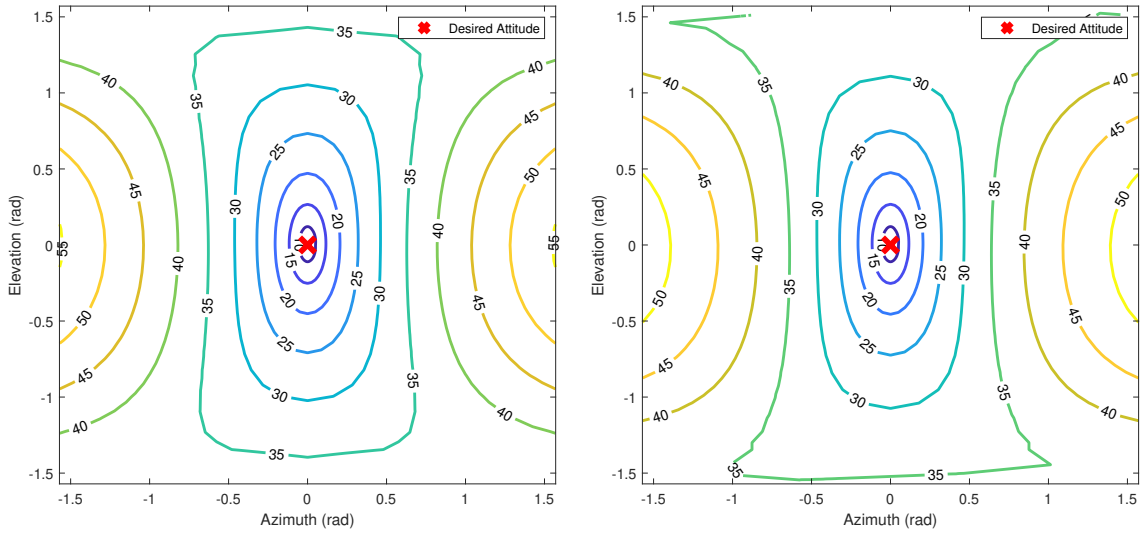

(a) Nonlinear Quaternion Dynamics **(b) Linearized Quaternion Dynamics**

Figure 54. Reachable Set Depicted as Time Optimal Contours: Asymmetric Body, Spherical Control Constraint

Bibliography

1. Karl D. Bilimoria and Bong Wie. Time-optimal three-axis reorientation of a rigid spacecraft. *Journal of Guidance, Control, and Dynamics*, 16(3):446–452, 1993.

2. Sandra L. Scrivener and Roger C. Thompson. Survey of time-optimal attitude maneuvers. *Journal of Guidance, Control, and Dynamics*, 17(2):225–233, 1994.

3. George A. Boyarko, Marcello Romano, and Oleg A. Yakimenko. Time-optimal reorientation of a spacecraft using an inverse dynamics optimization method. *Journal of Guidance, Control, and Dynamics*, 34(4):1197–1208, 2011.

4. Hanspeter Schaub and John Junkins. *Analytical Mechanics of Space Systems*. Number v. 1 in AIAA education series. American Institute of Aeronautics and Astronautics, 2003.

5. Hanspeter Schaub and John Junkins. Stereographic orientation parameters for attitude dynamics: A generalization of the rodrigues parameters. *Journal of the Astronautical Sciences*, 44, 01 1995.

6. Elizabeth Howell. Two private satellites just docked in space in historic first for orbital servicing. *Space.com*, Feb 2020.

7. Dehann Fourie, Brent E. Tweddle, Steve Ulrich, and Alvar Saenz-Otero. Flight results of vision-based navigation for autonomous spacecraft inspection of unknown objects. *Journal of Spacecraft and Rockets*, 51(6):2016–2026, 2014.

8. Jun Xu and Lihua Xie. *6 - Controllability and Reachability*, page 101–121. Woodhead Publishing, 2014.

9. M. Chen and C. J. Tomlin. Exact and efficient hamilton-jacobi reachability for decoupled systems. In *2015 54th IEEE Conference on Decision and Control (CDC)*, pages 1297–1303, 2015.

10. Costantinos Zagaris. Autonomous spacecraft rendezvous with a tumbling object: Applied reachability analysis and guidance and control strategies. Dissertation, Naval Postgraduate School Monterey United States, 2018.

11. Bong Wie. *Space vehicle dynamics and control*. American Institute of Aeoronautics and Astronautics, Inc., 2008.

12. Warren J. North, Helmut A. Kuehnel, John J. Van Bockel, and Jeremy B. Jones. Mercury project summary. Technical report, National Aeronautics and Space Administration, 1960.

13. John E. Cochran and John L. Junkins. Large angle satellite attitude maneuvers. *Flight Mechanics and Estimation Theory Symposium*, Apr 1975.

14. John L. Junkins and James D. Turner. Optimal continuous torque attitude maneuvers. *Astrodynamics Conferece*, Jul 1978.

15. Feiyue Li and Peter M. Bainum. Numerical approach for solving rigid spacecraft minimum time attitude maneuvers. *Journal of Guidance, Control, and Dynamics*, 13(1):38–45, 1990.

16. George Meyer. On the use of euler's theorem on rotations for the synthesis of attitude control systems. Technical report, National Aeronautics and Space Administration, 1966.

17. Robert Crisp and Donald Keene. Apollo command and service module reaction control by the digital autopilot. Technical report, National Aeronautics and Space Administration, 1966.

18. M. V. Dixon, T. N. Edelbaum, J. E. Potter, and W. E. Vandervelde. Fuel optimal reorientation of axisymmetric spacecraft. *Journal of Spacecraft and Rockets*, 7(11):1345–1351, 1970.

19. John L. Junkins and James D. Turner. *Optimal spacecraft rotational maneuvers*. Elsevier, 1986.

20. D.E. Kirk. *Optimal Control Theory: An Introduction*. Dover Books on Electrical Engineering Series. Dover Publications, 2004.

21. Michael A. Patterson and Anil V. Rao. A matlab software for solving multiple-phase optimal control problems using hp-adaptive gaussian quadrature collocation methods and sparse nonlinear programming. *ACM Trans. Math. Softw.*, 41(1), October 2014.

22. Philip E Gill, Walter Murray, and Michael A Saunders. Snopt: An sqp algorithm for large-scale constrained optimization. *SIAM review*, 47(1):99–131, 2005.

23. Jason Crane, Jason J. Westphal, I. Hussein, M. Oishi, A. Vinod, and Joseph D. Gleason. A formal approach to verification and validation of guidance, navigation, and control algorithms. *IEEE*, 2019.

24. Somil Bansal, Mo Chen, Sylvia Herbert, and Claire J Tomlin. Hamilton-jacobi reachability: A brief overview and recent advances. In *2017 IEEE 56th Annual Conference on Decision and Control (CDC)*, pages 2242–2253. IEEE, 2017.

25. Oded Maler. Computing reachable sets: An introduction. *Tech. rep. French National Center of Scientific Research*, 2008.

26. J. Lygeros. On the relation of reachability to minimum cost optimal control. In *Proceedings of the 41st IEEE Conference on Decision and Control, 2002.*, volume 2, pages 1910–1915 vol.2, 2002.

27. Varaiya P. Reach set computation using optimal control. In *Verification of Digital and Hybrid Systems*, volume 170, 2000.

28. Costantinos Zagaris and Marcello Romano. Reachability analysis of planar spacecraft docking with rotating body in close proximity. *Journal of Guidance, Control, and Dynamics*, 41(6):1416–1422, 2018.

29. Alex A. Kurzhanskiy and Pravin Varaiya. Ellipsoidal techniques for reachability analysis of discrete-time linear systems. *IEEE Transactions on Automatic Control*, 52(1):26–38, 2007.

30. Marcus Holzinger and Daniel Scheeres. Applied reachability for space situational awareness and safety in spacecraft proximity operations. In *AIAA Guidance, Navigation, and Control Conference*, page 6096, 2009.

31. K. Lesser, M. Oishi, and R. S. Erwin. Stochastic reachability for control of spacecraft relative motion. In *52nd IEEE Conference on Decision and Control*, pages 4705–4712, 2013.

32. Sangjin Lee and Inseok Hwang. Reachable set computation for spacecraft relative motion with energy-limited low-thrust. *Aerospace Science and Technology*, 77:180 – 188, 2018.

33. Qi Chen, Dong Qiao, Haibin Shang, and Xinfu Liu. A new method for solving reachable domain of spacecraft with a single impulse. *Acta Astronautica*, 145:153 – 164, 2018.

34. Joshuah Hess and Costantinos Zagaris. Rapid reachability analysis of single impulse spacecraft relative motion maneuvers. In *2020 AAS/AIAA Astrodynamics Specialist Virtual Lake Tahoe Conference*, 2020.

35. Michelle Chernick and Simone D'Amico. Closed-form optimal impulsive control of spacecraft formations using reachable set theory. *Journal of Guidance, Control, and Dynamics*, 44(1):25–44, 2021.

36. Costantinos Zagaris and Marcello Romano. Applied reachability analysis for spacecraft rendezvous and docking with a tumbling object. In *2018 Space Flight Mechanics Meeting*, 2018.

37. R. Bayadi, R. N. Banavar, and D. E. Chang. Characterizing the reachable set for a spacecraft with two rotors. In *2012 American Control Conference (ACC)*, pages 155–160, 2012.

38. Hanspeter Schaub. Modified rodrigues parameters definitions. CoursEra Videos, University of Colorado, Online.

39. Yaguang Yang. Spacecraft attitude determination and control: Quaternion based method. *Annual Reviews in Control*, 36(2):198–219, 2012.

40. Bong Wie and Jianbo Lu. Feedback control logic for spacecraft eigenaxis rotations under slew rate and control constraints. *Journal of Guidance, Control, and Dynamics*, 18(6):1372–1379, 1995.

41. Andreas Wächter and Lorenz T Biegler. On the implementation of an interior-point filter line-search algorithm for large-scale nonlinear programming. *Mathematical programming*, 106(1):25–57, 2006.

42. Xiaoli Bai and John L. Junkins. New results for time-optimal three-axis reorientation of a rigid spacecraft. *Journal of Guidance, Control, and Dynamics*, 32(4):1071–1076, 2009.

43. Unsik Lee and Mehran Mesbahi. Spacecraft reorientation in presence of attitude constraints via logarithmic barrier potentials. In *Proceedings of the 2011 American Control Conference*, pages 450–455. IEEE, 2011.

REPORT DOCUMENTATION PAGE

Form Approved
OMB No. 0704–0188

1. REPORT DATE *(DD–MM–YYYY)*	2. REPORT TYPE	3. DATES COVERED *(From — To)*
05–25–2021	Master's Thesis	August 2019 — March 2021

4. TITLE AND SUBTITLE

Applied Reachability Analysis for Time-Optimal Spacecraft Attitude Reorientations

5a. CONTRACT NUMBER

5b. GRANT NUMBER

5c. PROGRAM ELEMENT NUMBER

6. AUTHOR(S)

Barrett, Layne C., Capt, USAF

5d. PROJECT NUMBER

5e. TASK NUMBER

5f. WORK UNIT NUMBER

7. PERFORMING ORGANIZATION NAME(S) AND ADDRESS(ES)

Air Force Institute of Technology
Graduate School of Engineering and Management (AFIT/EN)
2950 Hobson Way
WPAFB OH 45433-7765

8. PERFORMING ORGANIZATION REPORT NUMBER

AFIT-ENY-MS-21-M-287

9. SPONSORING / MONITORING AGENCY NAME(S) AND ADDRESS(ES)

Intentionally Left Blank

10. SPONSOR/MONITOR'S ACRONYM(S)

11. SPONSOR/MONITOR'S REPORT NUMBER(S)

12. DISTRIBUTION / AVAILABILITY STATEMENT

Approved for Public Release; Distribution Unlimited

13. SUPPLEMENTARY NOTES

14. ABSTRACT Satellite attitude reorientation has been of significant interest in astronautical engineering, and being able to reorient in a time-optimal manner has been of exceeding interest since the 1970s. Ensuring a spacecraft mission set can be conducted within a certain amount of time begs the question of whether or not a certain maneuver can be completed with a bounded control. This thesis answers that question by using the concept of reachability to provide reachable sets for different spacecraft reorientation scenarios. The reachable sets generated provide a range of initial states that guarantee a satellite reach a desired end orientation given a certain time constraint. Prior research providing a formal approach of applying reachability to spacecraft attitude maneuvers has not been found. It was found that using Modified Rodriguez Parameters (MRPs) to generate reachable sets is more efficient than other attitude parameterizations. It was also found that the linearized MRP dynamics provide a valid time optimal solution for the true, nonlinear dynamics of medium angle attitude maneuvers. This linearized version of the dynamics was used to formulate an optimal control policy for spacecraft reorientations with bounded controls.

15. SUBJECT TERMS

Spacecraft Reorientation, Reachability, Optimal Control

16. SECURITY CLASSIFICATION OF:			17. LIMITATION OF ABSTRACT	18. NUMBER OF PAGES	19a. NAME OF RESPONSIBLE PERSON
a. REPORT	b. ABSTRACT	c. THIS PAGE			Major Costantinos Zagaris, AFIT/ENY
U	U	U	UU	93	19b. TELEPHONE NUMBER *(include area code)* (937) 255-6565 x4774 costantinos.zagaris@afit.edu